# Microstructural Development and Weldability Optimization in the Resistance Spot Welding of Quenched and Partitioned Steels

by

Bruna do Nascimento Figueredo

A thesis
presented to the University of Waterloo
in fulfillment of the
thesis requirement for the degree of
Master of Applied Science
in
Mechanical and Mechatronics Engineering

Waterloo, Ontario, Canada, 2021

## AUTHOR'S DECLARATION

This thesis consists of material all of which I authored or co-authored: see Statement of Contributions included in the thesis. This is a true copy of the thesis, including any required final revisions, as accepted by my examiners.

I understand that my thesis may be made electronically available to the public.

# Statement of Contributions

This thesis was solely written by the candidate. Professor E. Biro contributed to editing the entire dissertation and the paper which forms the base of Chapter 4. Additional contributions were made by other members of the Centre for Advanced Material Joining group from the University of Waterloo. The specific contributions are listed below.

Chapter 4 of this thesis was adapted from a journal paper that has been submitted to *Welding in the World*:

> B. Figueredo, D. C. Ramachandran, A. Macwan, E. Biro, "Failure Behavior and Mechanical Properties in the Resistance Spot Welding of Quenched & Partitioned (Q&P) Steels.", Welding in the World, 2021.

The experimental design, analysis, and writing were conducted solely by the candidate. The paper was co-authored by the candidate, Prof. E. Biro, Dr. A. Macwan from ArcelorMittal Dofasco, and Mr. D. C. Ramachandran. Mr. D. C. Ramachandran provided the EBSD results, which were used to characterize retained austenite and assisted in editing the microhardness and weld strength graphs used in the manuscript. Prof. E. Biro and Dr. A. Macwan contributed through technical discussions of the results and editing the manuscript.

Chapters 4 and 5 included the contributions from Dr. A. R. H. Midawi, Dr. N. Heinig, and Mr. M. Shojaee, who assisted with operating tensile testing equipment and SEM analysis. The data generated by tensile testing and SEM was processed and analyzed by the candidate. All experimental design, data analysis, and writing were conducted solely by the candidate. Prof. E. Biro again participated in technical discussions and editing the manuscript.

Chapters 5 and 6 of this thesis used data on the resistance spot welding behavior of Q&P980 obtained from chapter 4. Additional experimental work was completed using the material previously used in chapter 4.

Chapter 6 contains co-authored content. Mr. C. DiGiovanni developed the model for the domed electrode used in the modeling and assisted the candidate with training on the Sysweld® software. The candidate performed the simulation work and analysis of the output. All data analysis and writing were conducted solely by the candidate, with Prof. E. Biro participating in technical discussions and editing the manuscript.

# Abstract

Advanced high-strength steels (AHSS) have been widely used in the automotive industry to meet the demand for reduced fuel consumption and environmental emissions. Quenching and Partitioning (Q&P) is a heat-treatment method used to produce AHSS with higher ductility than similar strength steels, allowing for the use of thinner and lighter automotive parts due to its high formability. The mechanism behind how the microstructure of the different weld zones affects Q&P steel welds' mechanical properties is a topic that is yet to be fully understood.

In this study, the resistance spot welding behavior of Q&P steels was investigated through microstructure characterization, mechanical testing, failure behavior analysis, and computational simulation. It was found that the cross tension and tensile shear test samples all failed in a partial or full button pull-out mode, with an acceptable ductility ratio, but with lower cross tension strength compared to the available studies on resistance spot welding of Q&P steels. Fractography of the testing samples showed that the crack propagated along the fusion boundary, an occurrence previously reported in the literature for Q&P980, but with no comprehensive explanation regarding the mechanism behind the behavior. This work discusses how this fracture is possibly related to the formation of a softened region at the fusion boundary, a phenomenon commonly known as halo ring.

Weldability optimization was analyzed using multiple pulsing welding schedules and the study of their effects on the microstructural development of the welds and their mechanical properties. It was found that a second pulse with a higher current than the primary pulse is effective in avoiding the occurrence of halo ring and improving cross-tension strength. Multi-pulsing consistently improved overall weld strength even when normalizing the values to decouple the effect of increased weld diameter. The relationship between the occurrence of halo ring and the weldability is discussed along with alternative theories correlating the microstructure and microhardness to the observed improvements.

A computational simulation was applied to investigate the mechanism behind how the described multi-pulsing weld schedule eliminates the halo. It was found through the study of the thermal cycles in the weld that a high current second pulse effectively remelts the weld nugget, avoiding the fusion boundary to remain static towards the end of the welding cycle and thus not allowing for the formation of the softened zone.

# Acknowledgments

I would like to acknowledge and thank my supervisor, Prof. Elliot Biro, for the time, knowledge, support, and guidance he has given me in the last two years.

I would also like to thank the industry sponsors for this project, specifically Dr. Andrew Macwan from ArcelorMittal Dofasco Hamilton. This research would not have been possible without their support.

I am grateful to Dr. Yuquan Ding and Mr. Mark Griffett for their time and assistance in running many mechanical tests essential for this thesis. Also, I wish to acknowledge my fellow CAMJ members' assistance, especially Mohammad Shojaee, Abdelbaset Midawi, Chris DiGiovanni, Dileep Ramachandran, and Alireza Mohamadizadeh. Their help and support made all the difference in this experience.

Finally, I wish to thank my family and friends for their love and support throughout these years. I would not have been able to complete this degree without you.

# Table of Contents

# List of Figures

# List of Tables

# List of Abbreviations

AHSS – Advanced high strength steels

ANOVA – Analysis of variance

AWS – American welding society

BIW – Body-in-white

BM – Base material

CGHAZ – Coarse grain upper critical heat-affected zone

CP – Coach peel

CTS – Cross-tension strength

DOE – Design of experiments

DP – Dual-phase

FGHAZ – Fine-grain upper critical heat-affected zone

FZ – Fusion zone

GWP – Global warming potential

HAZ – Heat affected zone

ICHAZ – Intercritical heat-affected zone

MFDC – Medium frequency direct current

MS – Martensitic Steels

MWS – Minimum weld size

OEM – Original equipment manufacturer

Q&P – Quenched and partitioned

RSW – Resistance spot welding

SCHAZ – Subcritical heat-affected zone

SEM – Scanning electron microscope

TM – Tempered Martensite

TRIP – Transformation-induced plasticity

TSS – Tensile–shear strength

TWIP – Twinning induced plasticity

UCHAZ – Upper critical heat-affected zone

UTS – Ultimate tensile strength

YS – Yield strength

# List of Symbols

$\alpha$ – Statistical significance level

$A_{c1}$ – Austenite transformation start temperature

$A_{c3}$ – Austenite transformation end temperature

$d_n$ – Weld diameter

$F_{max}$ – Maximum load

I – Welding current

Q – Heat

$Q_{total}$ – Total heat generated through the RSW process

R – Electrical resistance

$M_s$ – Martensite start

$M_f$ – Martensite finish

$S_{max}$ – Normalized weld strength

t – Welding time

$t_{sheet}$ – Steel sheet thickness

# Chapter 1
# Introduction

## 1.1 Overview

With new regulations regarding fuel consumption and efficiency, the automotive industry has responded with an increased focus on reducing vehicle weight while improving passenger safety. Advanced High Strength Steels (AHSS) have been ideal options for achieving these goals. The combination they offer of high strength and high ductility makes it possible to manufacture thinner and lighter automotive parts, maintaining mechanical performance levels and ensuring passenger safety. These steels are commonly joined during body-in-white assembly using the resistance spot welding (RSW) process [1–4].

Quenching and partitioning (Q&P) steels have been included in the family of the third generation of AHSS, which achieve the desired combination of high strength and ductility through a microstructure that includes a significant amount of high strength constituents such as martensite, bainite (ferrite with cementite phase) and/or ultra-fine grains of ferrite along with other phases providing ductility and work hardening such as austenite [5]. Similarly to the conventional quenching and tempering process, the quenching and partitioning method is a two-step heat treatment consisting of partial or full austenitization, followed by a quench and an isothermal annealing process named partitioning, where carbon is redistributed from the supersaturated martensite formed in the quenching step to the austenite, stabilizing it [1, 6–8].

The Q&P process was first proposed by Speer et al. in 2003 [7], and due to its relative novelty, there still has been limited research published on the weldability of these alloys. Overall, the literature available for these steels diverges significantly on the general effects of the RSW process, with sources reporting different microstructural developments for similar welding schedules and providing various explanations for the failure mode of the welds. Although some studies report on the microstructural changes during welding and the post-welded properties, no work has reported how the post-welded microstructure affects crack propagation when the welds are loaded.

## 1.2 Objectives

This thesis aims to analyze the microstructure development and mechanical behavior of the resistance spot welding of Q&P steels and investigate and apply the findings to optimize the weldability of these steels. Specific objectives include:

1. Correlate the welding microstructure to the mechanical performance and failure behavior of Q&P RSW joints.
2. Investigate the effect of different weld schedules on the performance of the welded joints.
3. Understand the correlation between thermal cycles, failure mode, and weld optimization.
4. Optimize the Q&P RSW joint microstructure and post-weld properties.

## 1.3 Criteria and Constraints

The welding parameters used in this study were based on the American Welding Society (AWS) standards for resistance spot welding of automotive steels (AWS D8.1M and D8.9M) [9, 10]. Details on modified welding schedules used to understand the effect of pulsing parameters on the weld joints are described in Chapter 3. Mechanical testing and other characterization methods are also detailed in Chapter 3. All testing was based on AWS standards unless otherwise specified. This thesis work is limited to investigating the RSW behavior of two different grades of AHSS (Q&P980 and DP980) due to material availability and interest from the industry.

## 1.4 Thesis Outline

This thesis has been organized into seven chapters, as follows:

*Chapter 1: Introduction* – Introduces the topics covered in this thesis, including the overview, objectives, constraints, and organization of the report.

*Chapter 2: Literature Review* – Provides an overview of the relevant concepts and literature related to this study, such as a background on AHSS and, more specifically, Q&P steels, the RSW process, and the occurrence of transient softening at the fusion boundary in RSW.

*Chapter 3: Methodology* – Details the materials used, resistance spot welding equipment and parameters, characterization methods, and mechanical testing applied in this study.

*Chapter 4: Failure Behavior and Mechanical Properties in the Resistance Spot Welding of Quenched and Partitioned Steel* – Describes the results of the RSW of Q&P steels under standard parameters as given by AWS D8.9M, investigating the microstructural development, failure behavior, and mechanical properties of the welds.

*Chapter 5: Optimization of Weld Performance by Varying Weld Schedules* – Explores the effects of various welding schedule parameters, including pulsing current and cooling time, on the failure behavior and performance of Q&P joints, as well as deriving a strategy for optimizing the weldability of Q&P steels.

*Chapter 6: Analysis of the Correlation between Thermal Cycles and Weld Strength* – Studies the correlation between the thermal cycles during the weld as found by the computational simulation to the failure mode seen experimentally.

*Chapter 7: Conclusion and Recommendations* – Summarizes all of each chapter's significant findings and future work recommendations.

# Chapter 2
# Literature Review

## 2.1 Advanced High Strength Steels (AHSS)

New safety and fuel efficiency regulations in the automotive industry have challenged original equipment manufacturers (OEMs) to find new solutions to reduce vehicle weight while improving crashworthiness and passenger safety [11–14]. These goals are seemly contradictory – while an increase in vehicle mass is related to a decrease in injury risk during collisions, it also leads to an increase in fuel consumption. Studies have shown that, for petrol cars, an increase of 100 kg in mass increases fuel consumption by as much as 3.9%, while in diesel cars, the fuel consumption is increased by as much as 6.2%. Conversely, an increase of 100 kg in mass also leads to a decrease in injury risk by as much as 3.2% [15]. The automotive industry responded to this trade-off issue by rethinking material applications and looking for possible alternatives [12].

Advanced High Strength Steels (AHSS) is a family of steels with particular combinations of strength and formability parameters, generally described as having tensile strength above 500 MPa and complex multiphase microstructures [11–13, 16, 17]. The combination they offer of high strength and good ductility makes it possible to manufacture thinner and lighter automotive parts, maintaining mechanical performance levels and ensuring passenger safety. The sections below describe the different grades of AHSS, their application in the automotive industry and give further details into dual-phase and Q&P steels, which are the focus of this work.

### 2.1.1 Generations of AHSS

Despite being relatively new, AHSS have been historically divided into three generations. Figure 2.1 shows the strength versus elongation values that are obtainable for each generation of AHSS. These combinations are achieved by precise engineering of the volume fractions of the steel's sub-structures and phases through the selection of the chemical composition of the steel and the thermomechanical processing steps applied in manufacturing [11–14].

The first generation of AHSS included, amongst others, the dual-phase (DP), the martensitic (MS), and the transformation-induced plasticity (TRIP) steels. These were some of the first alloys designed to provide unique microstructures to meet the industry's demand for specific safety conditions, often through the combination of a ferritic and martensitic structure. The first generation was characterized by its high

strength, with ultimate tensile strength (UTS) ranging from 400 MPa to 2000 MPa, and reasonable formability, with elongation ranging from 0% to 30%, as shown in Figure 2.1. The second generation included highly alloyed steels, such as the twinning induced plasticity (TWIP). This generation provided a superior combination of strength and ductility compared to the first-generation AHSS, with UTS ranging from 800 MPa to 1700 MPa, while the elongation achieved values as high as 70%. However, the second generation presented additional challenges in the form of manufacturability problems, high sensitivity to hydrogen embrittlement, and high cost of alloying elements such as chromium, nickel, and manganese, which lead to the currently ongoing development of the third generation of AHSS [11, 13, 14, 17–19].

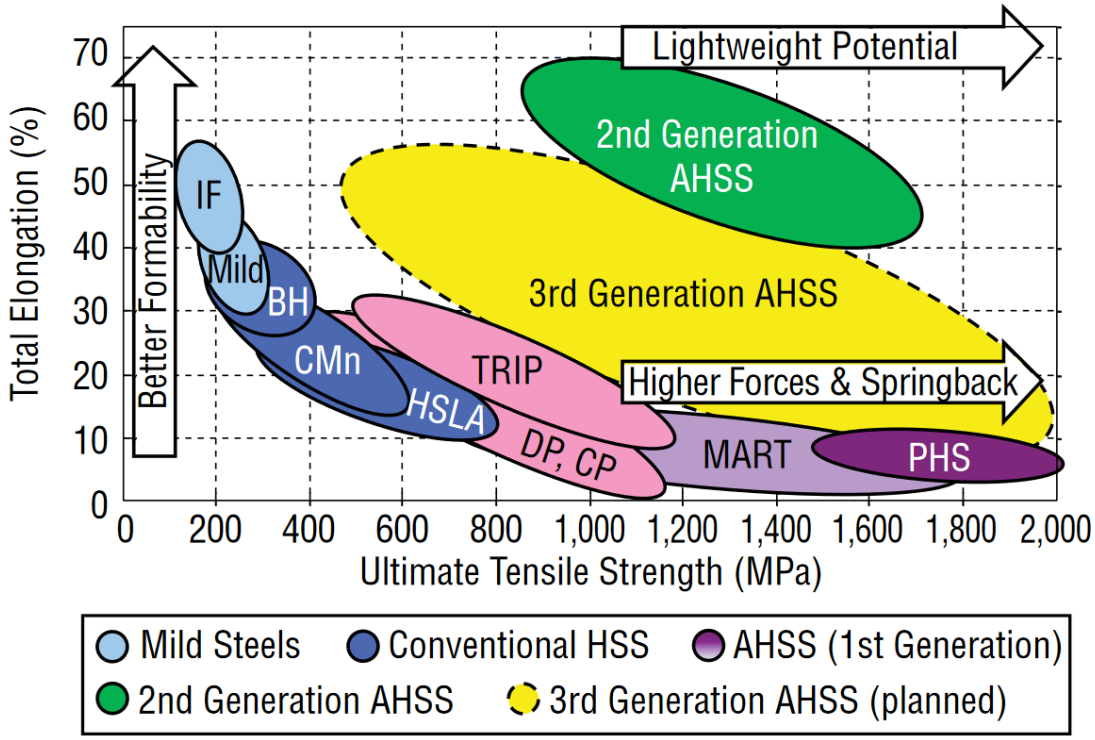


**Figure 2.1: Ultimate tensile strength and elongation for mild steels, high strength steels, and the three generations of advanced high strength steels** [18]**.**

This third generation of AHSS is currently under research and development. It is set to be characterized by material properties that close the gap between the first and second generations (as shown in Figure 2.1), with UTS values ranging from 500 MPa to 2000 MPa, and elongation varying from around 10% to 60%, achieving the desired combination of high strength and ductility at a more reasonable cost [14, 20]. Matlock and Speer [21] have described that the third generation of AHSS will feature a complex microstructure with

a significant amount of high strength constituents such as martensite, bainite, or ultra-fine grains of ferrite, along with other phases with good ductility and work hardening, such as austenite.

### 2.1.2 Application in the Automotive Industry

The automotive industry has seen a consistent increase in the application of AHSS. Studies report that AHSS have been the industry's fastest-growing light-weighting material, with a fourfold increase in use from 2006 to 2016. AHSS currently used by automakers have reduced the vehicles' body mass by a minimum of 25%, with the third generation being projected to reduce the mass by as much as 35% [14, 22]. Significant reductions in greenhouse emissions are also being achieved, with Hardwick and Outteridge [23] showing that a B-pillar design using AHSS instead of the conventional boron steel achieved a global warming potential (GWP) reduction of 29% while also improving the crash performance of the part during side impacts.

AHSS are mainly used in energy-absorption structural components, where they significantly improve the level of crash energy absorption and impact protection of the vehicle. The most typical applications of AHSS in automotive body parts include safety cage components such as B-pillars and A-pillars, dash panels, crash boxes, frame rails, and roof rails, among others [12–14, 22]. The use of AHSS in the body-in-white (BIW) of a 2019 Chevrolet Silverado is shown in Figure 2.2.

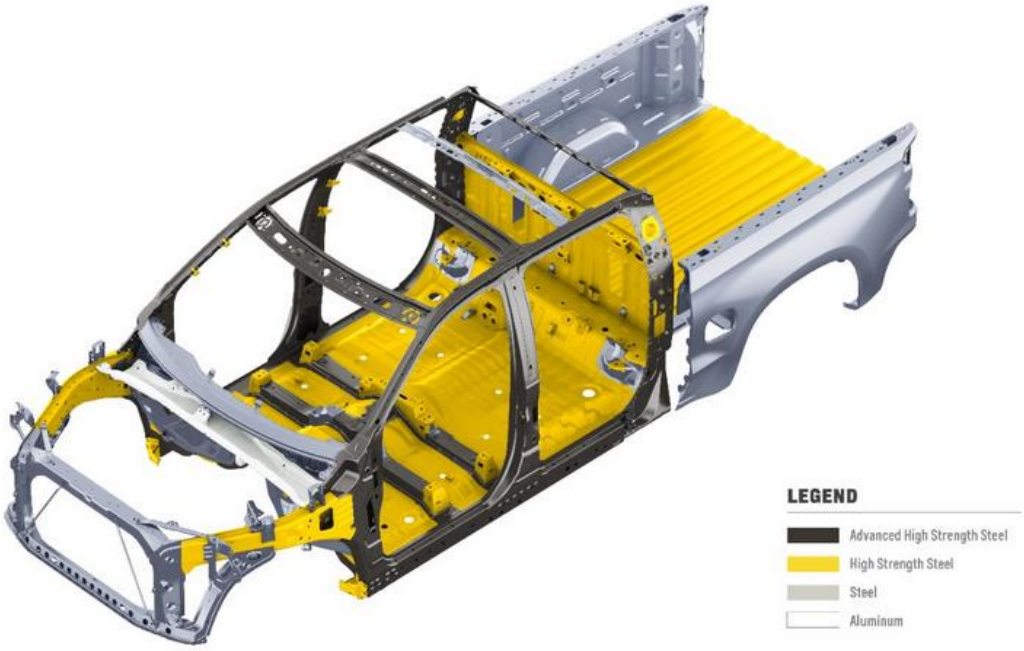


**Figure 2.2: Different grades of steel in the structure of a 2019 Chevrolet Silverado** [24]**.**

### 2.1.3 Dual-Phase Steels

Dual-phase (DP) steels are generally considered to be the flagship of AHSS. They are characterized by the combination of a relatively soft ferrite matrix, responsible for the excellent formability of the steels, with hard martensite islands, which act as a strengthening phase [11–14, 25]. DP steels are produced by controlled cooling from the intercritical temperature where both ferrite and austenite are stable so that some of the austenite possibly transforms into ferrite, and then rapid cooling to transform the remaining austenite into martensite. A typical cooling curve for these steels and the corresponding microstructure is shown in Figure 2.3. The production process of DP steels sometimes also leads to the possible generation of small amounts of bainite or retained austenite [17, 18, 22, 26].

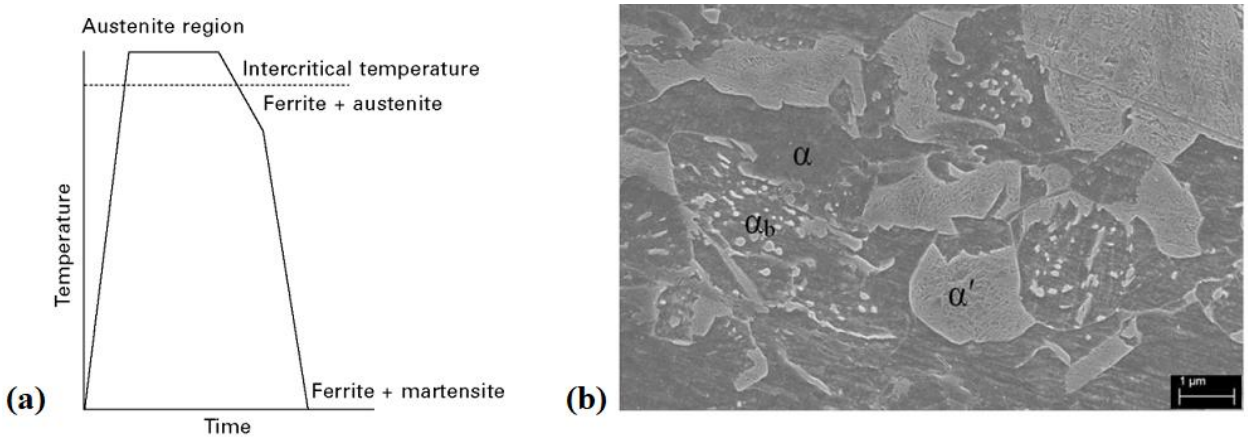


**Figure 2.3: Dual-Phase steels (a) Typical cooling curve, and (b) Microstructure showing α (ferrite), α' (martensite), and $\alpha_b$ (bainite).** Adapted from [17] and **[26].**

DP steels typically contain from 10% to 70% volume fraction martensite, where the strength of the material is determined by the amount of martensite in its microstructure. The crashworthiness of the steel (dynamic absorbed energy) is also informed by the characteristics of the martensite in its structure, as it increases if said martensite is finely dispersed. Typical tensile strength for DP steels ranges from 500 to 1270 MPa, and total elongation varies from around 10% up to 28% [17, 22, 27].

### 2.1.4 Quenching and Partitioning Steels

Quenching and partitioning (Q&P) is a heat treatment first proposed by Speer et al. [7] in 2003 to produce high-strength steels that also offer good ductility. The treatment results in a martensitic structure with retained austenite, where the martensite is responsible for the high strength of the alloy, and the retained austenite offers its excellent ductility. The Q&P process consists of heating the steel to partial or full

austenitization, then partially quenching it to a temperature between martensite start ($M_s$) and martensite finish ($M_f$) to obtain a desired fraction of martensite. From there, the steel is held isothermally either at the initial quenching temperature (one-step Q&P) or is heated up to the partitioning temperature (two-step Q&P) so that the steel goes through an isothermal annealing process named partitioning, where gradual carbon enrichment of austenite occurs. During partitioning, carbon diffuses from the supersaturated martensite to the austenite, stabilizing the austenite. The final step consists of quenching the steel to room temperature [1, 6–8, 28]. Figure 2.4 schematically shows the quenching and partitioning process and the corresponding microstructure.

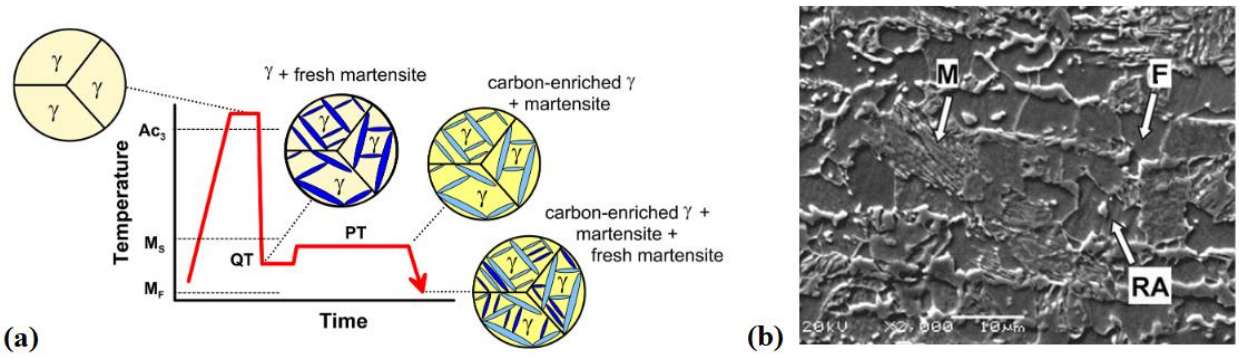


**Figure 2.4: Quenching and Partitioning (a) Schematic for the two-step process and (b) Microstructure showing F (ferrite), M (martensite), and RA (retained austenite).** Adapted from [1] and **[29]**.

Q&P process parameters directly affect the steel's microstructure, including the morphology, distribution of micro constituents, and carbon content in individual phases. These steels' mechanical properties are also highly dependent on the quench and partitioning conditions, mainly the quench temperature, as it directly affects the resulting retained austenite fractions. The transformation of retained austenite into martensite during tensile deformation is mainly responsible for the steel's mechanical behavior. Studies show that the strain hardening during tensile deformation in Q&P steels is determined by the volume fraction and morphology (i.e., stability) of the retained austenite. The volume fraction of secondary martensite, which forms upon cooling to room temperature after the partitioning step, is also a key factor determining the mechanical properties of Q&P steels, as it leads to a reduction in tensile ductility due to its high dislocation density and large solid solution strengthening [28, 30–32].

Q&P steels typically contain 50% to 80% volume fraction martensite and 10% to 20% retained austenite. Current tensile strength values for Q&P steels range from 1000 to 1400 MPa, and ductility from 10% to

30%, although it should be noted that mechanical properties are expected to continue advancing through ongoing research [1, 7, 32].

### 2.1.5 Surface coating of AHSS

Corrosion protection is an essential factor for consumers and automotive manufacturers, and it is mainly addressed by coating the steel with zinc or its alloys, which protects the steel through one or more of the following mechanisms or methods: barrier protection, galvanic/sacrificial corrosion, and formation of a barrier layer of precipitated zinc compounds. In barrier protection, the steel is isolated from the corrosive environment by the zinc coating. In the galvanic method, as zinc is anodic to iron at ambient conditions, it will sacrificially corrode to protect the steel, even if the steel is exposed at coating voids. Lastly, zinc corrosion products protect the exposed steel at coating voids, as the elevated pH at the surface of the steel promotes the deposition of dissolved zinc in the form of hydroxide and related compounds [33, 34].

As AHSS are increasingly being used in the automotive industry, zinc coatings are also applied to protect these steels from corrosion during service [35, 36]. The most common methods to produce zinc coatings include hot-dip galvanizing and electrodeposition. Among the main zinc-coated steel sheets are the hot-dip galvanized (HDG or GI), the galvannealed (GA), and the electro-galvanized (EG). The hot-dip process was the first to be widely used in car bodies. It consists of a steel article's immersion in a liquid bath of zinc or a zinc alloy, where the steel reacts with the bath forming the coating. The galvannealed coating is a hot-dip process where the coated steel is re-heated to allow interdiffusion of zinc and iron, thus forming an alloy coating. Finally, the electroplated zinc-coating consists of zinc's electrodeposition onto the steel substrate, providing a uniform coating thickness and better surface finish than the hot-dip process [33, 34, 37].

## 2.2 Resistance Spot Welding

Automotive steels are commonly joined during body-in-white (BIW) assembly using the resistance spot welding (RSW) process. RSW alone or a combination of RSW and other joining methods account for over 70% of the welding of a BIW assembly. A single automotive body can have as many as 7000 spot welds, primarily due to the varied advantages of the process related to its simplicity, including the low cost, fast operation, and no use of filler materials [38]. The crashworthiness of a vehicle largely depends on the integrity of the welds, which are used to transfer load through the structure in the event of a crash and can

act as fold initiation sites to manage the impact energy distribution [16, 17, 39–41]. Proper selection of welding parameters and process control is essential in ensuring the vehicle's performance and safety.

The following sections cover this process's details and provide a background on the literature available regarding RSW of the materials relevant to this study.

### 2.2.1 Process overview

In resistance spot welding, an electric current passes through two copper-based water-cooled electrodes and the metal sheets being joined, such that the resistance to current flow generates intense localized heating. The high temperature causes the melting and coalescence of the material at the interface between the sheets, forming a weld nugget as the materials cool down. Heat is generated in the RSW process through what is known as Joule heating, which, in a general sense, can be expressed by the equation:

$$Q = I^2Rt \qquad \text{(Eq. 2.1)}$$

where Q denotes total heat energy, I is the current, R the electrical resistance, and t the time during which the current is allowed to flow. In this process, the copper alloy electrodes are responsible for conducting the current to a small diameter area and for applying pressure to the sheets, ensuring adequate contact between the parts, and holding them together through the operation [17, 39–43]. The resistance spot welding process is illustrated in Figure 2.5.

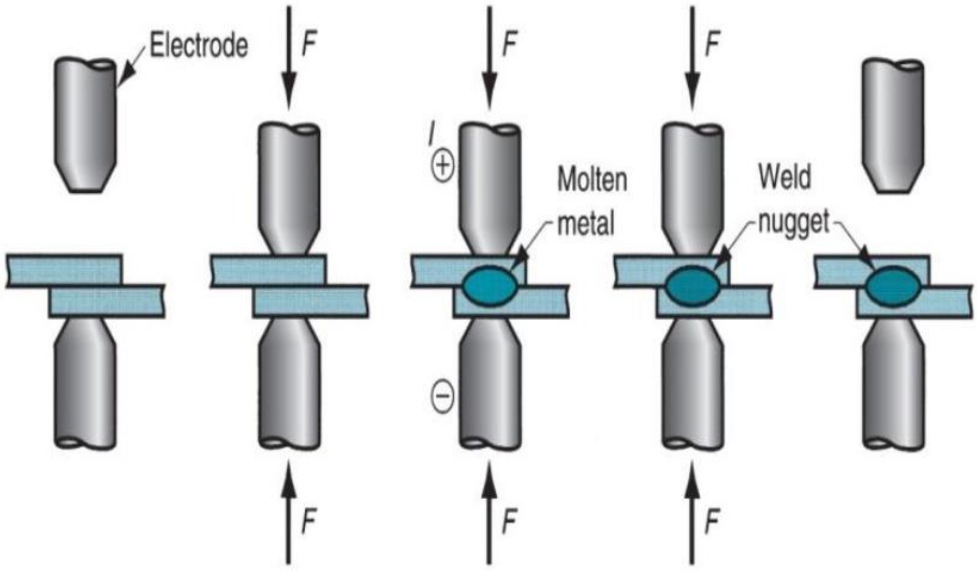


**Figure 2.5: Schematic of the resistance spot welding (RSW) process [44]**.

In RSW, the resistance of a joint changes throughout the welding cycle. Figure 2.6 (a) presents a theoretical dynamic resistance curve, which illustrates this variation in resistance. It can be seen that resistance at the start is high due to the presence of surface films, oxidants, and other contaminants, which act as insulators. Heat causes these contaminants to break down, lowering the resistance. As heating from the contact resistance rapidly elevates the temperature of the steel, the resistivity also increases, which causes the bulk resistance of the sheets to be the dominant resistance, leading to the formation of the nugget. However, the nugget growth also causes the current path to become larger, reducing the current density, which can decrease even further if there is indentation. If the molten nugget grows to a size where the electrode force can no longer contain it, expulsion occurs, further decreasing the resistance [43, 45].

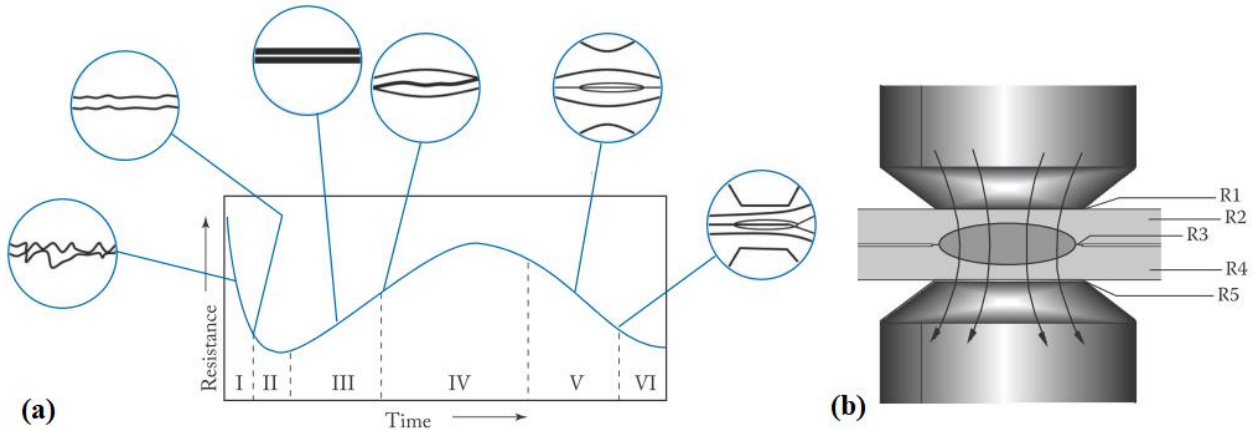


**Figure 2.6: (a) Dynamic resistance curve and (b) Electric resistances in RSW.** Adapted from **[42]** and **[43]**.

There are five main resistances acting in series in a RSW sheet stack-up, as shown in Figure 2.6 (b). Resistances 1 and 5 are the contact resistances between the sheets and the electrodes, while resistances 2 and 4 represent the bulk sheet resistance. Resistance 3 is the sheet/sheet interfacial resistance, or faying resistance. In the RSW process, the total electric resistance, R, corresponds to the sum of the contact resistance between the electrodes and sheet surfaces, the bulk resistance of the sheets, and the contact resistance at the sheet interface. The highest resistance is that at the sheet-to-sheet interface, which is why the weld nugget is formed between the sheets, where it is needed. These resistances' values are not constant, as the contact resistance is a function of both temperature and pressure, and the bulk resistance is sensitive to temperature [42, 43]. That way, equation 2.1 can be integrated, resulting in the total heat generated ($Q_{total}$) during the RSW process:

$$Q_{total} = \int \{I^2 R(t)\}\, dt \qquad \text{(Eq. 2.2)}$$

The RSW process can be quite complex and challenging to control, as it involves the interaction between physical and metallurgical properties of the materials being welded and the interaction between mechanical and electrical characteristics of the welding equipment. Obtaining a weld nugget with acceptable size and strength requires complete understanding and careful control of the process, which is why much attention is given to designing and monitoring RSW applications [40, 41].

### 2.2.2 Welding Parameters

The main parameters in RSW are the welding current, the welding time, and the electrode force, with the surface condition, electrode tip design, and fit-up between the sheets also having a significant influence on the weld nugget [17, 41, 43, 46]. The main parameters are better visualized within the spot-welding cycle, shown in Figure 2.7. The cycle starts with the squeeze time, which is the time required to develop the electrode force that will ensure contact between the sheets, followed by the weld time, which is the time in which the current is applied, and then the hold time, where the electrode force is still applied, but current does not flow, allowing for cooling and solidification of the weld. More complex cycles can include quenching and tempering times and the application of a forging force.

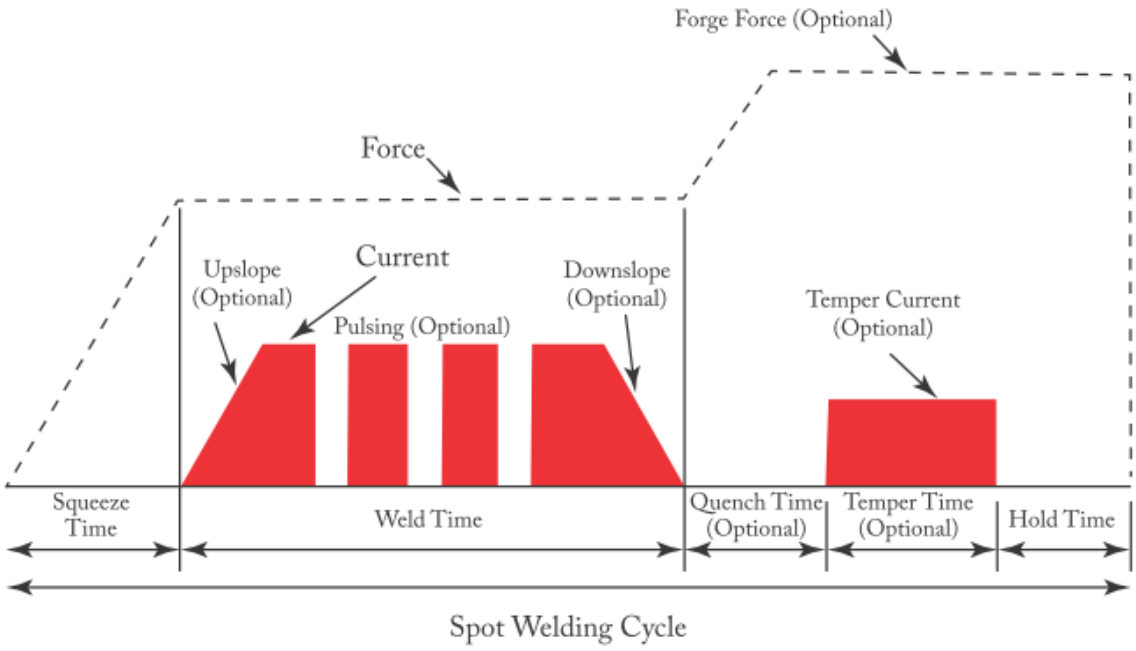


**Figure 2.7: Resistance spot welding cycle [43].**

The welding parameters affect not only the nugget size (and consequently its strength) but also have different effects on the quality of the weld. The nugget diameter increases with increasing weld current

and increasing weld time, with each material having different ranges of current and time where acceptable welds are produced. AWS D8.9M [9] recommends the minimum acceptable nugget size for automotive applications as $4t_{sheet}^{1/2}$, where $t_{sheet}$ is the sheet thickness in mm. While low current results in an incomplete nugget with a diameter below the minimum acceptable size, a high current leads to expulsion, which also produces an unacceptable nugget. This relationship is illustrated in what is called a weldability lobe, shown in Figure 2.8.

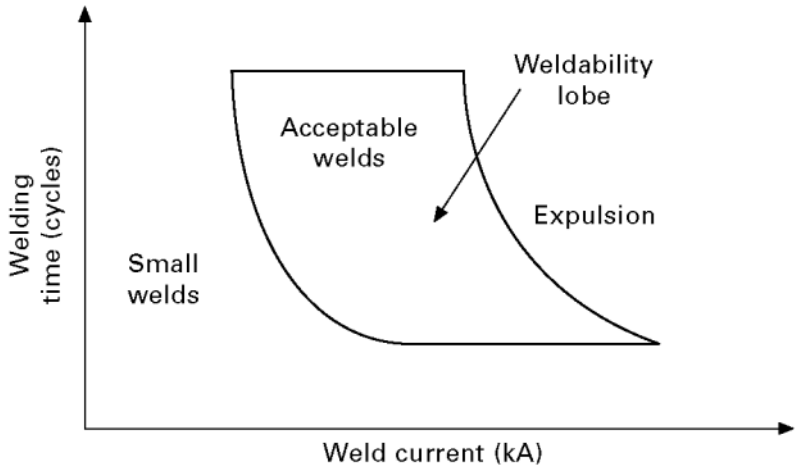


**Figure 2.8: Weldability lobe for RSW process** [17].

The weld lobe is highly influenced by the electrical resistivity of the materials being welded and the surface condition of the sheets. Higher electrical resistivity leads to a decrease in weldability, which leads to a narrower lobe as the current range where acceptable welds are achieved gets smaller, and coated steels need longer welding times and higher currents than uncoated steels, which shifts the weldability lobe toward higher current levels. Other parameters that influence the weldability lobe include the electrode force, where higher electrode force relates to wider lobes, and the sheet thickness, with thicker sheets leading to an increase in the lobe's width. The wider the weldability lobe, the wider is the current range where acceptable welds are achieved, which correlates to a higher tolerance to process variations [17, 41, 43, 47, 48].

### 2.2.3 Pulsed Welding Schedules

Resistance spot welding schedules that include multiple pulses have been applied to improve weldability by increasing the weld lobe range, reducing expulsion, and modifying the joints' failure mode [43, 49]. Pulsing is one of the most efficient methods of modifying the microstructure and consequently the mechanical properties of a weld, as a pulsed welding current effectively causes the weldment to undergo

various heating and cooling cycles, producing a different thermal history than that achieved by a single pulse [50, 51].

Kimchi and Philips [43] describe using a three-pulse weld schedule for welding coated steels, as shown in Figure 2.9. The method was applied to widen the weld lobe of a zinc-coated HF steel, where an initial short pulse with a high current was used to break the oxide layers and ensure good contact between the sheets, while the second pulse of lower current and longer time initiates the nugget formation at the same time it avoids expulsion, and a third pulse, similar to the previous one, grows the nugget to the desired diameter. Although the solution is valid for the desired application, it also leads to a longer weld cycle which is often undesirable for high-speed automotive production.

Another approach to using multi-pulse welding schedules is to apply a short pulse after the main pulse in order to briefly re-heat the nugget and improve the mechanical properties of the joint without a significant increase in the weld time [52–54]. This method was shown to improve the joints' strength, with the potential of also changing the welds' failure mode. Other studies have also successfully applied different pulsing schedules and techniques to achieve the desired improvements in the RSW of various materials.

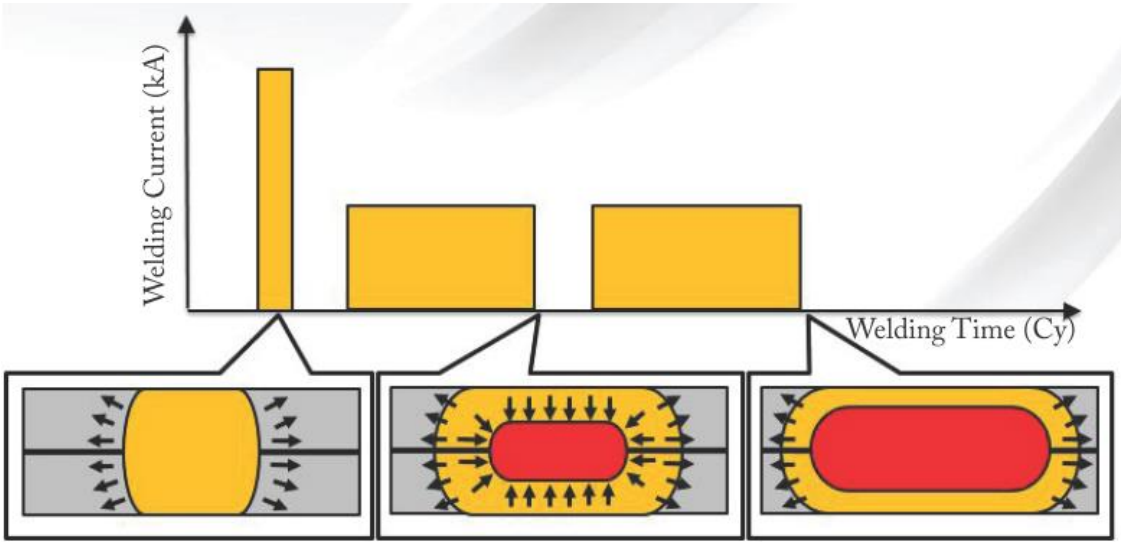


**Figure 2.9: Three-pulse weld schedule for welding-coated steels [43]**.

### 2.2.4 Weld Zones in RSW

A weldment can be divided into three distinct regions: the fusion zone (FZ), the heat-affected zone (HAZ), and the base material. The fusion zone undergoes melting and solidification, the heat-affected zone experiences solid-state phase changes but does not melt, and the base material remains unaffected [40, 55].

In resistance spot welding of steels, the heat-affected zone is often further divided into coarse grain upper critical heat-affected zone (CGHAZ), which experiences high temperatures leading to significant grain growth, the fine grain upper critical heat-affected zone (FGHAZ), which experiences lower peak temperatures and complete austenitization, the intercritical heat-affected zone (ICHAZ), which undergoes partial austenitization, and finally, the subcritical heat-affected zone (SCHAZ), where no significant phase transformations are found [56]. These regions are shown in Figure 2.10.

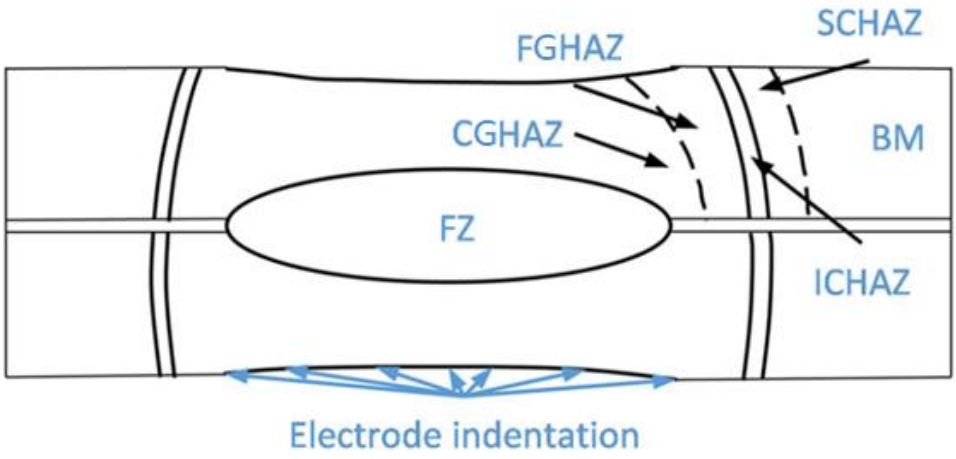


**Figure 2.10: Schematic illustration of resistance spot weld zones.** Adapted from **[57]**.

The fusion zone can be considered the most critical geometrical parameter of the weld, as it determines the joint's overall bonding area. It is also usually fully martensitic due to the high cooling rates related to the welding process. The heat-affected zone has a sizeable microstructural gradient, as its microstructure depends on the interaction between the base material structure and the thermal weld cycle. As mentioned above, the HAZ can be sub-divided into the upper critical heat-affected zone (UCHAZ), intercritical HAZ, and subcritical HAZ, where the upper critical HAZ is often further divided into CGHAZ and FGHAZ [40, 57–59].

The peak temperatures in UCHAZ are above $A_{c3}$ and lower than the melting temperature of the steel, therefore undergoing full austenitization during the weld cycle, usually presenting a martensitic structure after quenching. The ICHAZ has a peak temperature between $A_{c1}$ and $A_{c3}$, undergoing partial austenitization during heating, with its microstructure being composed of both ferrite and martensite. In the SCHAZ, the peak temperature falls below $A_{c1}$, with tempering of any existing martensite usually leading to softening in this zone [57–59].

### 2.2.5 Resistance Spot Weldability and Quality

As mentioned in section 2.2.2, the weld nugget size – and consequently the weldability lobe – is the primary indicator of spot weld quality. However, there are many other factors used to determine the resistance spot weldability of steels, which can be classified into three categories: the weld's physical and metallurgical properties, its mechanical performance, and failure mode [40, 42, 60].

Factors related to physical and metallurgical attributes include the weld diameter, the presence of voids and cracks, the weld surface's appearance, and the weld zones' hardness and material properties. Voids can occur mainly due to expulsion or shrinkage during the cooling process and cause a reduction in the load-bearing area of the welds and stress concentration [61]. The hardness distribution across the weld zones is controlled by the interaction between the thermal weld cycle, chemical composition, and microstructure of the material, and it is directly related to the joint's mechanical performance [40–43].

The mechanical performance of a spot weld usually refers to its static/quasi-static and dynamic strength. Although the dynamic response of a joint is essential for assessing the crashworthiness of vehicles as it relates to the performance of the welded structures during car crashes or collisions, the high cost, complexity, and low reliability of dynamic testing have caused it to be conducted in a limited scale, with static tests being almost exclusively used to assess weldability [42]. Tensile–shear strength (TSS), cross-tension strength (CTS), and coach peel (CP) tests are the most widely used indicators of a weld's mechanical behavior. Figure 2.11 shows a schematic representation of the sample geometry and stress distribution in a weld during TSS and CTS. Spot welds in automotive structures can experience both shear loading due to the displacement or rotation of adjacent sheets as well as tensile loading due to separating forces between the adjacent sheets in a direction normal to the sheets, such that TSS tests represent the shear loading conditions and CTS represents the normal force to the sheet/sheet interface. The most common parameters monitored in these tests are the peak load, the failure energy at the peak load, and the maximum displacement, which indicate the ductility and energy absorbing capacity of a weld [40, 42, 43, 62].

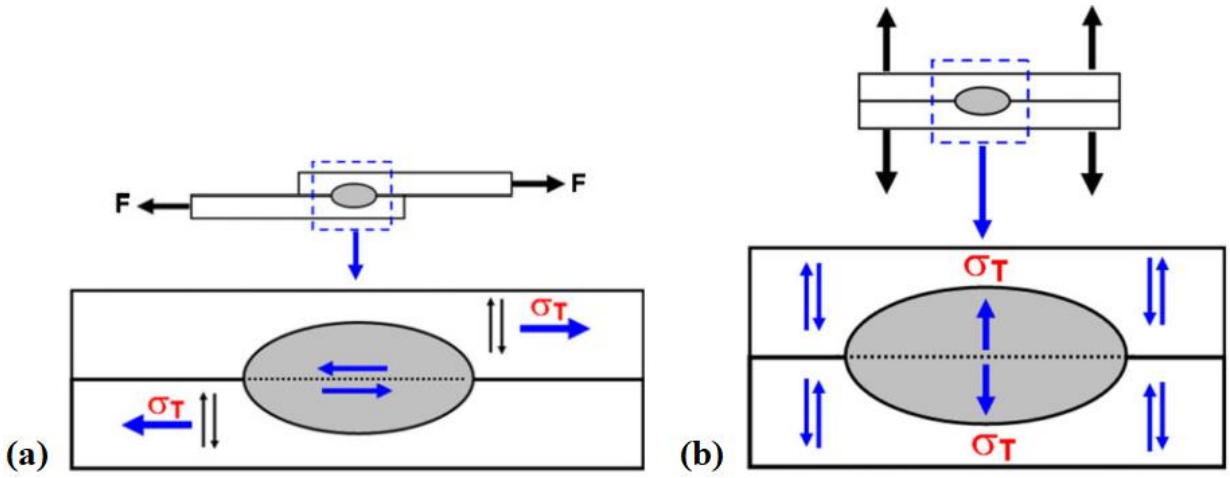


**Figure 2.11: Stress distribution in a weld during (a) TSS and (b) CTS.** Adapted from **[40]**.

Finally, the failure mode of a spot weld is a qualitative measure of mechanical properties, with pull-out failure (PF) and interfacial failure (IF) being the main fracture modes in welded joints, where the stress concentration caused by the weld's notch determines the deformation and fracture mode when a sample is loaded [40, 42, 63–65]. Various sources further classify the welds' fracture modes into more categories, such as partial pull-out and partial interfacial failure. Figure 2.12 shows a wide variety of fracture modes seen in RSW.

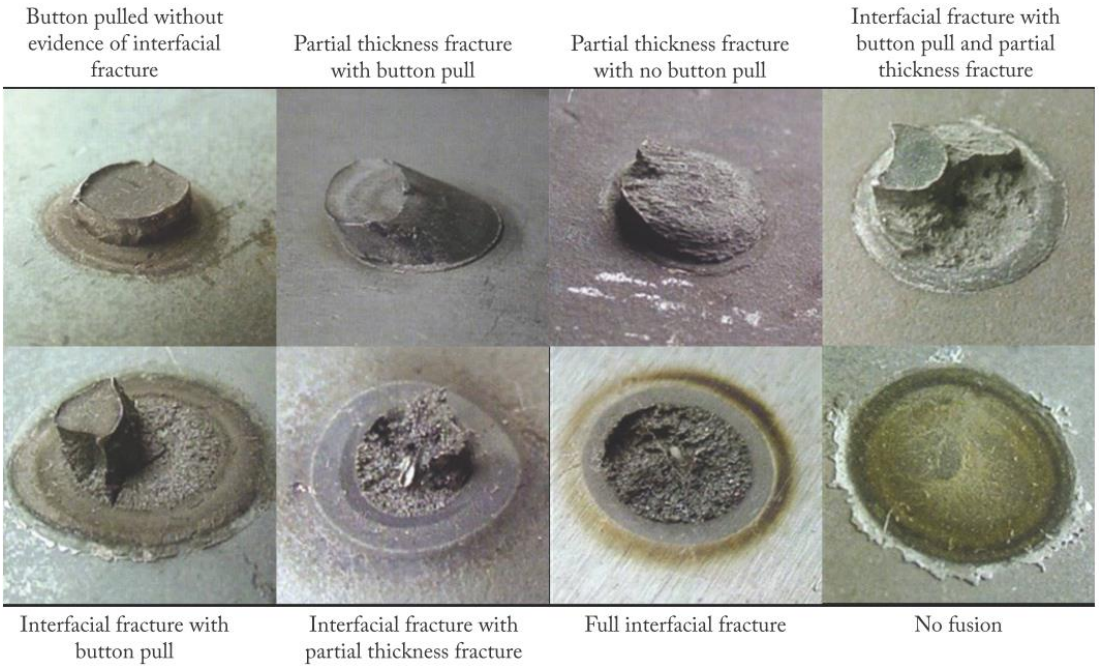


**Figure 2.12: Spot weld fracture modes [43].**

The relationship between the failure mode and the load-bearing and energy absorption capacity of spot welds has been a diverging topic in the literature, with some groups stating that it should not be considered as a single criterion to judge weldability. In contrast, others agree that failure mode significantly influences the welds' mechanical performance [40, 66]. Interfacial failure, where the crack propagates through the FZ, is generally related to low crashworthiness, while pull-out failure shows better mechanical properties. It should be noted that in the RSW of AHSS, fracture modes other than pull-out may also present good mechanical properties, as full button pull-outs are less common due to the nugget's increased hardness, and failure modes such as partial or full interfacial failures may also be related to high strength values [43]. The following section further describes the resistance spot welding behavior of these advanced steels and how it differs from conventional automotive alloys.

## 2.3 RSW of Advanced High Strength Steels

Compared to conventional steels used in the automotive alloys, AHSS have more complex microstructures and higher alloying additions, which are the main reasons why the implementation of these steels in automotive applications has been followed by welding challenges [43, 67]. During the RSW process, AHSS welds undergo complicated microstructural transformations, affecting the joint's failure behavior and mechanical properties. These difficulties are related to AHSS welds being more susceptible to solidification shrinkage and expulsion during the weld cycle, the occurrence of hardening and softening in the HAZ, and a higher tendency of the welds to fail in interfacial fracture mode [40, 50, 68].

In order to better understand and control these transformations, various studies and investigations are being developed on the topic of RSW of AHSS. The following sections provide an overview of the current findings related to the steels, which are the focus of this research.

### 2.3.1 RSW of Dual-Phase Steels

The main issues associated with RSW of dual-phase steels include its high tendency for expulsion and formation of shrinkage voids, high susceptibility to interfacial failure, and the occurrence of HAZ softening, which plays an essential role in the mechanical properties of DP welds. [69–71]. Due to its widespread use in automotive applications, a considerable amount of literature has been developed on the welding of different grades of these steels, with relevant findings to this study being summarized in the following paragraphs.

Wang et al. [72], Zhao et al.[71], and Kishore et al.[73] investigated the resistance spot welding behavior of DP590 / DP600 joints, looking at their load-bearing capacities and failure behaviors. Wang et al. focused on the effect of a multi-pulse welding schedule on the behavior of dual-phase steel joints, finding that the multi-pulse tempering impacted the nugget size and mechanical properties of the welds under tensile-shear load, with the decomposition of martensite under the high temperatures of the weld schedule being related to an improvement on the mechanical performance of the joints. Zhao et al. found that welding defects are commonly seen when extreme process parameters are employed, such as high currents and long welding times, and that the occurrence of solidification cracks and voids are often accompanied by expulsion. Kishore et al. studied the optimization of RSW of galvannealed dual-phase steels, looking for optimal welding parameters to achieve maximum load-bearing capacity. The research found that the weld strength depended primarily on nugget diameter. It also discussed how the transition from interfacial to pull-out failure modes depends not only on nugget size but also on the change in the fracture's micro mechanism from trans-granular cleavage and quasi-cleavage to ductile mode. The relationship between nugget size, failure mode, and load-bearing capacity in DP600 is shown in Figure 2.13, where it can be seen that tensile shear loads increase with an increase in nugget diameter, and that at a critical nugget diameter the fracture mode changes from partial interfacial failure to pull-out failure.

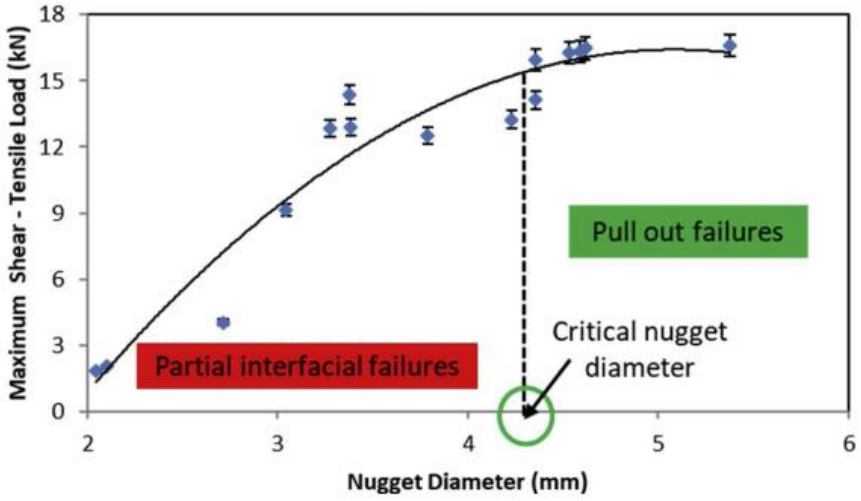


**Figure 2.13: Variation of failure mode and maximum tensile-shear load with nugget diameter on the RSW of 1.3mm thick DP600 [73]**.

Similarly, Sawanishi et al.[52], and Chabok et al.[74] looked at the mechanical performance and failure mode of DP980 / DP1000 resistance spot welds. Sawanishi et al. investigated the effect of multi-pulse weld schedules on DP980, finding that pulsing led to an improvement in the joints' cross-tension strength and a

change in failure mode from partial interfacial fracture to pull-out fracture. These results were corroborated by Chabok et al.'s research, which also concluded that a double pulse weld schedule led to an enhancement in cross-tension strength and energy absorption capability. Chabok et al. further investigated the microstructural changes that resulted in this observation, relating it to the severe softening in the HAZ of welds, which changed the joints' fracture behavior. The cross-sectional view of the CTS samples is shown in Figure 2.14.

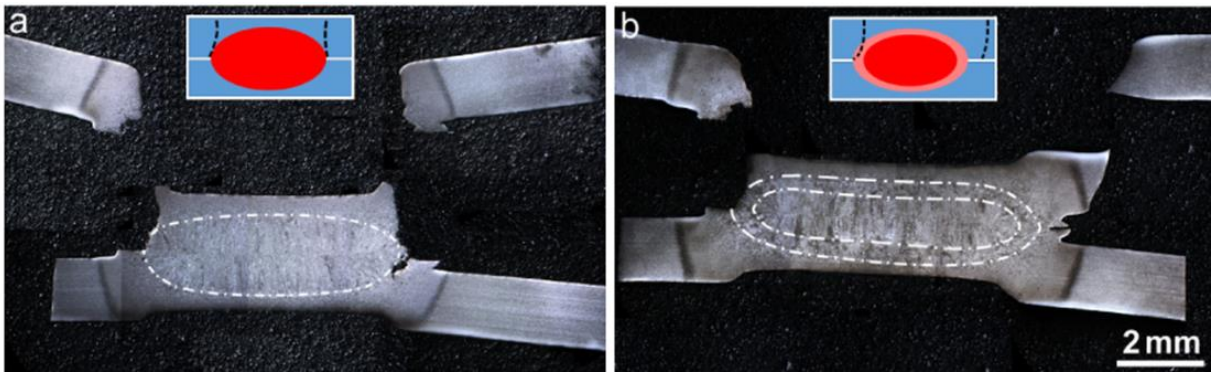


**Figure 2.14: Cross-section of CTS samples of (a) single pulse and (b) double pulse weld [74]**.

Figure 2.14(b) shows clear evidence of failure in the HAZ of the weld, which is commonly related to HAZ softening. Heat-affected zone softening is a well-understood phenomenon in resistance spot welding, and it is widely accepted that it is unavoidable in dual-phase steel welds. As discussed in section 2.1.3 of this review, DP steels are characterized by a composite-like microstructure containing a combination of ferrite and martensite. Martensite is a thermally unstable phase, decomposing and tempering at high temperatures, which leads to a decrease in its hardness [75]. This occurs in several thermal processes, such as welding, joining, and laser heat treatments. The degree of softening is heavily affected by the initial martensite content of the structure, the steel chemistry, heat input, and pre-strain. In resistance spot welds, softening often occurs in the subcritical HAZ, where changes in the material's microstructure, namely tempering of the martensite, leads to changes in mechanical properties such as a decrease in tensile strength when compared to that of the base metal [26, 75, 76].

### 2.3.2 RSW of Quenching and Partitioning Steels

Due to Q&P's relative novelty, there is still limited research on these alloys' general weldability. Guo et al. [77] and Li et al. [78] investigated the microstructure and mechanical properties of laser-welded Q&P980, finding that although softening occurs in the sub-critical HAZ, the welded joints still failed at the base material, which was the weakest point in the joint. These results were corroborated by Lin et al. [79]

when looking at the friction stir welding behavior of Q&P980, as this group also found that that the decrease in hardness seen in the sub-critical HAZ did not affect the failure behavior of the joints, which again failed in the base material. However, resistance spot welding trials done on Q&P980 steels did not all agree with this observation. While Wang et al. [80] reported seeing clear HAZ softening, where cracks initiated at the interface between sheets and propagated through the softened HAZ, Lei and Pan [81] claimed seeing no evidence of softening in the RSW of Q&P980. Wang and Speer [1] published in 2013 an overview of the Q&P process and its application in the automotive industry, stating that no obvious HAZ softening had been observed in the RSW of Q&P980. Liu et al. [82] also observed no HAZ softening, claiming instead that the crack-propagation behavior was related to the presence of a liquation cracking in the partially melted zone (PMZ) of the welds. Figure 2.15 compares the hardness profiles reported in Wang et al.'s and Liu et al.'s works. Based on the literature available so far, it is not clear if Q&P resistance spot welds have a tendency for HAZ softening and whether the possible occurrence of this softening leads to changes in the failure mode of the welds as it does in dual-phase steels.

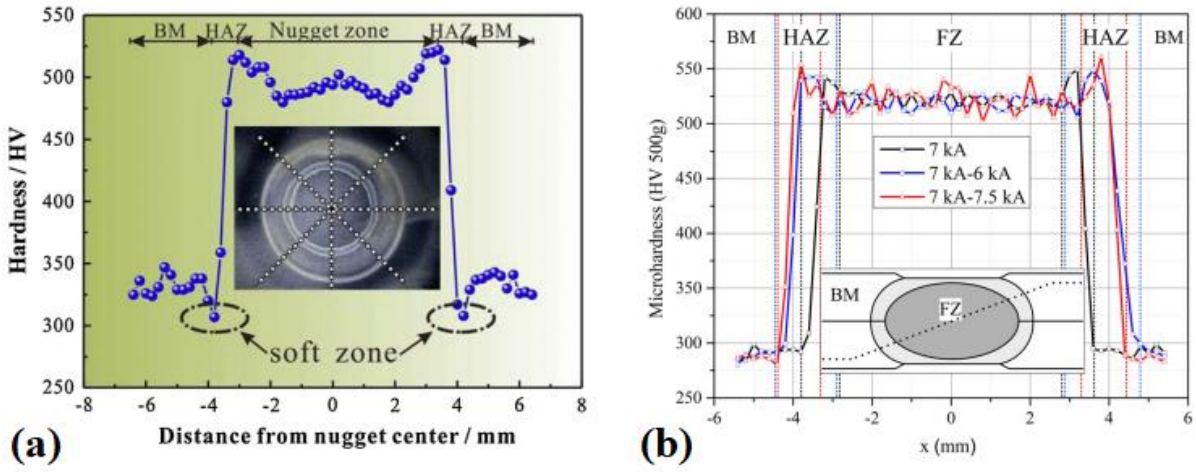


**Figure 2.15: Microhardness profiles of Q&P980 welds showing (a) HAZ softening and (b) no softening across different welding schedules.** Adapted from **[80]** and **[82]**.

Overall, the studies done on RSW of Q&P steels report high fusion zone hardness compared to that of the base material due to the formation of martensite and martensite being the predominant microstructure across the weldments [80–83]. Regarding fracture modes, both interfacial and pull-out modes were observed, with Liu et al. [82] reporting that TSS samples failed in interfacial failure when a single pulse was used and in partial pull-out mode when double-pulse was used and that all CTS samples failed in partial interfacial mode. Conversely, when Chen et al. [84] compared the use of a slightly concave electrode to the

conventional dome-radius electrode, it was reported that all TSS samples in the study failed in pull-out mode.

As for the mechanical properties seen in Q&P welds, Figure 2.16 provides an overview of the normalized TSS and CTS values for Q&P980 reported by Wang and Speer [1], Wang et al. [80], Lei and Pan [81], and Liu et al. [82]. The strength values were normalized to better account for the different material thicknesses and weld diameters, using the method described by Dancette et al. [60]. The normalized weld strength $S_{max}$ is expressed by the equation:

$$S_{max} = \frac{F_{max}}{t_{sheet}\, d_n} \qquad \text{(Eq. 2.3)}$$

where $F_{max}$ denotes the maximum load, $t_{sheet}$ is the sheet thickness, and $d_n$ is the weld diameter.

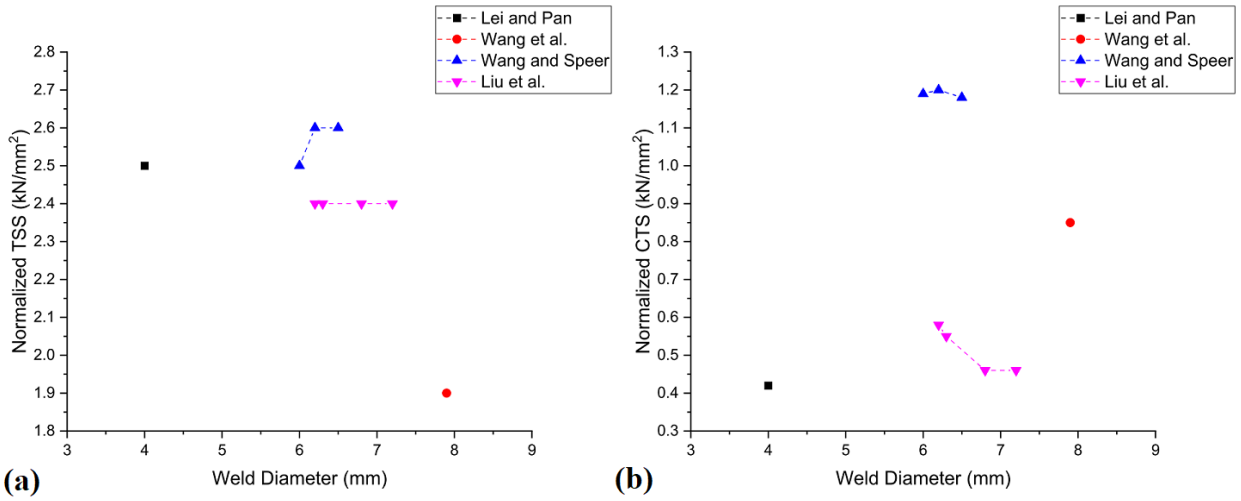


**Figure 2.16: Normalized weld strength reported in the literature for Q&P980 steels showing (a) TSS values and (b) CTS values.**

Finally, it is worth noting that other groups also published their results on various aspects of the resistance spot welding behavior of Q&P steels. Fan et al. [85, 86] discussed the fracture strength where spallation occurs (spall strength) and the quasi-static uniaxial compression properties of Q&P980, finding that due to differences in thermal cycles during welding, the flow stress of the FZ martensite is higher than that of the base material martensite. Ling et al. [87] observed the liquid metal embrittlement (LME) cracking of Q&P980, finding shallow, intergranular cracks that were mainly located at the weld's indentation edge and slope. Spena et al. [88–91] and Ozturk Yilmaz et al. [92] investigated the dissimilar resistance spot welding of Q&P980 and Q&P1180 with other AHSS, including TRIP, TWIP, and DP steels. As expected, diverging

mechanical behaviors were seen between the combinations, but overall Q&P steels were able to obtain sound RSW joints when welded with other AHSS.

### 2.3.3 Transient Softening at the Fusion Boundary in RSW

Recent studies have described the occurrence of a transient softening at the fusion boundary in the RSW of hot-stamped 22MnB5 and Dual-Phase steels. This phenomenon has been commonly referred to as the halo, as it resembles a halo-like ring located between the weld nugget and the coarse-grained HAZ. Longer welding times, generally used to increase the process window for resistance spot welds, have been shown to lead to a more pronounced softened region at the fusion boundary [93–95].

It has been proposed that the halo is due to the carbon redistribution at the fusion boundary through the combination of segregation due to the C solubility differences between liquid and solid, and δ-Fe formation in the peritectic region [93]. This occurs when the molten nugget boundary remains static towards the end of the welding cycle, resulting in the formation of softer carbon-depleted martensite in the fusion boundary's adjacency [96]. Evidence of the halo can be found through microhardness mapping, where hardness drops are seen around the fusion boundary, as shown in Figure 2.17.

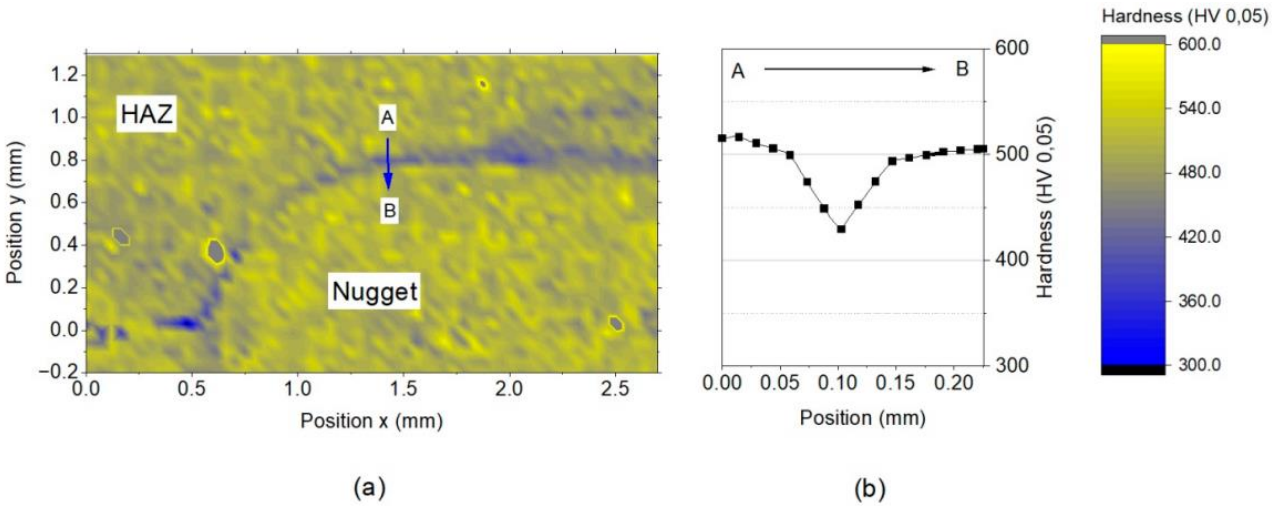


**Figure 2.17: (a) Hardness mapping of a RSW of 22MnB5 with a welding time of 630 ms and (b) hardness line across the fusion boundary [93]**.

The halo has an average width of approximately 104 μm according to literature reports, and it has been related to changes in the fracture mode of the welds, where severe softening was connected to a slight increase in peak CTS values and higher energy absorption [94, 96]. However, this phenomenon has been given limited attention in the literature. Mohamadizadeh et al. [96] described in 2020 the failure mechanism

in the RSW of aluminum-silicon coated 22MnB5, finding that failure was located around the fusion boundary for both CTS and TSS tests, as shown in Figure 2.18. The study concluded that even though the hardness at the sub-critical HAZ was lower than that of the fusion boundary, the stress concentration at the weld notch initiated the failure, which then propagated through the low strength path provided by the halo.

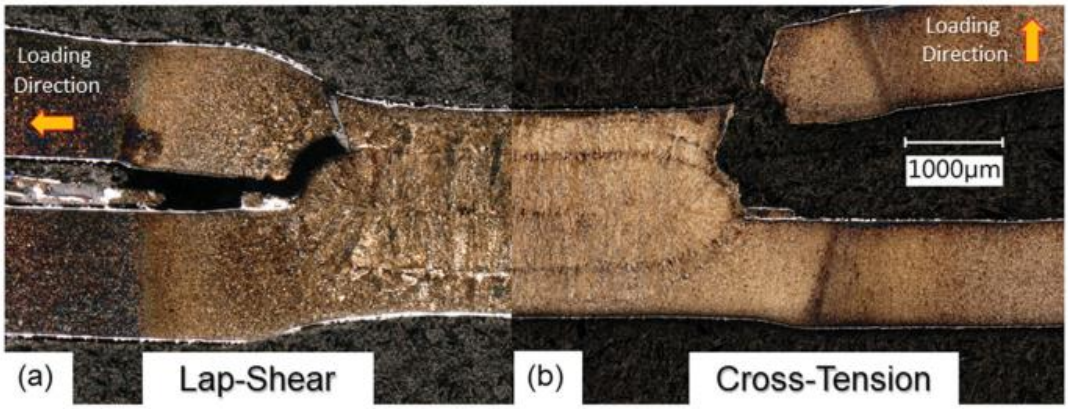


**Figure 2.18: Cross-section of a RSW of 22MnB5 after failure for (a) lap-shear and (b) cross-tension test.** Adapted from **[96]**.

# Chapter 3
# Methodology

This work's main objective was to understand the microstructure development and mechanical behavior of the resistance spot welding of Q&P steels and apply the findings to optimize the weldability of these steels. Two experiments were designed to study the resistance spot welding behavior of Q&P steels, first using standard parameters as described by AWS D8.9M, and then using various welding schedule parameters, including pulsing current and cooling time, in order to explore the effects in the failure behavior and mechanical performance of Q&P joints. This chapter presents the welding techniques used for the studies, as well as materials, preparation methods, and characterization procedures.

## 3.1 Materials

This research was performed using industrially produced sheets of 1.2 mm thickness of hot-dipped galvanized (GI) DP980 and Q&P980 provided by ArcelorMittal Dofasco, sampled from a production run for the automotive industry. Table 3.1 presents the chemical composition of the as-received steels, where the carbon equivalent of the materials was calculated according to the method described by Yurioka et al. [97], expressed by the equation:

$$CE = C + A(C)\left\{\frac{Si}{24} + \frac{Mn}{6} + \frac{Cu}{15} + \frac{Ni}{20} + \frac{Cr + Mo + Nb + V}{5} + 5B\right\} \quad \text{(Eq. 3.1)}$$

where CE denotes the carbon equivalent, and A(C) can be found by the expression:

$$A(C) = 0.75 + 0.25\ tanh\{20\ (C - 0.12)\} \quad \text{(Eq. 3.2)}$$

The tensile test specimens were cut following the ASTM E8/E8M sheet type specimen specification [9]. The measured mechanical properties of the base metals used in this study are shown in Table 3.2.

**Table 3.1: Chemical composition of DP980 and Q&P980**

| Material | C (wt%) | Mn (wt%) | P (wt%) | S (wt%) | Si (wt%) | Cr (wt%) | Carbon Equivalent |
|---|---|---|---|---|---|---|---|
| DP980 | 0.10 | 2.1 | 0.013 | 0.004 | 0.34 | 0.2 | 0.42 |
| Q&P980 | 0.23 | 2.0 | 0.009 | 0.004 | 1.00 | 0.2 | 0.65 |

**Table 3.2: Mechanical properties of DP980 and Q&P980**

| Material | UTS (MPa) | YS (MPa) | Elongation (%) | Hardness (HV0.2) |
|---|---|---|---|---|
| DP980 | 1045 | 862 | 13.8% | 314 |
| Q&P980 | 1047 | 855 | 19.9% | 323 |

## 3.2 Resistance Spot Welding

The materials were sheared and waterjet cut into smaller coupons for the welding experiments. Coupons with dimensions of 25 mm x 25 mm were used for metallurgical analysis, and coupons with dimensions of 100 mm x 25 mm were used for chisel and peel tests. Coupons for tensile shear strength and cross tension strength were cut following the AWS D8.9M standard [9], with dimensions of 105 mm x 45 mm for the shear tension samples and 150 mm x 50 mm for the cross tension samples. All coupons were cleaned with ethanol before welding.

### 3.2.1 Welding Equipment

Resistance spot welding was conducted using a medium-frequency direct current (MFDC) pedestal spot welder with a maximum secondary current of 60 kA and a maximum electrode force of 25 kN (Figure 3.1). The welder used a Bosch Rexroth PSQ 6000 controller with a BOS 6000 operating interface, and the electrodes were RWMA (Resistance Welder Manufacturer's Association) Group A, Class II, domed electrodes with a dressed face diameter of 6 mm [98]. The electrodes had a flat contact face. Welding current, voltage, and resistance were measured with a data acquisition system connected to the controller. The system recorded current and voltage values for every millisecond of the weld cycle and used the acquired data to calculate real-time resistance.

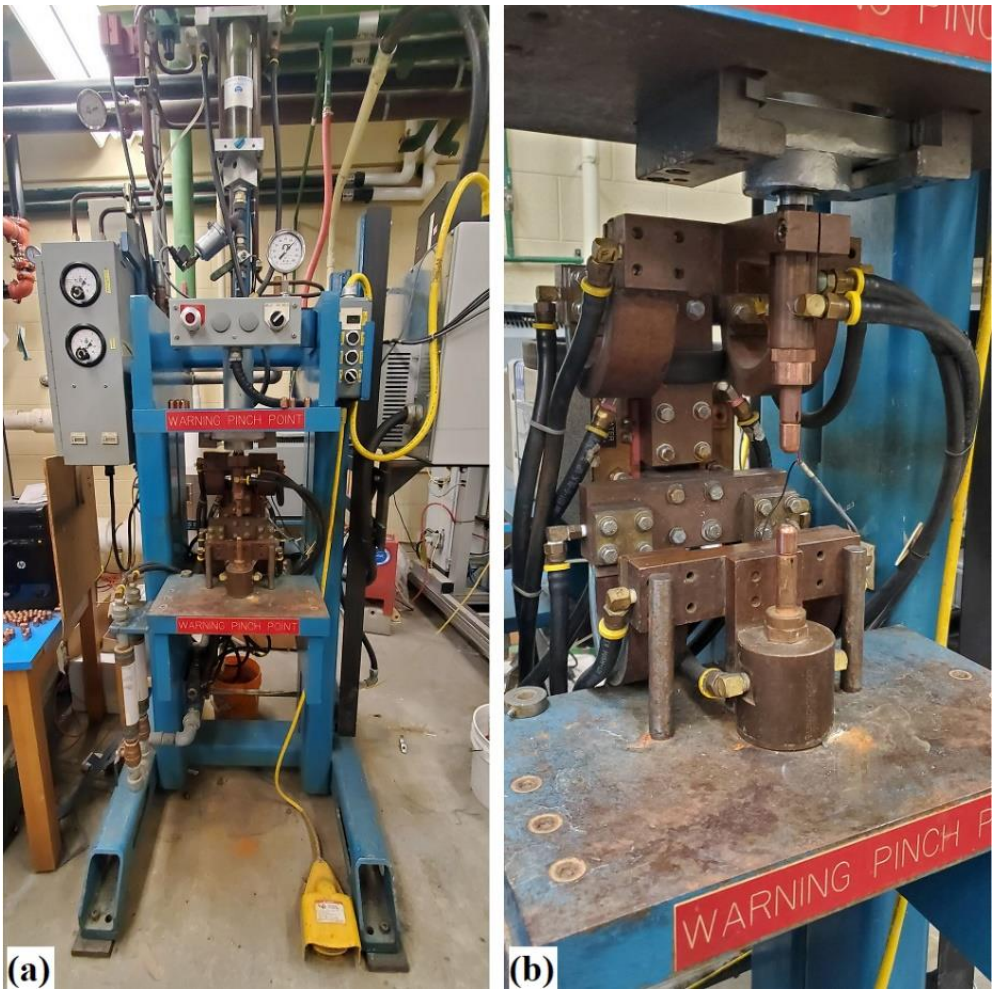


**Figure 3.1: (a) MFDC resistance spot welder and (b) detail showing the welding setup with domed electrodes.**

### 3.2.2 Single Pulse Welding Parameters

In the first study, the welding parameters followed the specification given by AWS D8.9M [9]. Given that both DP980 and Q&P980 sheets had the same thickness and tensile strength, parameters such as force, recommended weld cycles, squeeze time, and hold time were the same for both materials. Welds were made with a single pulse schedule, and the currents and weld times were varied to obtain the operational window where acceptable welds were achieved. The cooling water flow rate was 4 L/min, and the electrode force was 4 kN. Figure 3.2 shows a schematic for the welding parameters used for single pulse welding, where the welding times are given in units of cycles (cy) at a line frequency of 60 Hz, which is equal to 16.67 ms.

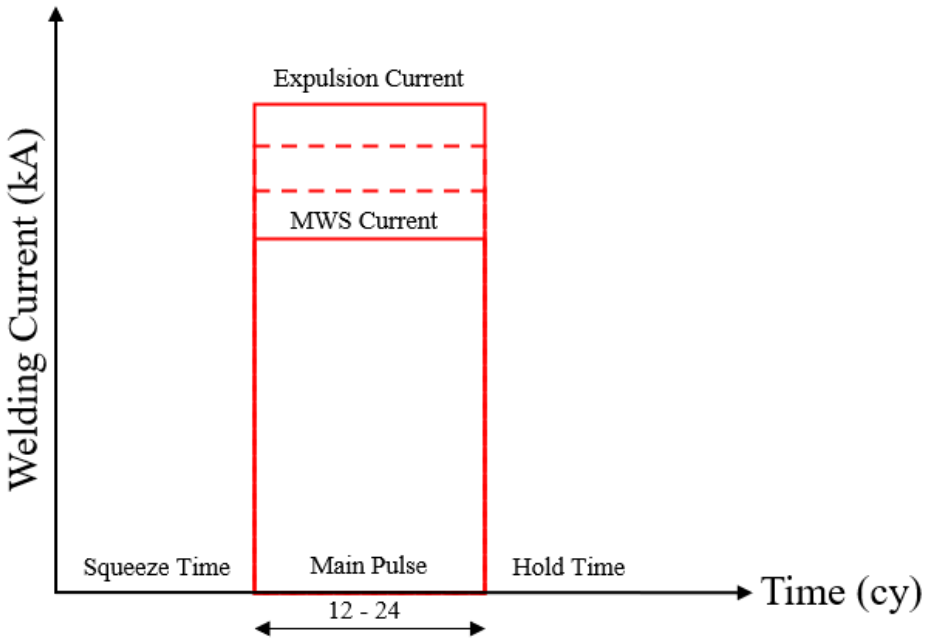


**Figure 3.2: Schematic for single pulse resistance spot weld.**

### 3.2.3 Double Pulse Welding Parameters

For the second study, parameters such as force and cooling water flow rate followed the specification given by AWS D8.9M [9]. The welds were made with a multi-pulse schedule, where the first pulse followed the recommend weld time of 16 cycles, and the selected current was 7.5 kA. Different values of second pulse current, second pulse weld time, and cooling time between pulses were applied to investigate their effect on the weldment. The cooling time between the pulses varied between 2 and 4 cycles, the second pulse time varied between 4 and 8 cycles, and the second pulse current varied between 6 kA and 9 kA, as shown in Figure 3.3.

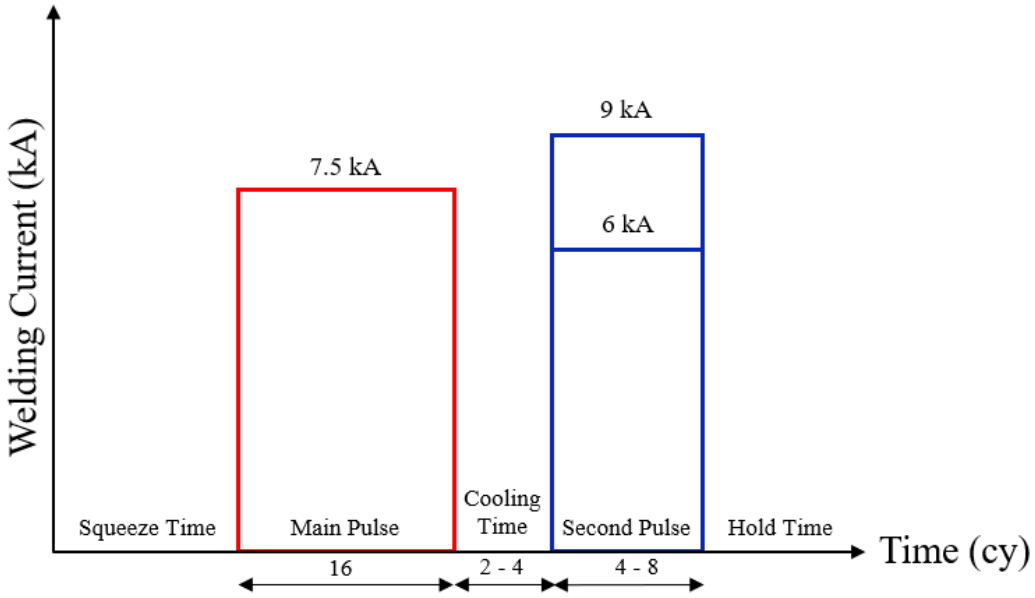


**Figure 3.3: Schematic for double pulse resistance spot weld.**

The parameters for both single pulse and double pulse welding schedules are detailed in Table 3.3.

**Table 3.3: Welding parameters for single and pulsed welding schedules.**

| Schedule | Force (kN) | Cooling (L/min) | Squeeze Time (cy) | Main Pulse Time (cy) | Second Pulse Time (cy) | Cooling Time (cy) | Hold Time (cy) |
|---|---|---|---|---|---|---|---|
| Single Pulse | 4.0 | 4 | 45 | 12 to 24 | - | - | 5 (short)<br>90 (long) |
| Double Pulse | 4.0 | 4 | 45 | 16 | 4 to 8 | 2 to 4 | 5 (short)<br>90 (long) |

## 3.3 Metallographic Characterization

The metallographic analysis was carried out following a conventional preparation method. Each weld was cross-sectioned using a metallurgical abrasive cut-off saw with a continuous application of coolant, mounted, polished to a 1 μm diamond finish, and etched with a 2% Nital solution for 5 seconds.

The microstructure was observed using an Olympus BX51M system metallurgical microscope, and scanning electron microscopy (SEM) was performed in a Zeiss FESEM 1530 field emission scanning electron microscope.

## 3.4 Mechanical Testing

### 3.4.1 Weld Size Measurement

The nugget size was measured using the peel test (Chapter 4) and chisel test (Chapters 5 and 6), as well as by cross-sectioning the weld and measuring the nugget size through microscopy for better accuracy. In both peel and chisel tests, the weld nugget was pulled out and directly measured with a caliper. For the microscopy measurements, the sample preparation followed the metallographic characterization procedure described above in section 3.3.

All welds were measured across their minimum and maximum axes, and the reported weld sizes were calculated by finding the average of the two measurements for each sample as described by AWS C1.1M [99]. The procedure for measuring the weld nugget following this specification is shown in Figure 3.4.

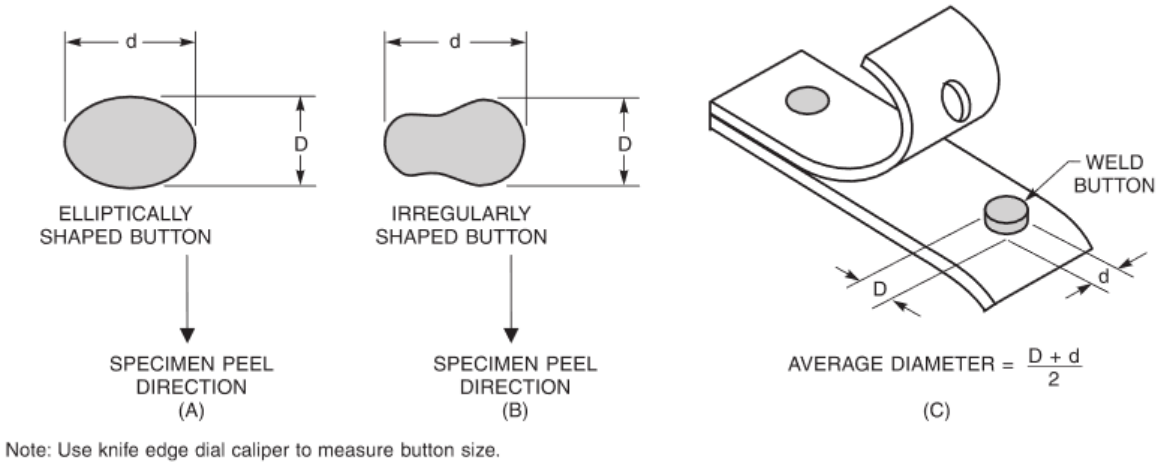


**Figure 3.4: Measurement of a weld button (a) Elliptically shaped button, (b) Irregularly shaped button, and (c) Average diameter calculation [99].**

### 3.4.2 Microhardness

Microhardness tests were made using an automated Clemex CMT machine with a Vickers indenter, using a load of 200 g and a dwell time of 10 s. The indentation spacing was 0.2 mm as required by AWS D8.9M [9] to avoid the work hardening effect from previous indentations, and a staggered pattern was used to obtain more accurate measurements in the HAZ, as shown in Figure 3.5.

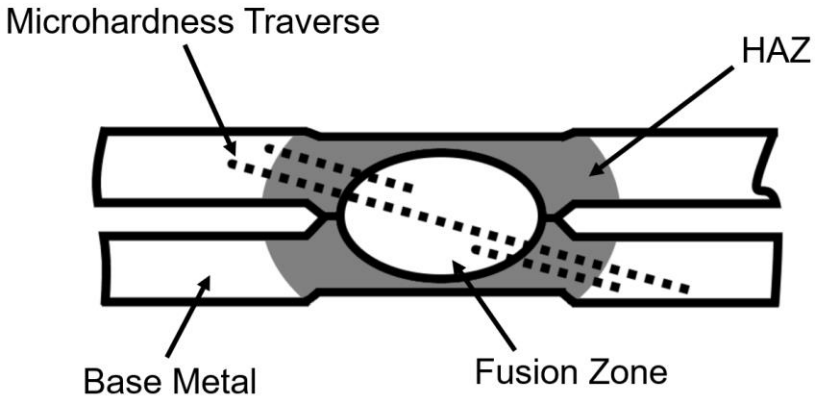


**Figure 3.5: Schematic of a cross-sectioned weld and microhardness traverse.**

### 3.4.3 Tensile Testing

The tensile shear strength (TSS) and cross tension strength (CTS) tests were performed using an Instron testing machine, Model 4206, and a Tinius Olsen model H10KT tensile tester, shown in Figure 3.6. The crosshead speed was 10 mm/min, and the strength samples were welded following the geometry described in the AWS D8.9M standard [9]. The test coupons were prepared according to the size requirements shown in Figure 3.7.

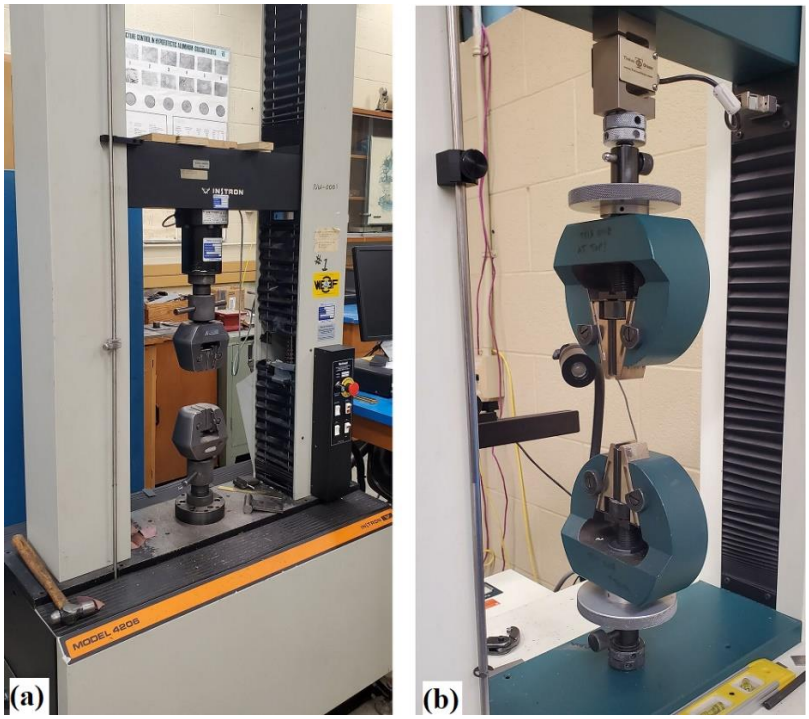


**Figure 3.6: Tensile testers (a) Instron Model 4206 and (b) Tinius Olsen model H10KT.**

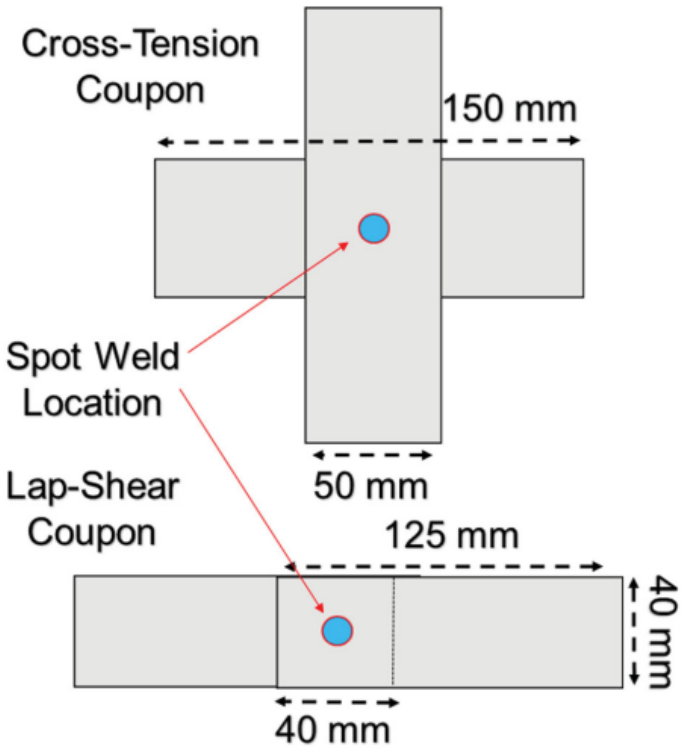


**Figure 3.7: Strength test coupon configuration and size [96].**

## 3.5 Computational Simulation

Simulation of the detailed effects of welding on Q&P980 sheets was performed using the finite element code Sysweld® Version 2018.0 (ESI-Group, 2018). Sysweld® is a finite element method (FEM) software package that models the specific problems encountered in welding by simulating the interactions between electrical, metallurgical, and mechanical phenomena of the welding process [100, 101]. As described by Eshraghi et al. [102], the Sysweld® model accounts for the following physical and metallurgical interactions in the simulations: the interaction between the electro-kinetics and heat transfer via the Joule effect, the heat transfer and phase transformations through latent heat, and the heat transfer, electro-kinetics, and mechanical behavior via the contact conditions.

This research used a customized electrode mesh modeled by Christopher DiGiovanni. Due to the welded structure's symmetry, only one half was modeled, as shown in Figure 3.8. The mesh was finer in the vicinity of the weld region and coarser far away from HAZ. Four phases were used to simulate the phase transformations, and strong coupling, where every thermal simulation step is followed by mechanical simulation step and geometry actualization, was also used [103]. The chemical composition of Q&P980

shown in Table 3.1 was used as input for the JMatPro® Version 11.2 (Sente Software, 2019) materials modeling software, and the resulting material data be found in Appendix B was input into Sysweld®. The process parameters were as described above in section 3.2.3.

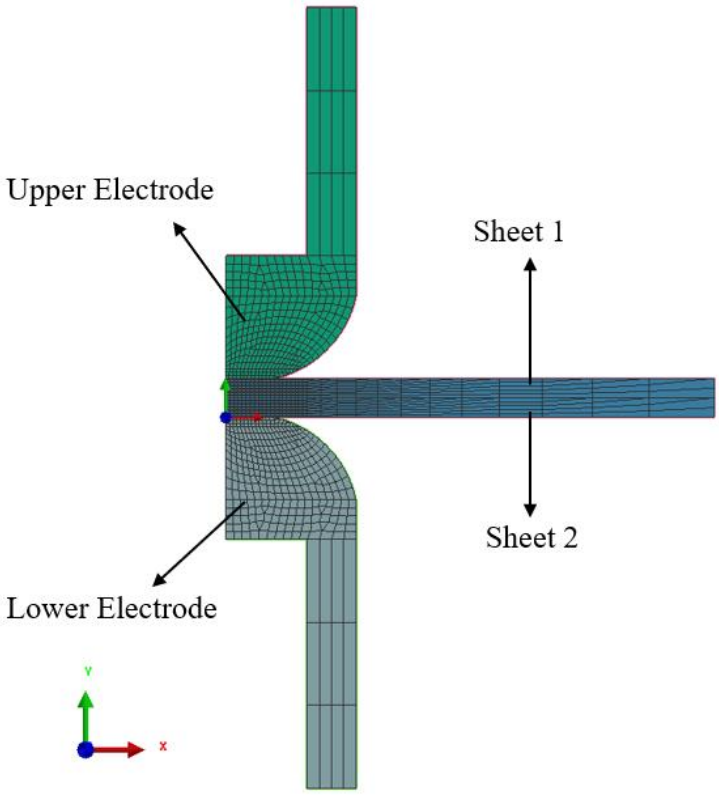


**Figure 3.8: Finite element model.**

## 3.6 Statistical Analysis

All measurements have a degree of uncertainty, and a quantitative statement of the uncertainty associated with a measurement is required to determine if the result is fit for its purpose and consistent with similar results. Statistical analysis can be used to determine the uncertainties in the measurement process [104].

In this study, the reported results' statistical significance was assessed through confidence intervals and significance testing. Standard error propagation techniques were applied to calculate the uncertainty associated with the reported measurements, where all reported errors associated with strength measurements represent a 95% confidence interval.

Linear regression was used to quantify the relationship between weld strength and nugget diameter (Chapter 4) and between weld strength and heat input (Chapter 5). Linear regression analysis was conducted using the data analysis and graphing software OriginPro, Version 2020 (OriginLab Corporation, 2020). The statistical significance of the model was tested using the analysis of variance (ANOVA) method.

# Chapter 4

# Failure Behavior and Mechanical Properties in the Resistance Spot Welding of Quenched and Partitioned Steels

In this chapter, a study is presented to report findings in the microstructure and mechanical properties of Q&P980, relating the post-welded microstructure to the failure behavior when the welds are loaded. The results intend to bring further understanding to the state of knowledge noted in Chapter 2. This was done by comparing the post-welded properties in DP980 with those of Q&P980 under the same welding schedules and elucidating how these microstructures affect crack propagation. The choice of performing the comparison with dual-phase steels derives from the fact that these alloys are well understood and already widely used in the industry. The results of this study are discussed in the following sections.

## 4.1 Base Material Characterization

The first step in understanding the changes during the welding of Q&P steels is understanding the base material itself. Before welding, both materials' base material microstructure was characterized under scanning electron microscopy, as shown in Figure 4.1 and Figure 4.2. Figure 4.1 (a and b) shows the electron micrograph DP980 steel, where clear phases of ferrite (F) and martensite (M) can be identified, with ferrite corresponding to approximately 61% of the structure and martensite to 39%. All the microstructures were characterized according to their morphologies. It was seen that the microstructure of the Q&P980 steel was composed of a ferrite (F) matrix, with martensite (M), tempered martensite (TM), and retained austenite (RA) islands, with ferrite corresponding to approximately 41% of the structure, martensite and tempered martensite corresponding to approximately 51%, and retained austenite to approximately 8%, as seen in Figure 4.2 (a and b). The quantitative analysis of the retained austenite was performed by electron backscattered diffraction (EBSD).

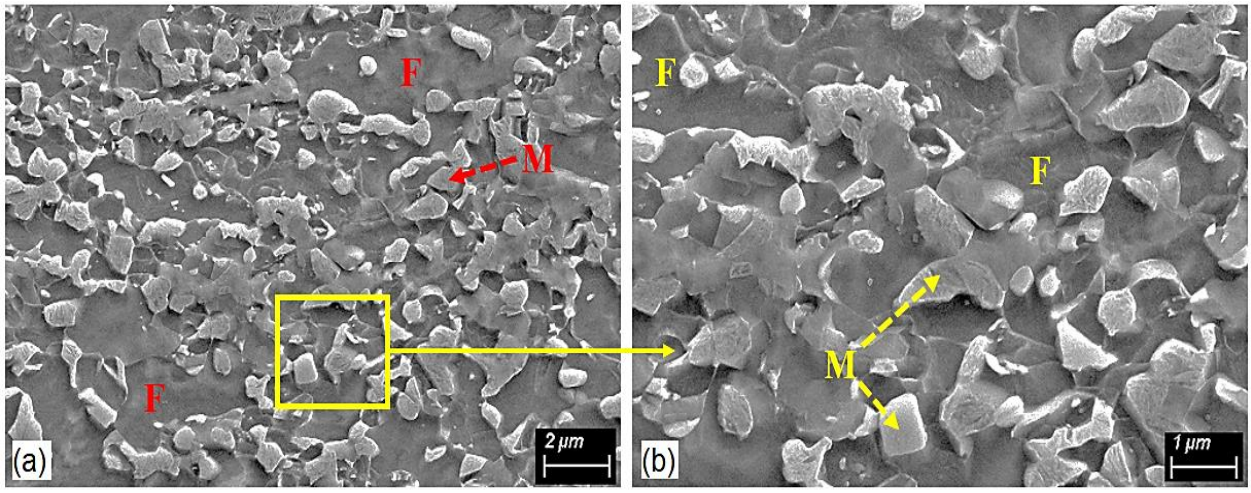


**Figure 4.1: Micrographs of the structures in DP980. (a) Magnification of x4000 and (b) Magnification of x8000. M is Martensite, F is Ferrite.**

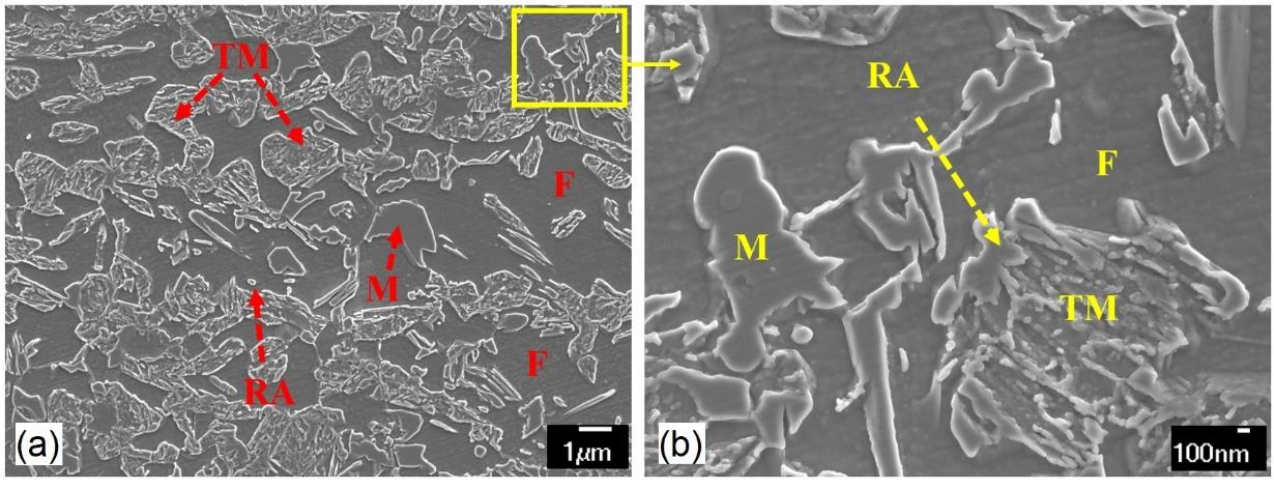


**Figure 4.2: Micrographs of the structures in Q&P980. (a) Magnification of x4000 and (b) Magnification of x15000. M is Martensite, F is Ferrite, TM is Tempered Martensite, and RA is Retained Austenite.**

The microstructure of both materials shows an agreement with what has been previously reported in studies. As discussed in Chapter 2, the literature shows that the final microstructure of Q&P has a 50 to 80% volume fraction of martensite and 10 to 20% volume fraction of retained austenite [1, 7]. The Q&P steel consisted of around 8% RA, which will improve its ductility by the TRIP effect. The fresh martensite

in the microstructure will temper to form TM when the heat is applied, which may induce a localized softened zone in the microstructure.

## 4.2 Weld Lobe

Based on the welding parameters described in Chapter 3, the weld property test was performed, and the weld lobes for the RSW of DP980 and Q&P980 steels were constructed to establish the operational window where acceptable welds are achieved. The experiments were performed at four different weld times. The standard weld time was 270 ms, equivalent to the 16 cycles recommended by AWS D8.9M [9]. The minimum weld time was 200 ms, the maximum weld time was 400 ms, and finally, an intermediary weld time of 340 ms was also used. For each weld time, the current was increased by increments of 100 A, starting at the current required to obtain the minimum weld size (MWS) and ending where expulsion occurs. The MWS for the materials used in this study was 4.38 mm, which corresponds to $4t_{sheet}^{1/2}$, where $t_{sheet}$ is the sheet thickness, as prescribed by AWS D8.9M [9]. All materials used in this study had a sheet thickness of 1.2 mm.

The weld lobes achieved for DP980 and Q&P980 are shown in Figure 4.3. Any current between the minimum and maximum current will achieve an acceptable weld. The weld nugget dimensions were measured by both peel tests and macroscopy, where the values were calculated by finding the average of two measurements for each sample.

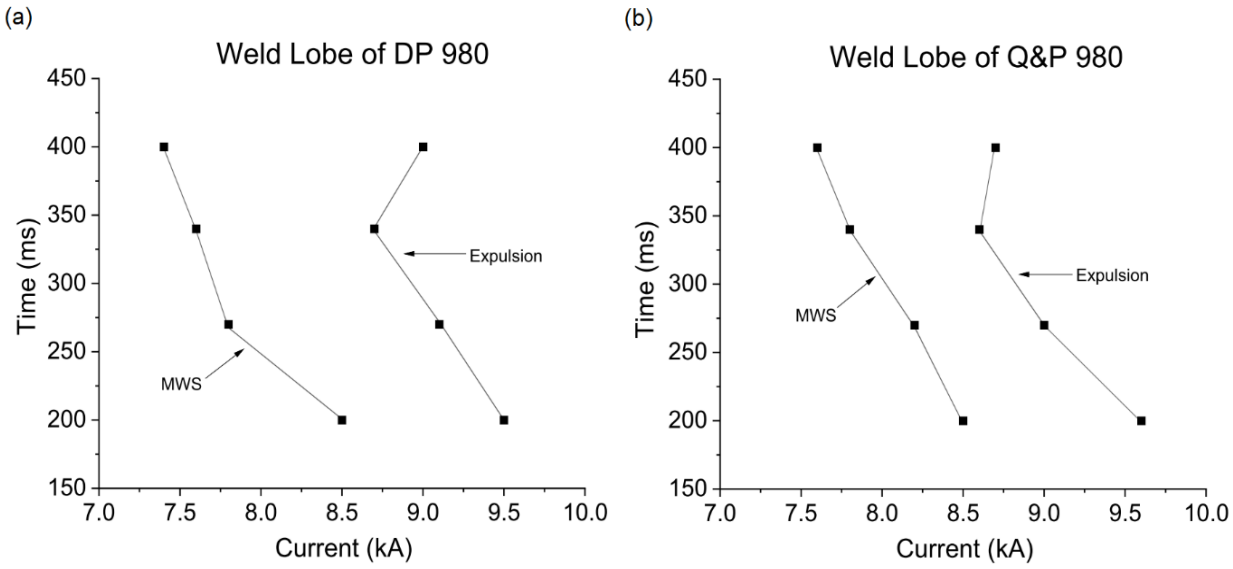


**Figure 4.3: Weld Lobe, where MWS is Minimum Weld Size. (a) DP980 (b) Q&P980.**

As seen in Figure 4.3, DP980 has a welding range varying from 1kA to 2kA. Q&P980 has a narrower welding range, varying from 0.8kA to 1.1kA. Although both materials show an acceptable range, DP980 shows better weldability by requiring smaller currents to achieve MWS and showing expulsion higher currents. Q&P980's higher electrical resistivity can explain its narrower window. The electrical resistivity for DP and Q&P steels are 28.7 μΩ.cm and 36.2 μΩ.cm, respectively, as calculated by the method described by Ludwigson and Schwerer [105]. Alloys with higher resistivity require lower currents to be welded than those that are better conductors of electricity but are also more susceptible to expulsion, leading to narrower welding current ranges [43, 106].

## 4.3 Weld Microhardness and Microstructural Characterization

The microstructures of the weld zone were characterized by scanning electron microscopy. Figures 4.4 and 4.5 show the cross-section and the microstructure within different weld zones for the resistance spot welds of DP980 and Q&P980. The welds for both alloys show the expected microstructure for each zone, with a distinct separation between the base material, heat affected zone regions, including inter-critical HAZ, sub-critical HAZ, coarse-grained HAZ, and fine-grained HAZ, and the fusion zone [107].

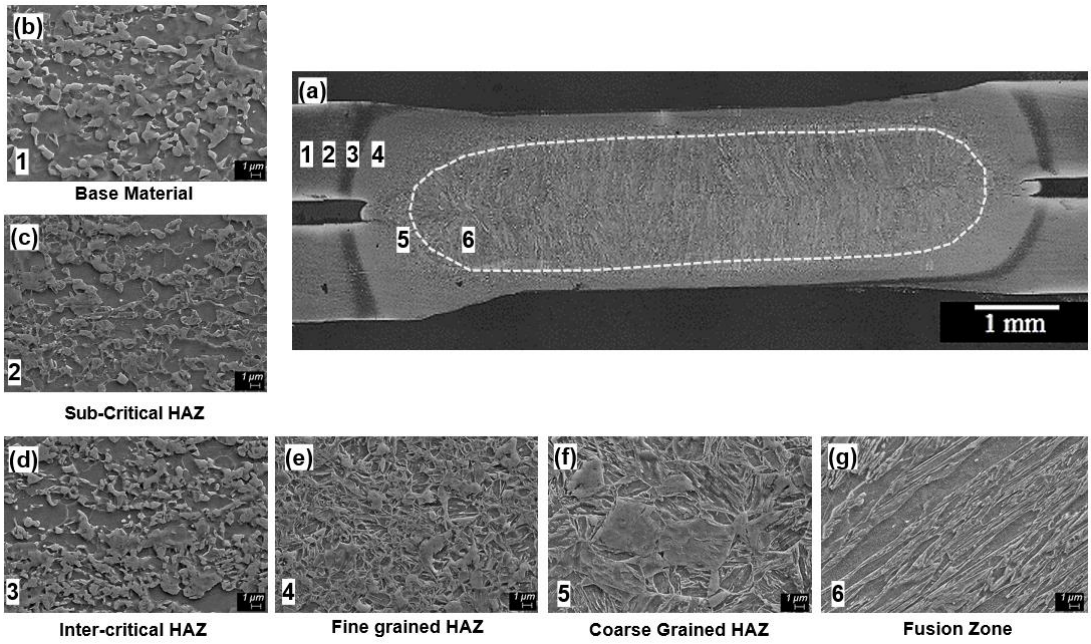


**Figure 4.4: Microstructure within different weld zones for RSW of DP980. (a) Overview of weld microstructure. (b) Base Material (c) Sub-Critical HAZ (d) Inter-Critical HAZ (e)Fine-Grained HAZ (f) Coarse-Grained HAZ (g) Fusion Zone.**

The fusion zone in both DP980 and Q&P980 resistance spot welds is fully martensitic due to their high carbon equivalent and high cooling rate resulting from the RSW process [16]. The heat-affected zone for both materials shows an increase in the martensite fraction with a decrease in the ferrite matrix as the microstructure approaches the fusion zone, which can be seen in Figures 4.4 and 4.5 (c, d, e, and f). Moreover, the structures show extremely fine grains in all regions.

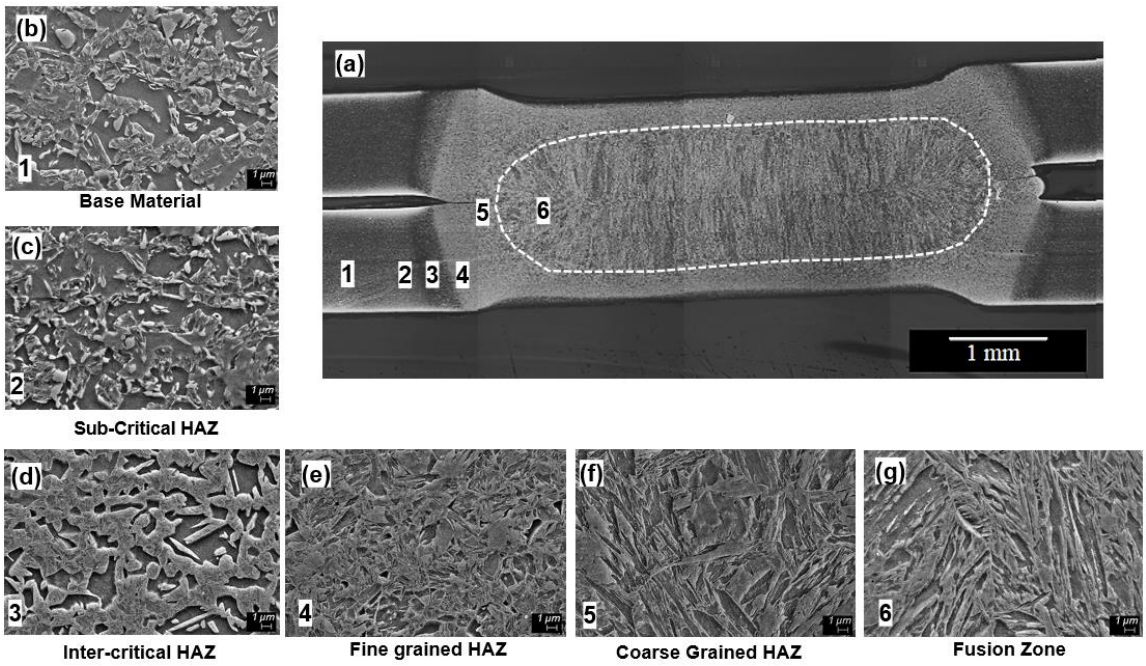


**Figure 4.5: Microstructure within different weld zones for RSW of Q&P980. (a) Overview of weld microstructure. (b) Base Material (c) Sub-Critical HAZ (d) Inter-Critical HAZ (e) Fine-Grained HAZ (f) Coarse-Grained HAZ (g) Fusion Zone.**

Microhardness was also performed to identify the structures in the weld accurately. Figure 4.6 shows the microhardness distribution across the weld of DP980 and Q&P980 steels. The base metal for both steels has similar microhardness. From Table 3.2, the microhardness for Q&P and DP980 was 320 and 323 HV, respectively. The fusion zone in the RSW of DP980 welded at 9kA for 270 ms had a maximum hardness of 430 HV, while the fusion zone in the RSW of Q&P980 under the same conditions had a maximum hardness of 580 HV. All welded samples showed significant hardening at the fusion zone, which agrees with the observed fully martensitic structure found through microscopy. The nugget microstructure of the Q&P980 steel shows fine martensite, as seen in Figure 4.5 (g). However, the martensite found on the DP steel nugget, shown in Figure 4.4 (g), is comparatively coarser.

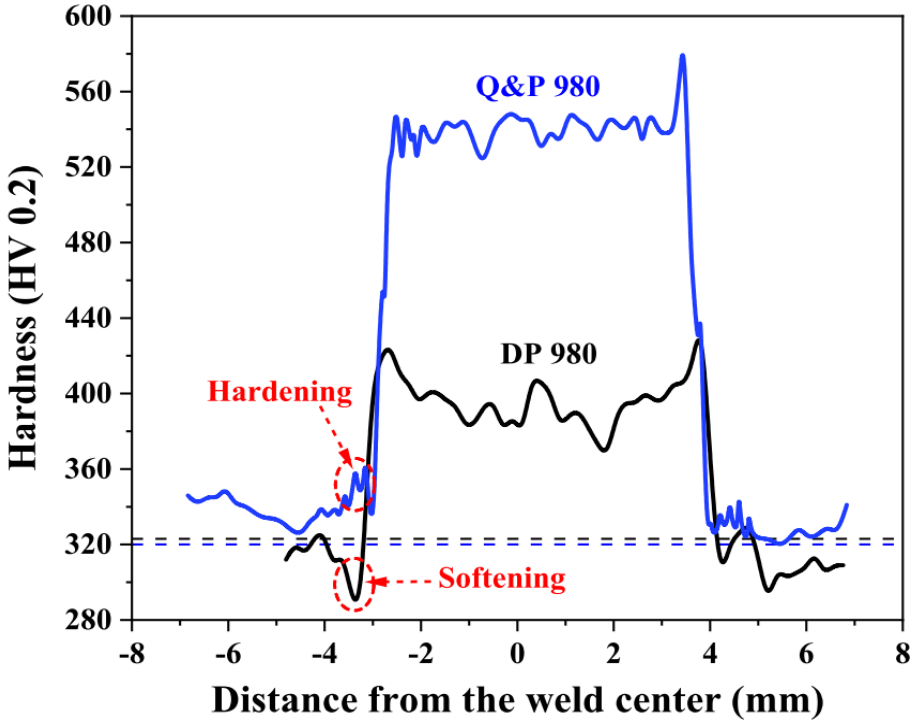


**Figure 4.6: Hardness profile of DP980 and Q&P980 welds.**

DP980 steel shows softening in the HAZ, which is in good agreement with the reported literature, such that tempering of martensite (formation of tempered martensite from the initial microstructures' fresh martensite) makes the HAZ softer than the BM and nugget. As shown in Figure 4.1 and Figure 4.4 (b), the base material for DP980 consists of ferrite and fresh martensite phases. Conversely, Figure 4.4 (c) shows that most of the martensite in the sub-critical heat affected zone has decomposed into tempered martensite. Q&P980 shows evidence of hardening in the HAZ, but no softening was found based on current observation. It has been proposed that the lack of softening is related to the fact that in the tested Q&P980 steel, most of the base material's martensite already in a tempered state. This is in agreement with Figure 4.2 and Figure 4.5 (b), where it can be seen that the base material for Q&P980 has a combination of both fresh and tempered martensite, while Figure 4.5 (c) shows that the microstructure of the sub-critical heat affected zone consists of similar fractions of TM as that of the base material.

The current study depicts that overall, the microstructure of Q&P has a large volume fraction of TM, as shown in Figure 4.2 (b). It has been described in the literature that during welding, the heat experienced by the base metal transforms the fresh martensite into TM and the existing TM into ferrite with fine carbides [75, 76]. Therefore, it is believed that there is a competition between softening and secondary hardening.

This agrees with the current results, where no softening was seen, and instead, Q&P980 shows hardening in the HAZ. Saha et al. [26] also reported that pre-existing carbides in bainite would dissolve during welding and provide C for plate-shaped $M_4C_3$ and needle-shaped $M_2C$ precipitation, leading to the secondary hardening effect in carbide-containing steels. Hence, it is reasonable to conclude that the fine carbides within the large volume fraction of TM in the Q&P980 would transform similar to the carbides in Saha et al.'s work, leading to the secondary hardening phenomena in the studied alloy.

## 4.4 Weld Strength and Failure Mode

Cross-tension strength (CTS) and tensile shear strength (TSS) tests were performed for DP980 and Q&P980 welds under the standard weld time of 270 ms and with the current varying from the MWS until expulsion. Figure 4.7 shows the weld strength results for DP980 plotted against the nugget diameter and the ductility ratio represented by the peak CTS values divided by the peak TSS values. Figure 4.8 shows the results for Q&P980 resistance spot welds.

As expected, an increasing weld diameter leads to an increase of both CTS and TSS values. Values as high as 17.5 kN were found for the TSS test of DP980 welds, and CTS testing showed results as high as 6.9 kN. The ductility ratio (CTS / TSS) ranges from around 0.40 to 0.46. As for Q&P980 welds, TSS values as high as 15.6 kN were measured during TSS testing, and CTS testing showed results as high as 3.2 kN. The ductility ratio for Q&P980 ranges from around 0.20 to 0.21. It can be seen that, for DP980 welds, an increase in nugget diameter was related to a decrease in the ductility ratio, while the same trend is not seen in Q&P980 welds. The ductility ratio shows the extent to which the greater stress concentrations from the cross-tension test affect load failure [43]. Weld defects, coarse-grained microstructures, and HAZ softening are all microstructural heterogeneities from a mechanical standpoint, producing stress concentration factors that result in early fracture of the welds with low load-bearing and energy absorbing capacities [108]. Larger nugget diameters are generated at higher heat inputs, which are also related to more prominent HAZ softening in DP welds, possibly leading to higher stress concentration and the downward trend seen in DP980. The fact that Q&P980 shows no HAZ softening is a possible explanation as to why the opposite trend is seen in its ductility ratio.

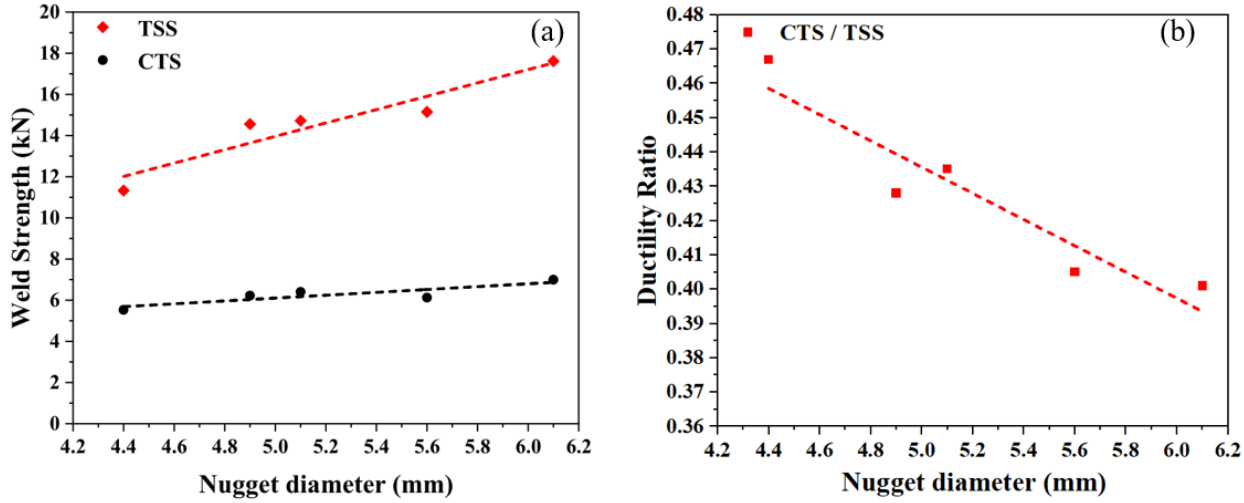


**Figure 4.7: (a) Weld strength for DP980 (b) Ductility ratio for DP980.**

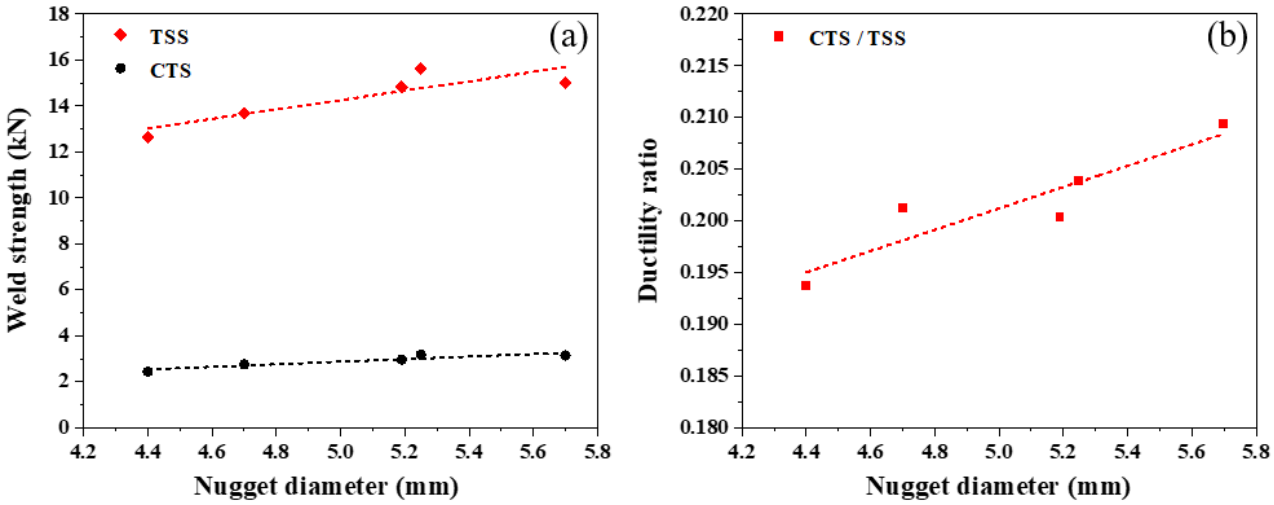


**Figure 4.8: (a) Weld strength for Q&P980 (b) Ductility ratio for Q&P980.**

These results are comparable to those previously reported in the literature, as discussed in Chapter 2 and Figure 2.13. For the same sheet thickness of 1.2 mm, Lei and Pan [81] reported peak TSS values for Q&P980 of 18.5 kN and peak CTS values of 5.8 kN, with a ductility ratio of approximately 0.32. For a sheet thickness of 1.6 mm, Wang et al. [80] reported a peak TSS value for Q&P980 of 23.7 kN and peak CTS of 10.8 kN, with a ductility ratio of 0.46. Finally, for a sheet thickness of 1.8 mm and considering the single pulse weld schedule, Liu et al. found peak TSS values around 27 kN and CTS around 4.8 kN, with a

ductility ratio of approximately 0.18. Figure 4.9 shows a comparison between the ductility ratio for Q&P980 found in this study and the values reported by Lei and Pan, Wang et al., and Liu et al.

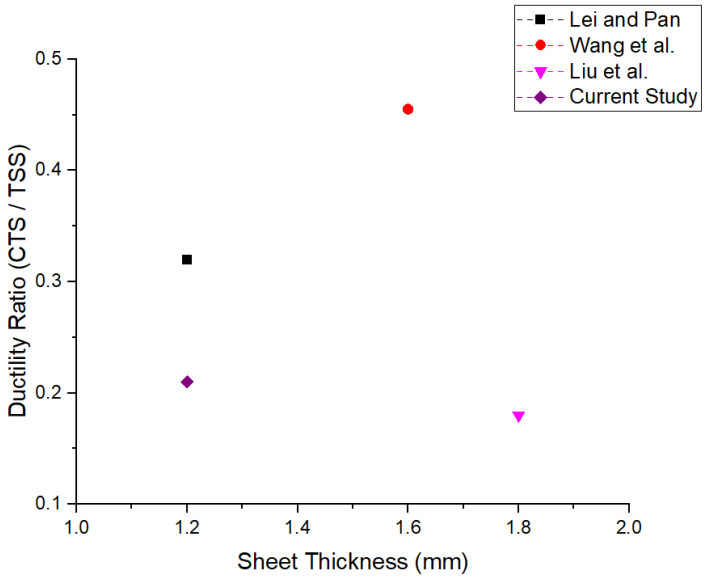


**Figure 4.9: Comparison between ductility ratios reported in the literature for Q&P steels and the current study.**

The weld strength results show a slight decrease in both peak CTS and TSS values for Q&P980. Guidelines described by AWS D8.1M state that for the materials in this study, with a thickness of 1.2 mm, the spot welds should meet a minimum shear strength value of 9.17 kN and a cross tension strength value of 1.87 kN [10]. The values found for both TSS and CTS of the alloys all safely meet these requirements, with DP980 welds exceeding TSS requirements by as much as 90% and the Q&P980 welds exceeding the required minimum TSS by as much as 70%.

The weld strength samples were cross-sectioned to obtain more information on the fracture behavior of the steels. Figure 4.10 shows the cross-section of a CTS sample of DP980, where crack propagation can be seen in the HAZ, and failure occurs around the softened sub-critical HAZ. This agrees with the microhardness results shown previously in Figure 4.6 and with the current understanding of how HAZ softening affects the welds' failure behavior. However, further testing was required in order to analyze the fracture behavior of Q&P980 welds properly.

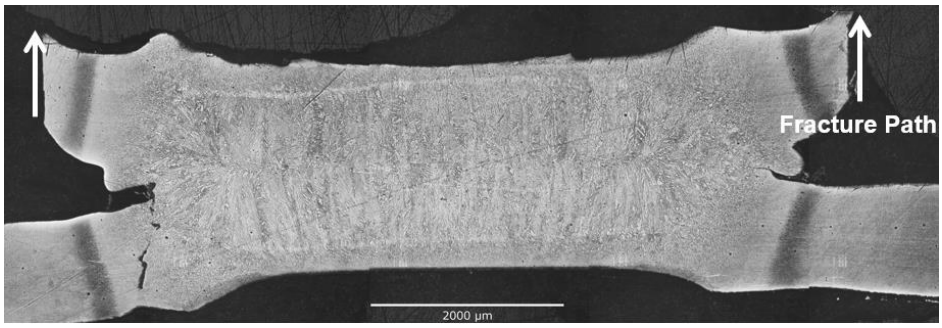


**Figure 4.10: Cross-section of the DP980 weld nugget after CTS test showing the fracture path.**

Analysis of the fracture initiation and fracture behavior in Q&P steels was done by performing interrupted CTS tests to characterize the crack propagation before complete failure, where the test was stopped when the weld reached 90% of its peak strength. Microscopy of the Q&P980 weld nugget surface after the interrupted CTS test shows crack propagation around the weld nugget, as seen in Figure 4.11. It may be seen that the crack's path around the weld nugget is evidence of failure around the fusion zone and not in the heat-affected zone. This conclusion is corroborated by the fact that no softening behavior was observed in the hardness tests, so the crack propagation should not occur around the sub-critical area of the heat-affected zone.

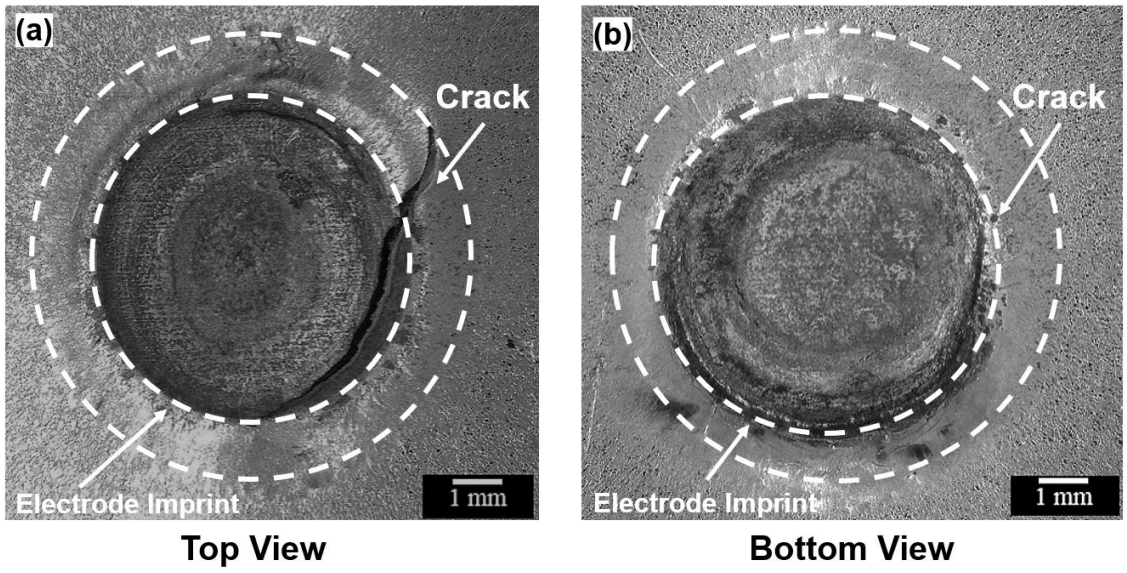


**Figure 4.11: Overview of the weld nugget surface after interrupted CTS test of Q&P980. (a) Top View showing crack propagation around weld nugget (b) Bottom View**

The interrupted samples were cross-sectioned to analyze the crack behavior and confirm the suggested failure path (fracture mechanism), as shown in Figure 4.12. Cross-sections of the welds interrupted before failure showed that these welds' failure occurs around the fusion zone, starting at the notch and strictly following the weld nugget. This behavior is similar to what was previously reported for Q&P980, as Liu et al.'s work [82] presents very similar results for the same material. According to Liu et al., the failure behavior was determined to result from a liquation crack in the fusion zone's vicinity. The study showed that the region close to the liquation crack displayed prominent softening, which was attributed to the fact that alloying elements such as C and Mn were absent in the root of the crack incurring in the formation of martensite with low alloying contents [82]. However, no such liquation cracks were found in the present work.

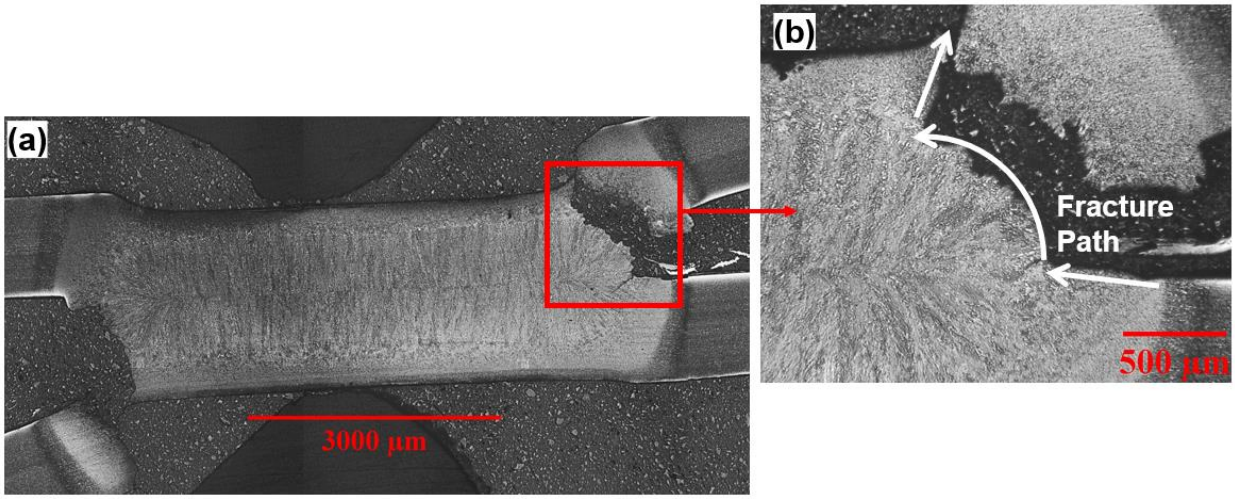


**Figure 4.12: Cross-section of the Q&P980 weld nugget after interrupted CTS test. (a) Image of the cross-section showing the fracture path, (b) High magnification image of the fracture path.**

As discussed in Chapter 2, a similar failure behavior has also been described for Al–Si-coated 22MnB5 and Dual-Phase steels, where failure around the fusion zone was related to the presence of transient softening at the fusion boundary. Section 2.3.3 described how halo's occurrence is related to carbon redistribution at the fusion boundary, which occurs when the molten nugget boundary remains static towards the end of the welding cycle, forming softer carbon-depleted martensite in the adjacency of the fusion boundary [93, 94, 96].

Previous work reported that halo has an average width of approximately 104 µm [96]. This means that that traditional microhardness testing with a spacing of 200 µm is not capable of representing the softening in that region. To determine if a halo was present in the welds produced in this study, an altered

microhardness test was performed with a spacing of 80 μm and a force of 200 g, where the spacing still respected the requirement of being three times larger than the average diameter of the indentation, as described in ASTM E384 [109]. These microhardness test results are shown in Figure 4.13, which shows softening around the fusion zone, where a decrease in hardness of around 10% was measured. This hardness drop offers evidence of the presence of the halo in these welds.

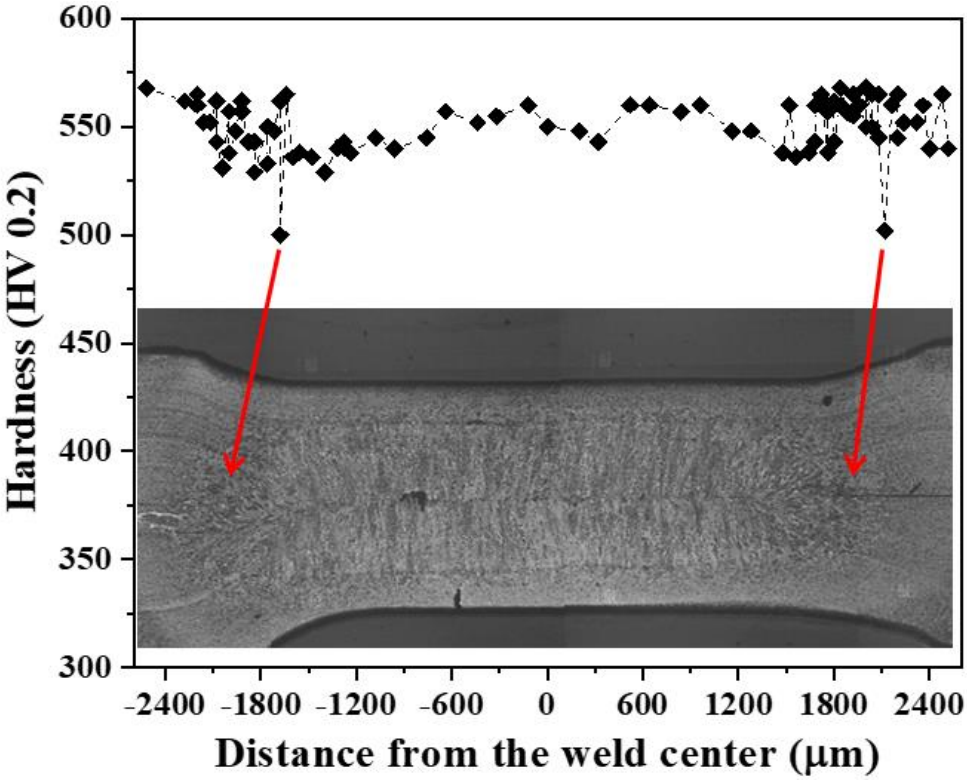


**Figure 4.13: Hardness around the nugget of a Q&P980 weld showing a decrease in hardness around the fusion zone.**

As Mohamadizadeh et al. [94] reported for the resistance spot welding of 22MnB5, the weld's failure under tensile and shear loading initiated and propagated along the fusion boundary, where the halo was located, even though it was not the minimum hardness in the joint. Similarly, for the material described in the present study, the softened region's presence is likely what leads to the failure around the fusion zone, as it affects the energy absorption of the welded joints and possibly leads to lower CTS results. Further investigation is required to confirm this correlation and determine if controlling the halo can increase joint strength.

## 4.5 Summary and Further Work

This study contributed to the existing knowledge of the resistance spot welding behavior of Q&P steels by analyzing their microstructure, hardness profile, tensile shear strength, cross tension strength, and failure behavior. It found that the cross tension and tensile shear test samples all failed in a partial or full button pull-out mode, with an acceptable ductility ratio, but with lower cross tension strength compared to the available studies on resistance spot welding of Q&P steels. Fractography of the testing samples showed that the crack propagated along the fusion boundary, an occurrence previously reported in the literature for Q&P980, but with no comprehensive explanation regarding the mechanism behind the behavior.

This work proposed that this fracture occurred due to the formation of a softened region at the fusion boundary. This phenomenon is commonly known as the halo ring and has been studied in Al–Si-coated 22MnB5 but has not yet been reported for Q&P steels. The possible influence of this softened region on the mechanical performance of the welds was described. However, further study is required to confirm the correlation between the transient softening and the lower CTS values observed. Further work should also be done to determine how to control the halo and if doing so, in fact, increases CTS results.

# Chapter 5
# Optimization of Weld Performance by Varying Weld Schedules

The previous chapter showed that Q&P steels had a lower ductility ratio and cross-tension strength than those reported in the available literature, and the presence of a softened region around the fusion zone was possibly related to the lower CTS values observed. This chapter explores the use of multi-pulse weld schedules to optimize Q&P980's weldability and to control the halo's occurrence.

Q&P980 was the single focus of this study, and the results found in Chapter 4 under a single pulse weld schedule were used to understand how the multi-pulse schedule affects the microstructural and mechanical behaviors of the weld. Design of experiment (DOE) was used to determine the influence of various process parameters on weld diameter, hardness, and strength; and to optimize these parameters for enhanced weld performance. A weld schedule where the weldability of Q&P is optimized by maximizing the weld's strength was established. The study also investigated the use of these varied process parameters to eliminate the halo's occurrence by driving nugget growth into the carbon-depleted region at the fusion boundary. The implementation of this method and its results are discussed in the following sections.

## 5.1 Experimental Design and Analysis

Despite the wide use of multi-pulse weld schedules to improve the weldability of AHSS, there has only been a single study in the literature investigating the effect of multi-pulsing in the RSW of Q&P steels. The work of Liu et al. [82] compared the use of a single pulse to a double pulse with varying currents, finding that a higher secondary current improved both tensile shear and cross-tension strength. However, it is not clear from the study if this occurs due to microstructural changes in the weld or if it is solely related to an increase in the nugget's diameter due to a second pulse. The secondary current is the single process parameter changed in the study, so changing other parameters such as cooling time between pulses or second pulse length has never been discussed in the welding of Q&P steels.

This study conducted experimental trials based on the design of experiment (DOE) by varying process parameters such as second pulse current, second pulse length, and cooling time between pulses, as shown in Table 5.1.

**Table 5.1: Design of experiment process parameters.**

| Factor | Name | Low Value | High Value |
|---|---|---|---|
| A | Cooling Time Between Pulses | 2 cycles | 4 cycles |
| B | Second Pulse Length | 4 cycles | 8 cycles |
| C | Second Pulse Current | 6 kA | 9 kA |

A factorial model of the design of experiment was adopted to arrive at the experimental trials with varying parameter levels. A 2-level full-factorial design was developed using Minitab® Version 19.2020.1 (Minitab, 2020) to study the effects of the three chosen factors on nugget diameter, fusion zone hardness, tensile-shear strength, and cross-tension strength. The values of input process parameters used and the run order of the spot-welding experiments conducted are listed in Table 5.2. This thesis references each sample using the format A-B-C based on the factors described in Table 5.1, where A is the cooling time between pulses in cycles, B is the second pulse length in cycles, and C is the second pulse current in kA.

**Table 5.2: Design Matrix.**

| Run Order | Sample Reference | Cooling Time (cycles) | 2nd Pulse Time (cycles) | 2nd Pulse Current (kA) |
|---|---|---|---|---|
| 1 | 4-4-6 | 4 | 4 | 6 |
| 2 | 4-8-6 | 4 | 8 | 6 |
| 3 | 2-8-6 | 2 | 8 | 6 |
| 4 | 2-4-6 | 2 | 4 | 6 |
| 5 | 2-8-9 | 2 | 8 | 9 |
| 6 | 4-4-9 | 4 | 4 | 9 |
| 7 | 4-8-9 | 4 | 8 | 9 |
| 8 | 2-4-9 | 2 | 4 | 9 |

Minitab® was used to analyze the factorial design, which was done through analysis of variance (ANOVA) and linear regression, as well as for plotting the fitted means to understand how the factors affected the responses and how the variables interact. The complete statistical analysis performed with

Minitab can be found in Appendix A. Variables were found significant if their p-values were less than the significance level of 0.05.

## 5.2 Effect on Nugget Diameter and Fusion Zone Hardness

The Pareto plot of the main effects for nugget diameter, presented in Figure 5.1 (a), shows that the most significant effect is the second pulse time (B), followed by the second pulse current (C). A summary of the model can be found in Appendix A, where the $R^2$ value was 99.74%, which indicates that the model fits the data extremely well. Figure 5.1 (b) shows the main effects plot for diameter. It can be seen that while cooling time has little effect on the nugget diameter, a higher second pulse time leads to a larger nugget, and although not as significant, so does a higher second pulse current. As both current and time are main factors indicating the heat generated during the RSW process (see equation 2.2), these effects are expected.

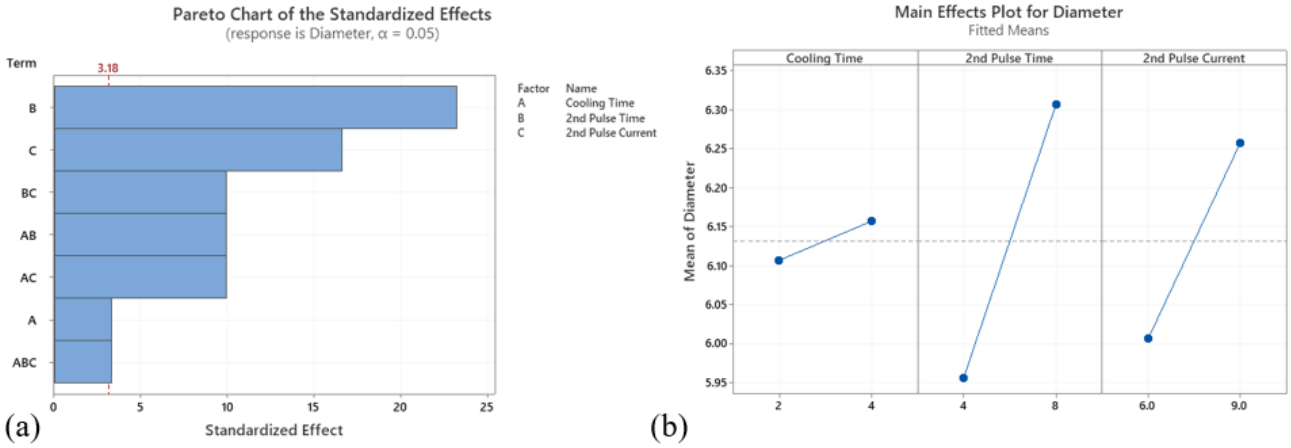


**Figure 5.1: (a) Pareto plot of the main effects for nugget diameter and (b) Main effects plot for nugget diameter.**

In this part of the study, the reported fusion zone hardness values specifically refer to the lowest hardness values found in the fusion zone as a means to characterize the occurrence of softening at the fusion boundary. These results are of particular importance to the study, as they not only identify which samples were affected by the halo but also which variables affect its formation. The Pareto plot of the main effects for fusion zone hardness, found in Figure 5.2 (a), shows that the only significant factor ($\alpha$=0.05) is the second pulse current (C).

Figure 5.2 (b) shows the main effects plot for the minimum fusion zone hardness, where it can be seen that pronounced softening at the fusion boundary is highly related to a decrease in second pulse current.

These results show that not only fusion zone softening occurs when a single pulse is used, using a multi-pulse schedule with a lower current in the secondary pulse also consistently leads to the formation of the halo, indicating that there is a minimum second pulse current required to eliminate the occurrence of the halo.

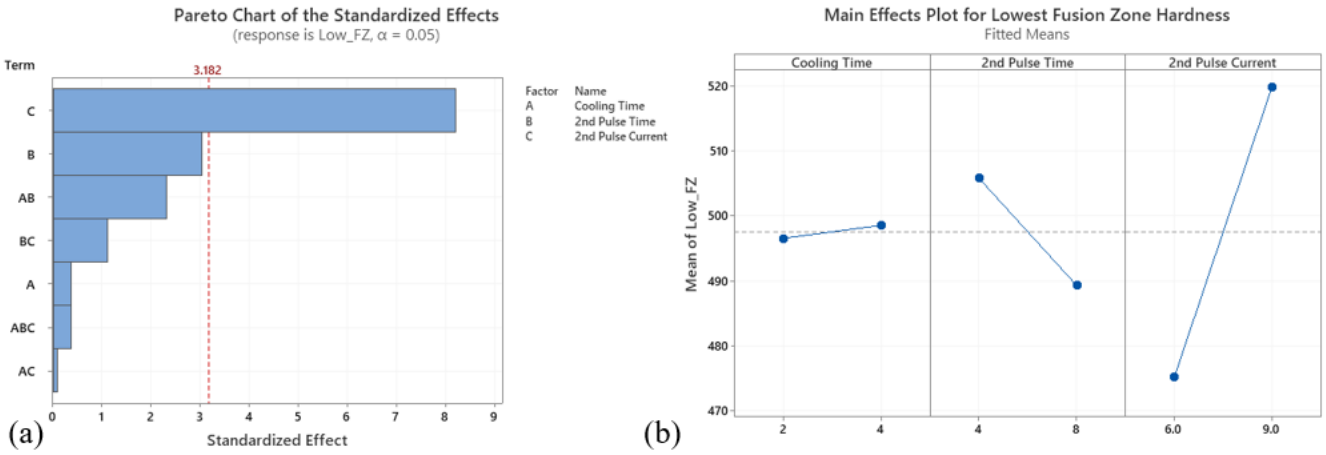


**Figure 5.2: (a) Pareto plot of the main effects for lowest fusion zone hardness and (b) Main effects plot for lowest fusion zone hardness.**

## 5.3 Microstructural Characterization and Hardness

The microstructures of the weld zone were characterized by optical microscopy. All spot welds in this study showed no apparent defects, with no evidence of shrinkage voids or occurrence of expulsion. The welds showed distinct separation between the base material, HAZ, and FZ typically seen in welds of AHSS. The fusion zone of all welds showed columnar growth where the grains were oriented along the direction of the heat flow, which again is typical for AHSS joints.

Figure 5.3 shows the cross-section and the microstructure for samples 4-4-6 and 4-8-6, where a low secondary current was used, and prominent softening around the fusion boundary was observed in the initial hardness investigation. The welds where the second pulse current was 6 kA showed no evidence of nugget growth during the second pulse, indicating that the nugget was only formed due to melting from the first pulse.

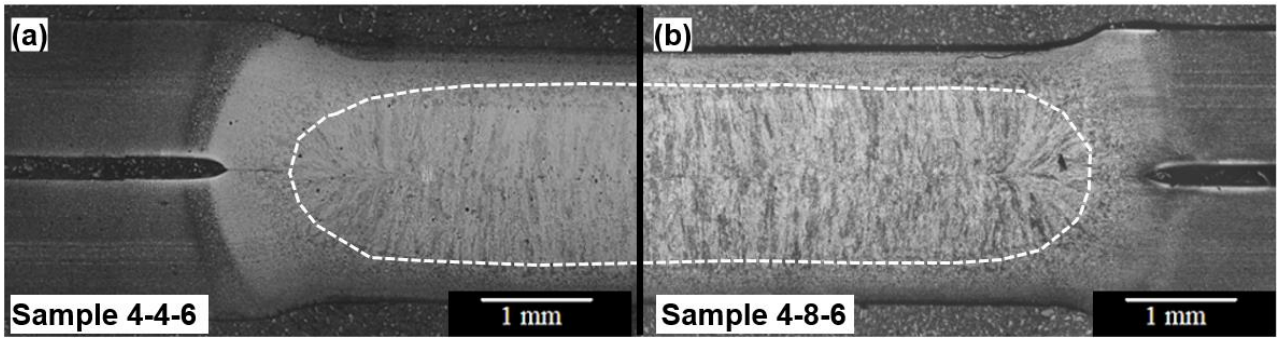


**Figure 5.3: Microstructure for multi-pulse welds (a) sample 4-4-6 and (b) sample 4-8-6.**

Figure 5.4 shows the cross-section and the microstructure for samples 4-4-9 and 4-8-9, where a high current was used in the second pulse, and no apparent evidence of the halo was observed in the initial hardness investigation. Similar to what was described by Liu et al. [82], two distinct nuggets can be seen in Figure 5.4, one formed with the primary weld current and another formed by the heat generated by the secondary weld current, which remelts the primary nugget. The same is not observed in Figure 5.3, possibly because the second pulse's low current was not enough to not remelt the primary nugget.

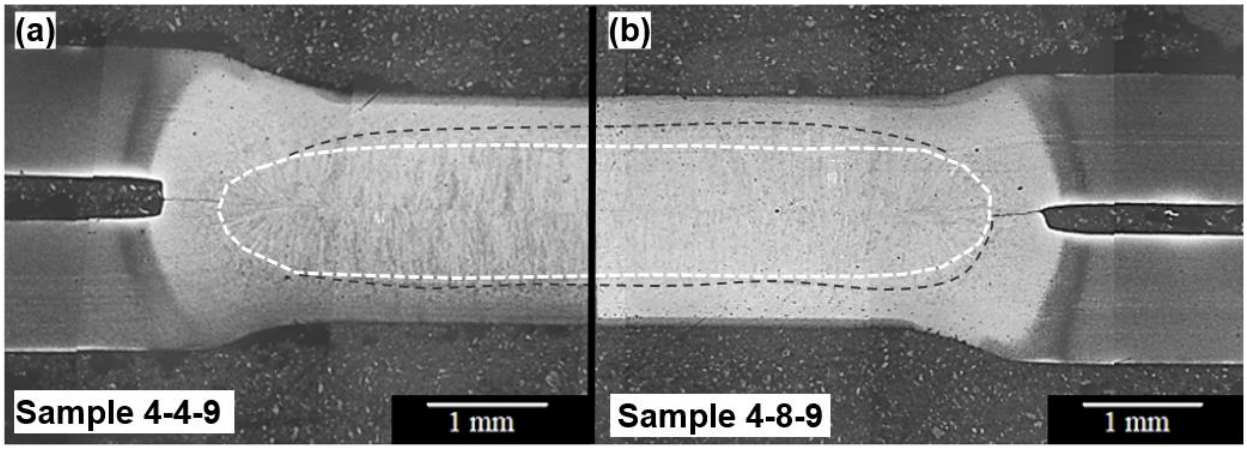


**Figure 5.4: Microstructure for multi-pulse welds (a) sample 4-4-9 and (b) sample 4-8-9.**

A similar microhardness test to the one described in Chapter 4 was used to determine the halo's presence, where the test was performed with a spacing of 80 μm and a force of 200 g, the spacing respected the requirement of being three times larger than the average diameter of the indentation, as described in ASTM E384 [109]. These results are shown in Figure 5.5. Prominent softening around the fusion zone is seen in Figure 5.5 (a), where a decrease in hardness of as much as 15% was measured, providing evidence of the

halo's presence in the welds where a low secondary current was used. As discussed earlier, softening is not seen on the welds where a high secondary current was used, as shown in Figure 5.5 (b).

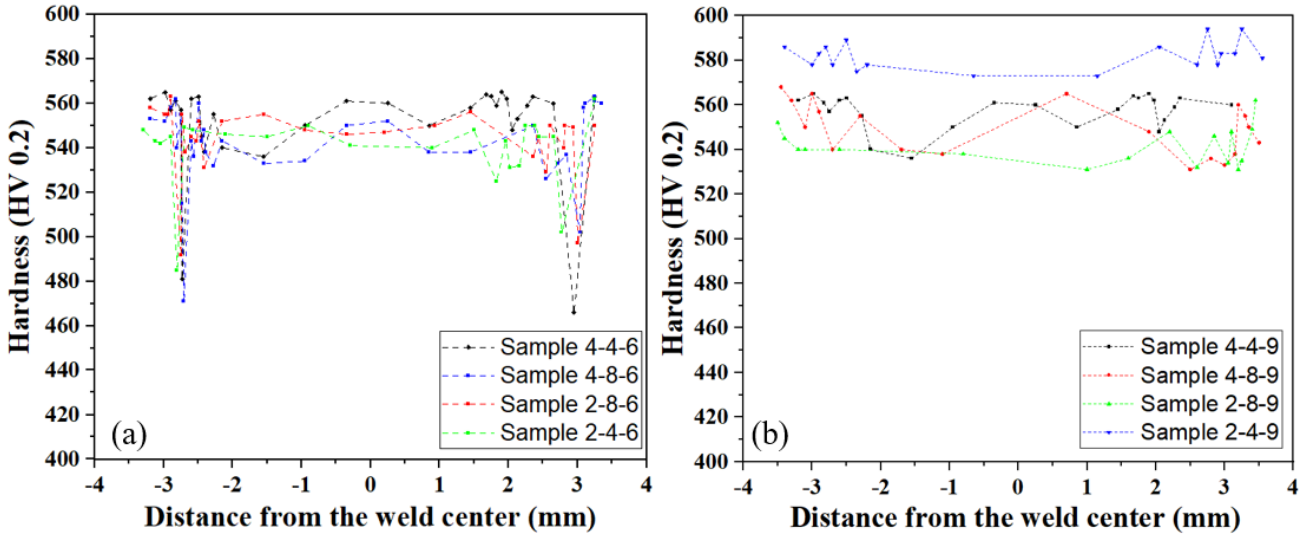


**Figure 5.5: Hardness across the fusion zone for multi-pulse Q&P980 welds with (a) low secondary current and (b) high secondary current.**

To further investigate the presence of halo in Q&P980 welds, hardness mapping was carried out with a low indenter load and a small distance between the indentations, similar to the test described by Sherepenko et al. [93]. The load applied was 50g (HV 0.05), and the spacing corresponded to three times the average diameter of the indentation, again following the requirement described by ASTM E384 [109]. 112 indents were made following a checkerboard pattern, where the minimum spacing between the indentations was 45 μm. To reduce the testing time, only a small region of each weld cross-section was investigated, as shown in Figure 5.6 (a), Figure 5.7 (a), Figure 5.8 (a), and Figure 5.9 (a).

The hardness mapping of the samples that showed evidence of the halo is shown in Figures 5.6 and 5.7, where the hardness profiles extracted from the maps were computed and drawn using Delaunay Triangulation in OriginPro. In these images, the microstructure highlighted in the detail is reflected in the harness mapping, which reveals a softened region at the fusion boundary. This softened region's outline corresponds to the halo. For sample 2-8-6 (Figure 5.6), while the highest hardness measured was 630 HV, the hardness in the region corresponding to the halo was as low as 460 HV, showing a decrease in hardness of as much as 27%. For sample 4-8-6 (Figure 5.7), the decrease in hardness was approximately 14%, going from the maximum value of 600 HV to the lowest of 520 HV. Due to the significantly low load applied and corresponding small indentation, a skew in the measured hardness values is expected. This

phenomenon, known as indentation size effect (ISE), has been amply discussed in the literature. It is well established that a combination of different mechanisms and instrumental errors contributes to the variation in hardness value from a variation in indentation size. This effect is usually related to a decrease in the apparent microhardness with an increase in applied test load or an increase in microhardness with a decrease in test load [110, 111]. This accounts, for example, for divergences seen between the results reported in Figure 5.5 (a), where the highest hardness value measured with a load of 200g was 570 HV, and the results reported in Figures 5.6 and 5.7, where the highest hardness value measured with a load of 50g was 630 HV, all while dealing with the same set of samples.

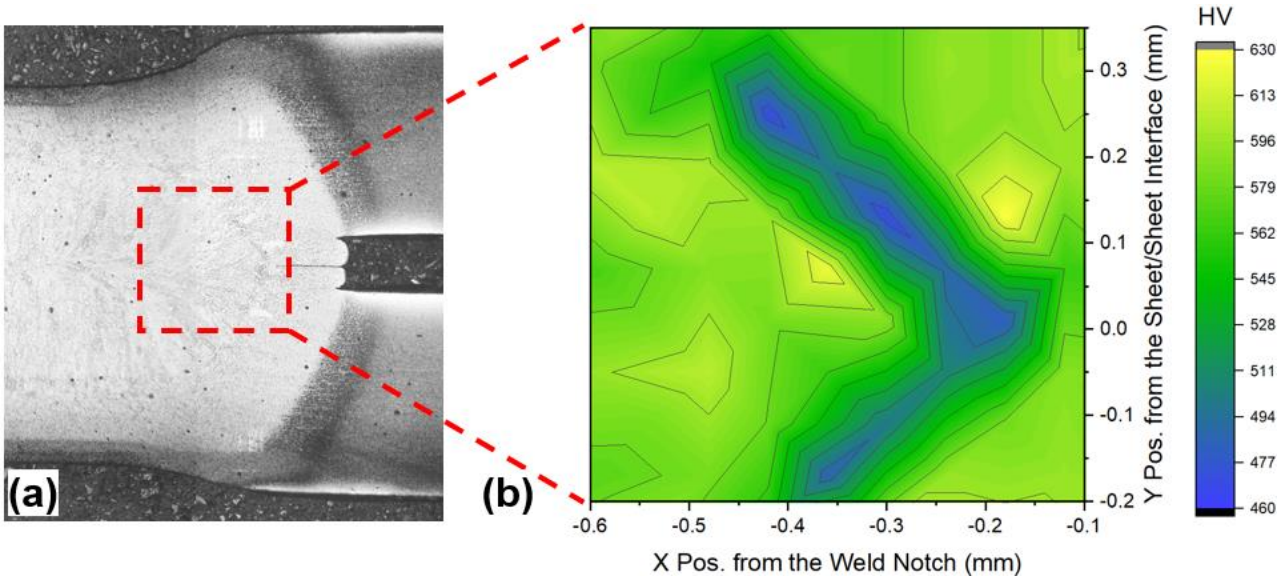


**Figure 5.6: (a) Detail of sample 2-8-6 and (b) Microhardness map.**

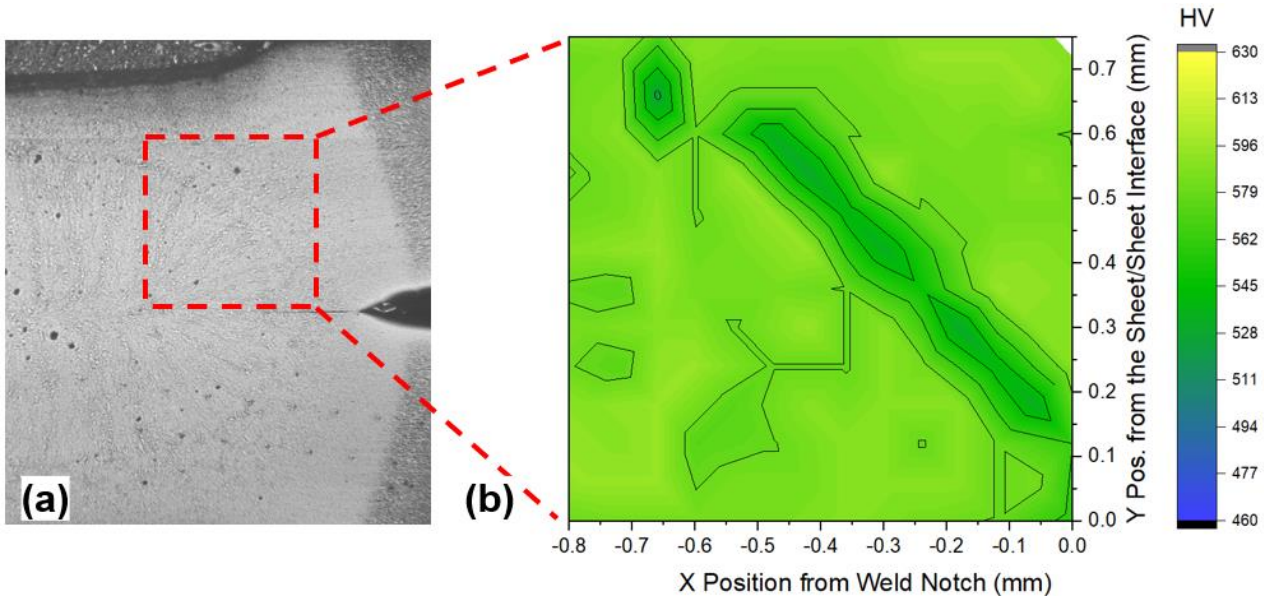


**Figure 5.7: (a) Detail of sample 4-8-6 and (b) Microhardness map.**

Hardness mapping of the samples welded with high second pulse current was also performed and is shown in Figures 5.8 and 5.9. For sample 2-8-9 (Figure 5.8), while the highest hardness measured was 605 HV, the lowest hardness value measure was 540 HV, showing a decrease in hardness of approximately 11%. For sample 4-8-9 (Figure 5.9), the decrease in hardness was also around 11%, going from the maximum value of 600 HV to the lowest of 530 HV. It can be seen in these images that the halo outline present in the detail shows no correspondence to the hardness mapping. Contrary to what was seen in Figures 5.6 and 5.7, there is no distinct low hardness area located at the fusion boundary, and the hardness distribution is random. The lowest hardness values are still higher than those seen in samples with evidence of the halo, and the decrease in hardness from the highest value to the lowest value is less pronounced.

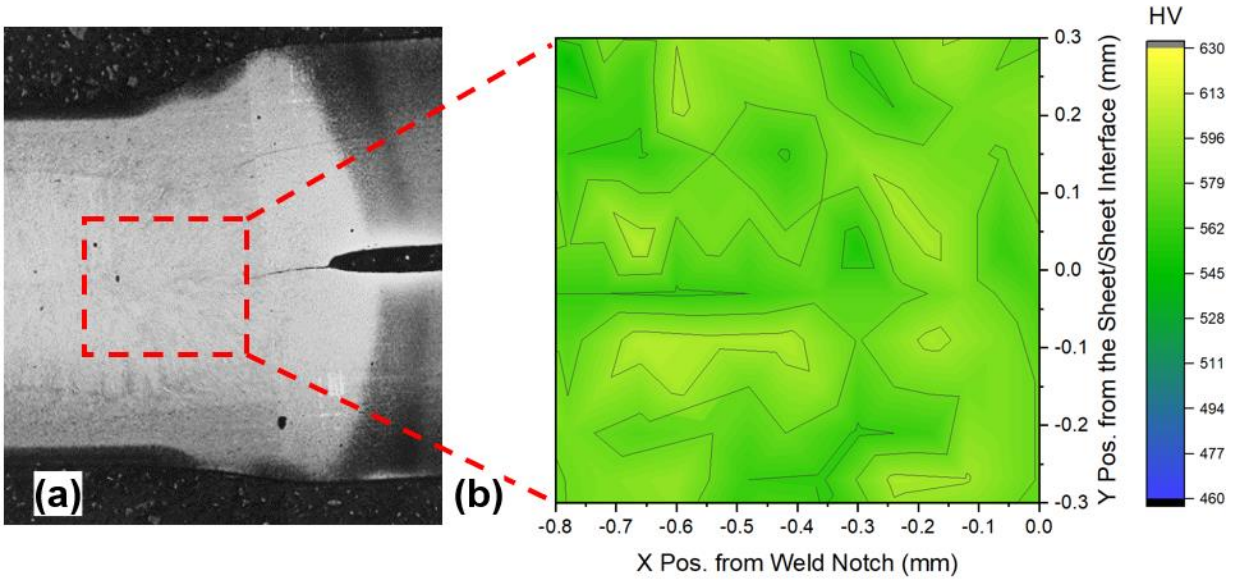


**Figure 5.8: (a) Detail of sample 2-8-9 and (b) Microhardness map.**

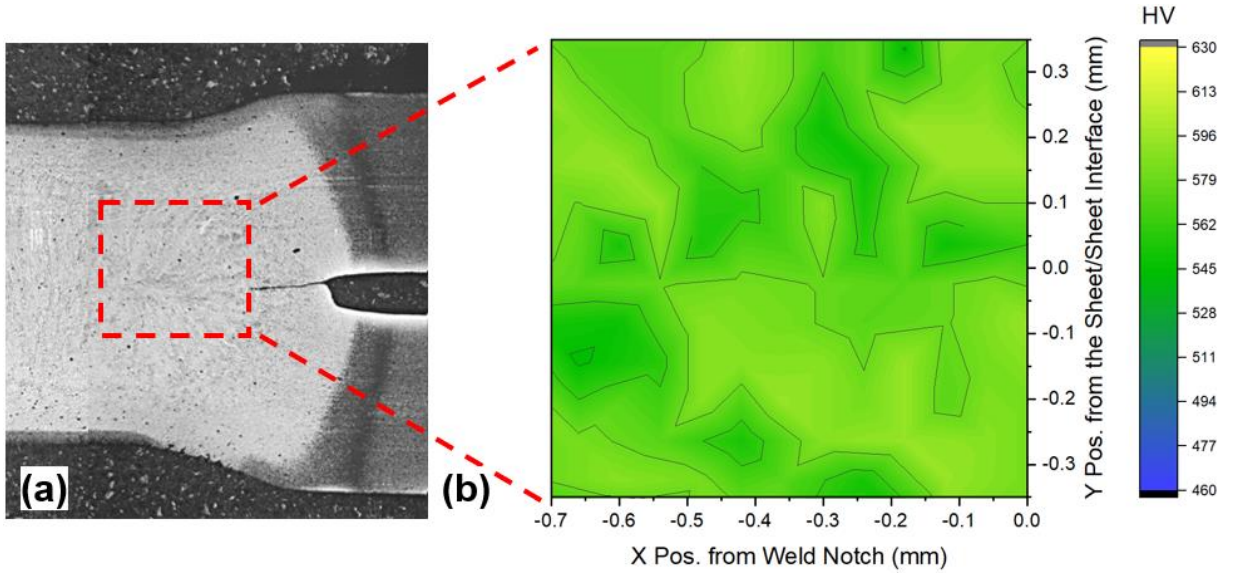


**Figure 5.9: (a) Detail of sample 4-8-9 and (b) Microhardness map.**

## 5.4 Effect on Weld Strength and Failure Mode

The same normalization method described by Dancette et al. [60] and discussed in Chapter 2 was used to decouple the effect of different weld diameters when investigating how the various factors affect the weld strength responses. Normalized CTS and TSS values were used in the ANOVA and linear regression and are shown in the main effects plots described in this section and in the results found in Appendix A.

The Pareto plot of the effects for normalized TSS, presented in Figure 5.10 (a), shows that the significant factors (α=0.05) are the second pulse time (B), the interaction between second pulse time and second pulse current (BC), and the interaction between all factors (ABC). A summary of the model can be found in Appendix A, where the $R^2$ value was 97.57%, which indicates that the model fits the data well. Figure 5.10 (b) shows the main effects plot for normalized TSS. It can be seen that the second pulse time is the most significant individual factor, where the longer the pulse, the higher the TSS values. As the interaction between all factors is the most significant effect, the highest TSS occurs with a short cooling time between pulses, long second pulse length, and high second pulse current.

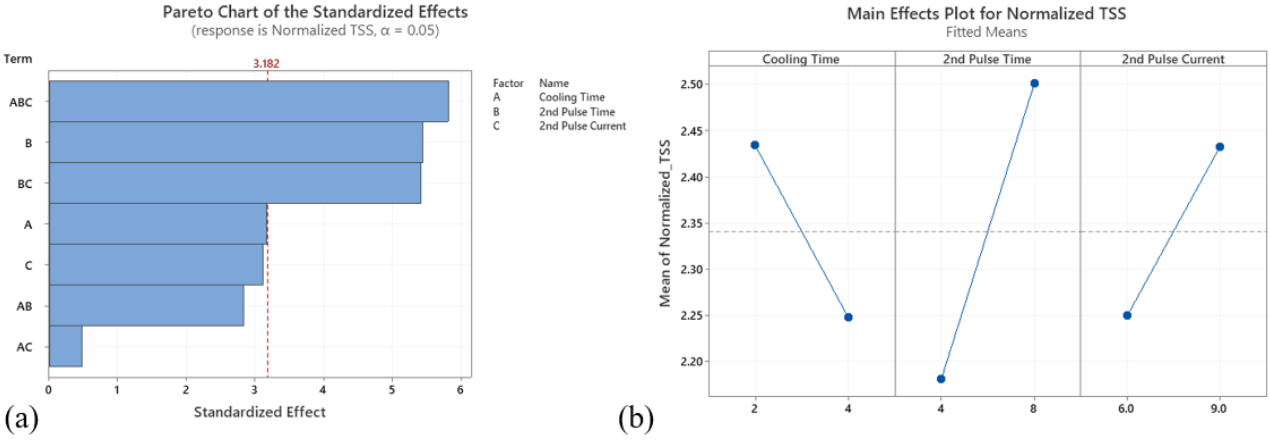


**Figure 5.10: (a) Pareto plot of the main effects for normalized TSS and (b) Main effects plot for normalized TSS.**

The Pareto plot of the effects for normalized CTS, presented in Figure 5.11 (a), shows that most factors and the interaction between them are significant, except cooling time (A). The most significant factor is, by far, the secondary pulse current (C). The $R^2$ value was 99.93%, which indicates that the model fits the data extremely well. Figure 5.11 (b) shows the main effects plot for normalized CTS. It can be seen that while cooling time and second pulse time have little effect on CTS, a higher second pulse current leads to a higher CTS value. This same effect is seen in Figure 5.2 (b), which shows the main effects plot for the lowest hardness in the fusion zone. A high secondary current was also related to higher minimum FZ hardness and no halo occurrence.

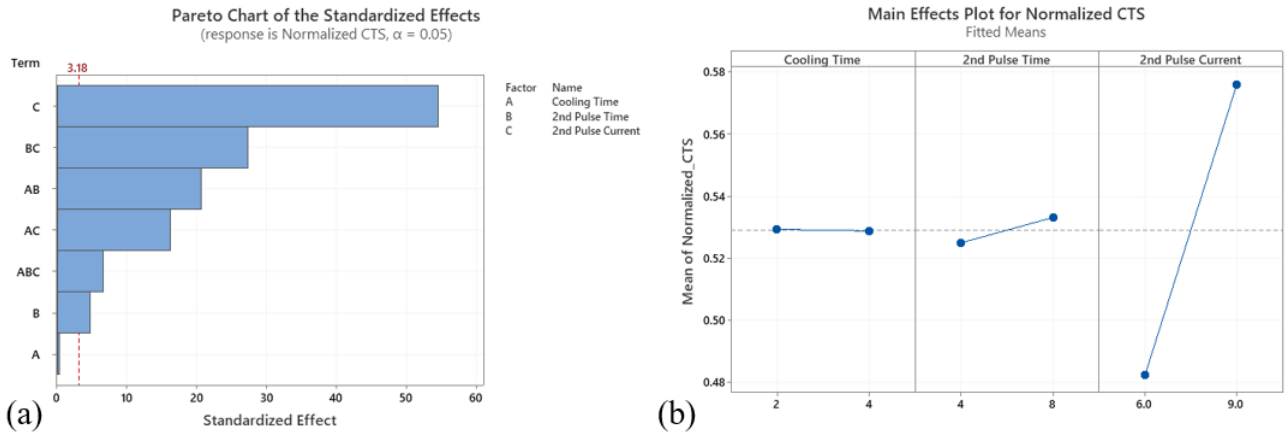


**Figure 5.11: (a) Pareto plot of the main effects for normalized CTS and (b) Main effects plot for normalized CTS.**

The experimental generated power curve and the dynamic resistance curve were extracted for each of the weld schedules to calculate the samples' total heat input, shown in Figure 5.12. The total heat input was used to correlate and unify the varying values of cooling time, second pulse time, and second pulse current of the different samples in this study to a single measurable value for ease of representation in the following weld strength graphs. As expected, the two samples with a low secondary current and low second pulse time had the lowest total heat inputs, around 2.5 kJ, while the two samples with a high secondary current and high second pulse time had the highest heat inputs, around 3.7 kJ.

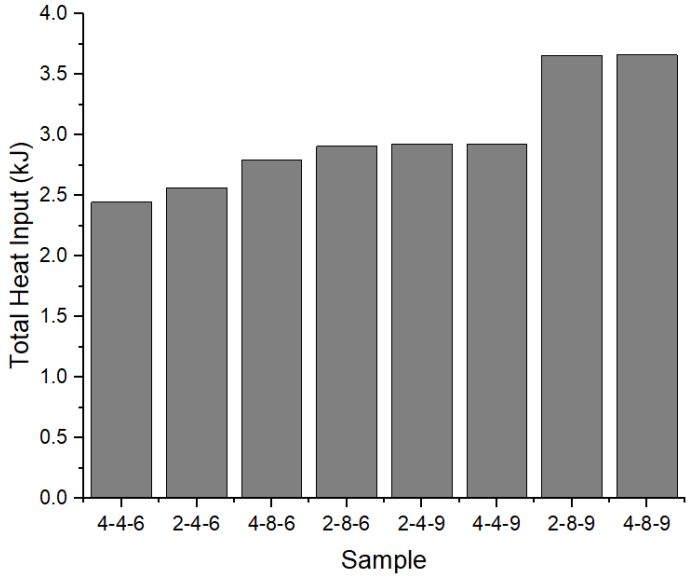


**Figure 5.12: Total heat input for multi-pulse weld samples.**

Figure 5.13 shows the tensile shear strength results for samples with and without the halo, plotted against the total heat input. The reported grey line in Figure 5.13 represents the average TSS value for samples with the halo. The TSS results show that the statistical difference across samples with halo is not significant, as the slope is not different from zero. Samples with no halo appear to have higher TSS values, with an increase in heat input for these samples leading to an increase in TSS. A two-sample t-test was run using Minitab® to verify whether the average difference for TSS samples with and without halo is significant, and the results can be found in Appendix A. The results show no significant TSS difference between samples with halo (15.95 ± 2.05) and samples with no halo (18.2 ± 3.87), where the p-value was found to be 0.095. As seen in Figure 2.11, the force applied during tensile shear strength testing is perpendicular to the location of the halo, which explains why this softened region would not affect the load-bearing capacity of the welds under TSS. Although there seems to be no impact of the halo in the TSS of Q&P980, multi-pulsing effectively increased TSS results from a maximum of 15.6 kN for single pulse welds to a new maximum of 22 kN, improving the steel's weldability.

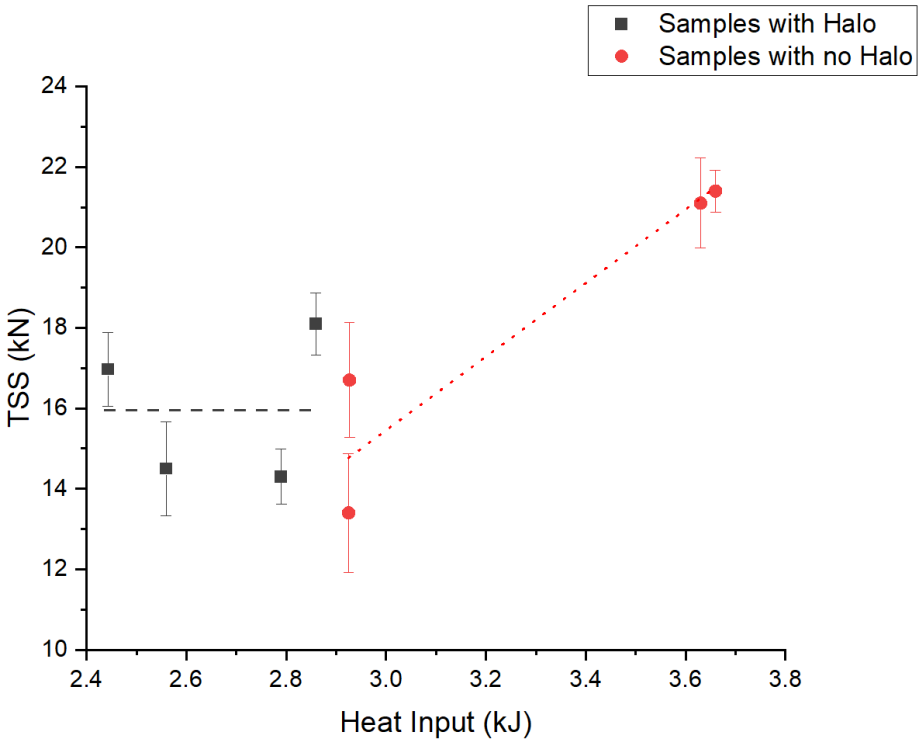


**Figure 5.13: Tensile-shear strength for multi-pulse weld samples.**

Figure 5.14 shows the cross-tension strength results for samples with and without the halo, plotted against the total heat input. The results show that while an increase in heat input leads to an increase in CTS for the

samples with halo, the statistical difference across samples without the halo is not significant, and the reported red line in Figure 5.14 represents the average CTS value for samples with no halo.

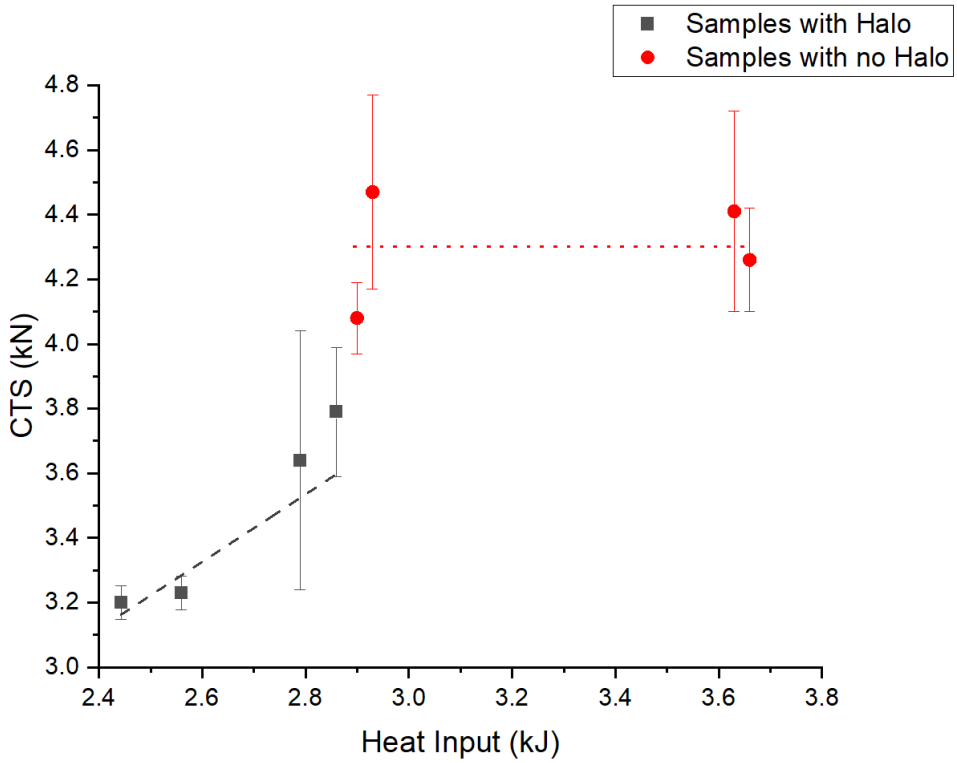


**Figure 5.14: Cross-tension strength for multi-pulse weld samples.**

Samples with no halo appear to have consistently higher CTS values, further illustrating what was discussed before regarding the main effects plot for the lowest fusion zone hardness and normalized CTS (Figures 5.2 and 5.11). Samples where a high secondary current was used show no evidence of the halo and display higher CTS values than samples with the halo. Again, a two-sample t-test was run to verify whether the average difference for CTS samples with and without halo is significant. The results show that samples with no halo have statistically significantly higher CTS values (4.07 ± 0.61) than samples with halo (3.38 ± 0.29), where the p-value was found to be 0.003. The concepts discussed in Chapter 4 are possibly true, where the correlation between the presence of a transient softening and the lower CTS was confirmed, and controlling the halo does increase CTS results. As discussed before, the same, however, was not seen in TSS.

Figure 5.15 shows the weld strength results for multi-pulse Q&P980 plotted against the total heat input and the ductility ratio represented by the peak CTS values divided by the peak TSS values. Overall, an increase in total heat input led to an increase in both CTS and TSS values. Values as high as 22 kN were

found for the TSS tests of multi-pulse Q&P980 welds, and CTS testing showed results as high as 4.7 kN. The ductility ratio (CTS / TSS) ranges from around 0.19 to 0.31.

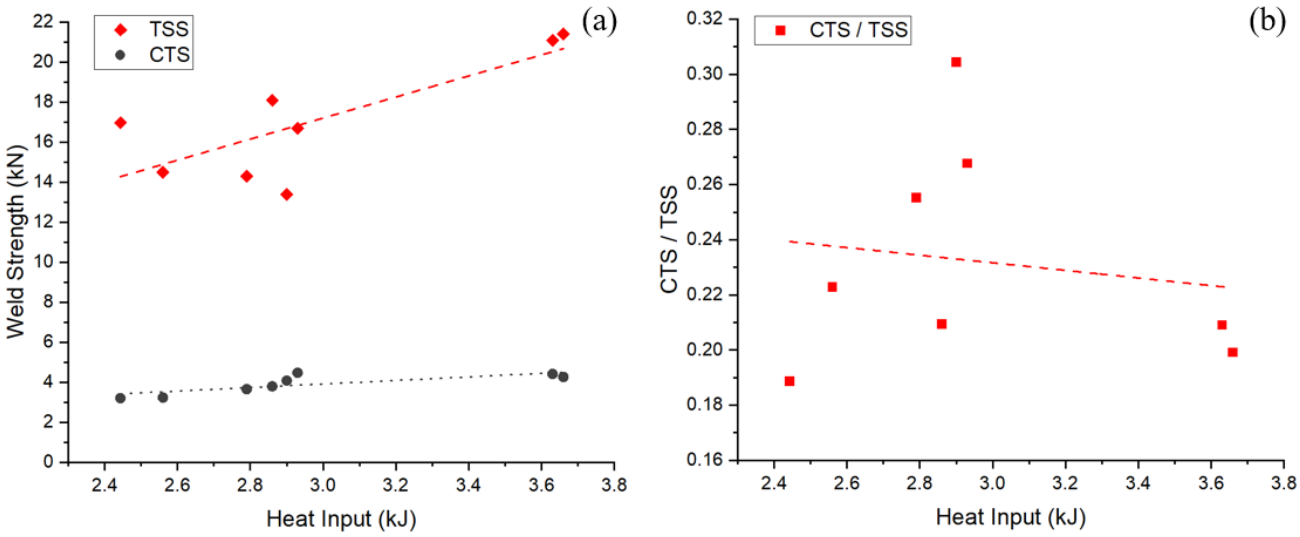


**Figure 5.15: (a) Weld strength for multi-pulse Q&P980 (b) Ductility ratio for multi-pulse Q&P980.**

As described in Chapter 4, the TSS values for single pulse Q&P980 welds achieved values as high as 15.6 kN, and CTS values were as high as 3.2 kN. The ductility ratio for single pulse Q&P980 ranged from 0.20 to 0.21. Therefore, the use of multi-pulse weld schedules improved the TSS values of Q&P welds by as much as 41%, the CTS values by as much as 47%, and the ductility ratio by 48%. As discussed previously, guidelines described by AWS D8.1M state that for the materials in this study, the spot welds should meet a minimum shear strength value of 9.17 kN and a cross tension strength value of 1.87 kN [10]. The new values found for both TSS and CTS using multi-pulse weld schedules exceed the TSS requirements by as much as 140% and the CTS requirements by as much as 151%.

Figure 5.16 describes how these current results compare to the ones previously reported in the literature, as discussed in Chapter 2 and Figure 2.13, providing an overview of the normalized TSS and CTS values for Q&P980 found in this study and the values reported by Wang and Speer [1], Wang et al. [78], Lei and Pan [79], and Liu et al. [80].

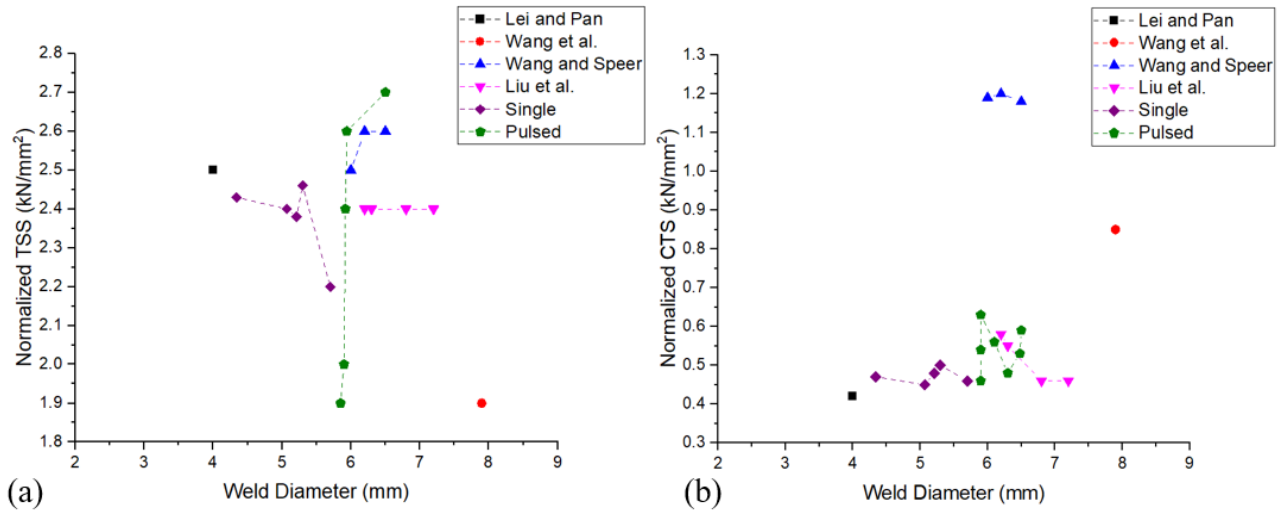


**Figure 5.16: Comparison between strength values reported in the literature for Q&P steels and the current study, showing (a) TSS values and (b) CTS values.**

It can be seen in Figure 5.16 (a) that while the TSS values found for single pulse weld schedules were comparable to the ones previously reported in the literature, multi-pulsing achieves normalized TSS values higher than the ones reported before for Q&P980, with the best results seen in the literature. Figure 5.16 (b) shows that multi-pulse CTS values also showed significant improvement to the ones reported for a single pulse, with CTS values being comparable to those described by Liu et al. [82].

Analysis of the fracture initiation and fracture behavior in multi-pulse welding of Q&P steels was done by performing interrupted TSS and CTS tests to characterize the crack propagation before complete failure, where the test was stopped when the weld reached 90% of its peak strength. Figure 5.17 shows the weld nuggets' microscopy after interrupted testing for the samples welded with a low secondary current.

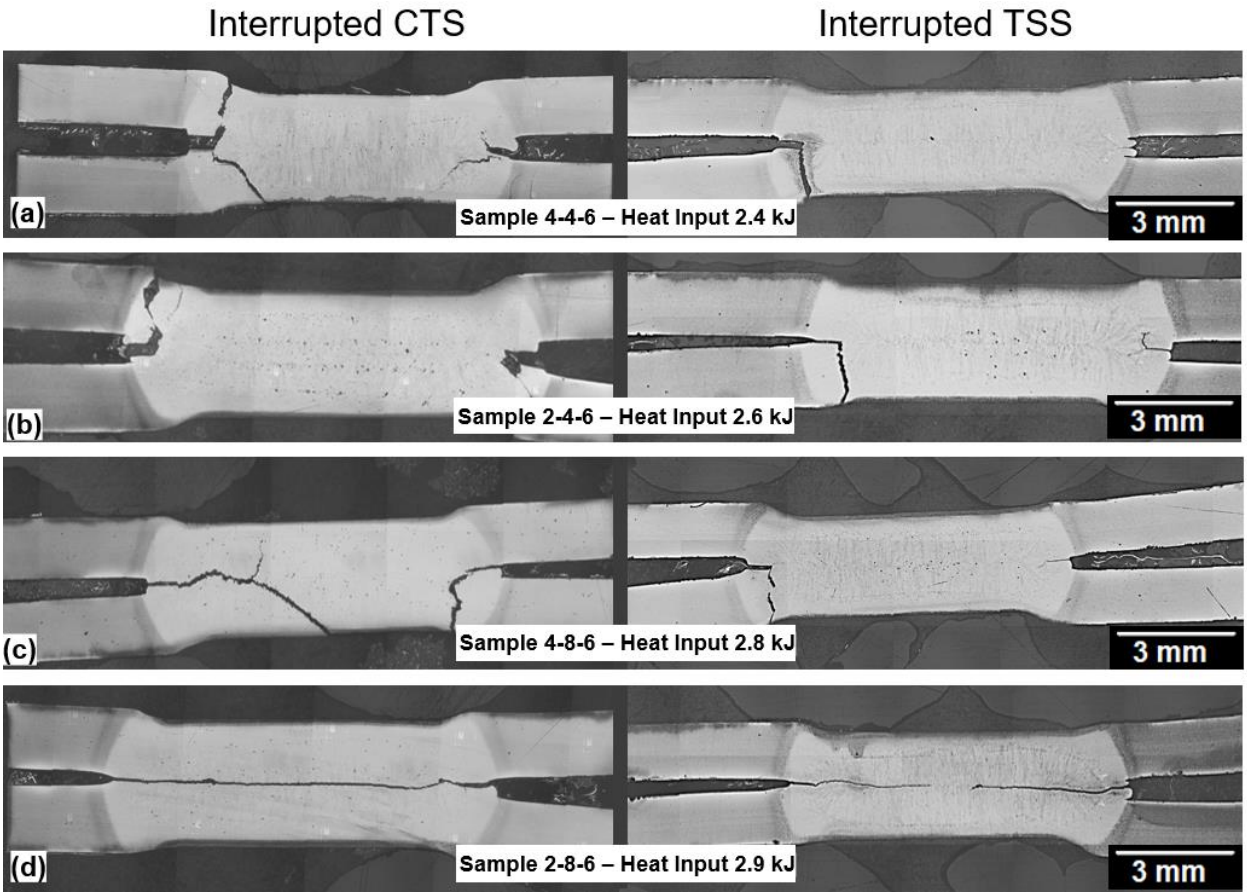


**Figure 5.17: Failure mode comparison for samples with halo, left column showing interrupted CTS and right column showing interrupted TSS (a) sample 4-4-6, (b) sample 2-4-6, (c) sample 4-8-6, and (d) sample 2-8-6.**

While the results in Chapter 4, Figure 4.12 for the single pulse welding of Q&P980 showed evidence of failure around the fusion zone, with crack propagation starting at the notch and strictly following the weld nugget, the same is not consistently observed in the samples shown in Figure 5.17. Sample 2-8-6, shown in Figure 5.17 (d), shows interfacial failure for both interrupted CTS and TSS tests, and the other samples show different variations of crack propagation starting at the notch and propagating through the sheet thickness across the HAZ and FZ, with no discernable pattern. Similar behavior is seen in Figure 5.18, which shows the weld nuggets' microscopy after interrupted testing for the samples welded with a high secondary current, which showed no evidence of the halo.

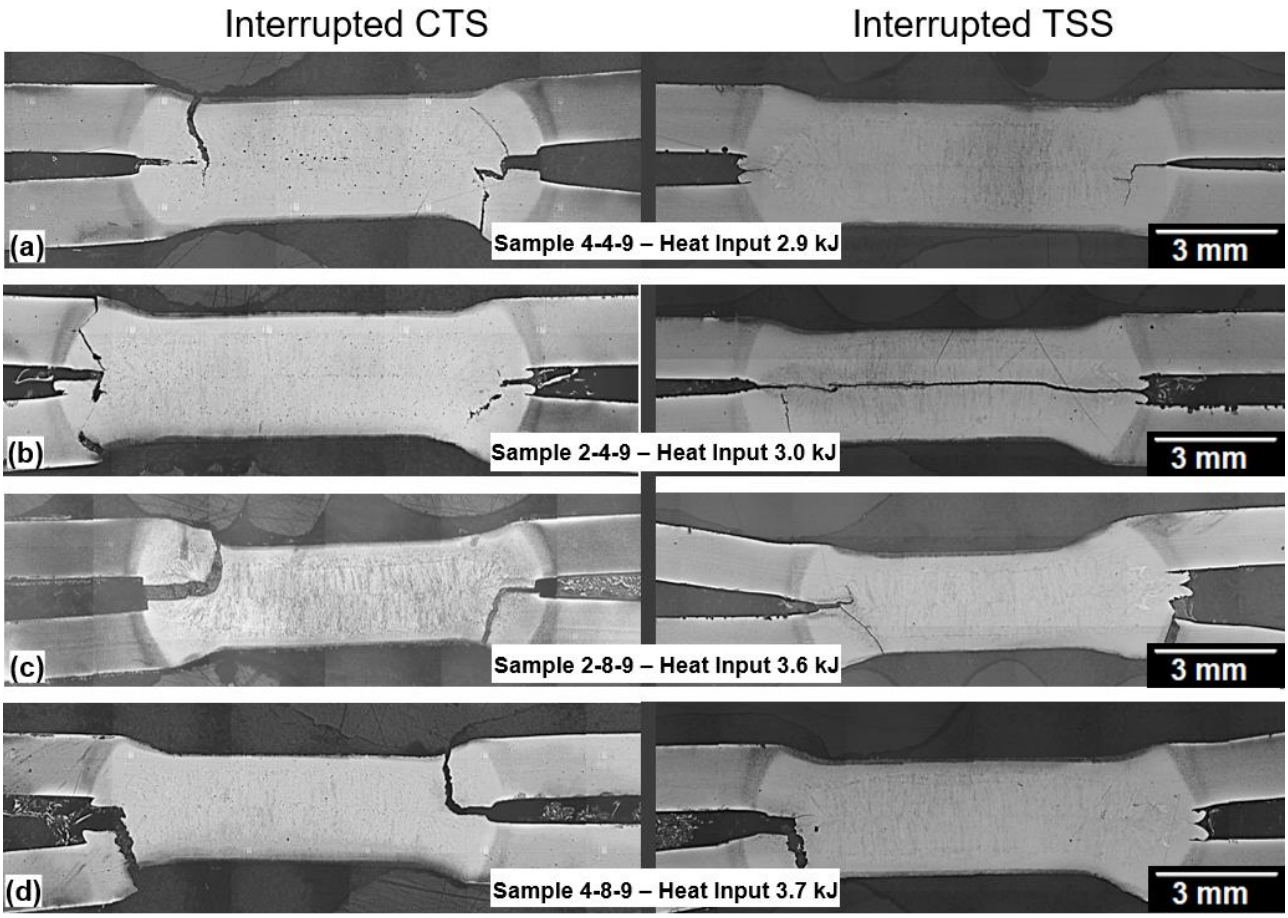


**Figure 5.18: Failure mode comparison for samples with no halo, left column showing interrupted CTS and right column showing interrupted TSS (a) sample 4-4-9, (b) sample 2-4-9, (c) sample 2-8-9, and (d) sample 4-8-9.**

Although no evidence of the halo was seen on the samples presented in Figure 5.18, there is evidence of crack propagation around the fusion boundary for samples 4-4-9 and 2-4-9, shown in Figure 5.18 (a) and (b). Again, the samples show no discernable fracture propagation pattern, with some samples failing interfacially and others failing at various points across the FZ and HAZ. There is no distinct correlation between the samples that failed interfacially and lower strength values.

Work by Sherepenko et al. [93, 94] and Mohamadizadeh et al. [94] have correlated failure around the fusion zone to the halo's presence, with crack propagation being initiated and propagated across the fusion boundary. The same mechanism was seen in the previous chapter for single pulse welds that showed evidence of the halo, but it is not correlated to multi-pulse welds with clear evidence of softening around the fusion boundary. Studies have shown that partial thickness failure with button pull fracture is one of the

most prevalent types of fracture in AHSS, mainly because of their complex microstructure [62, 112]. It is also accepted that the fracture mode in the RSW of AHSS is a complex phenomenon that depends on multiple factors, including the geometry and metallurgy of the weld and the loading mode [113].

Other driving factors besides the occurrence of halo in these welds may be leading to the failure modes seen in Figures 5.17 and 5.18, and contrary to what was proposed earlier, the presence of halo is not the sole factor affecting the energy absorption of the joints and consequently leading to lower CTS results. Although this study does characterize a strong correlation between halo elimination and increased joint strength, another possible mechanism affecting energy absorption might be the fusion zone and base material's hardness ratio. Previous studies have discussed how the FZ/BM hardness ratio influences the failure mode and weld strength in resistance spot welding, with a low hardness ratio having a detrimental effect on weld strength [114]. Figure 5.19 shows the microhardness comparison between samples welded with a high and low secondary current, or samples with and without the halo, where it can be seen that samples with no halo have fusion zone hardness values of as high as 620 HV, while samples with halo have a maximum hardness of 560 HV. It can be concluded that samples welded with a high secondary current have significantly higher hardness ratios than those welded with a low secondary current.

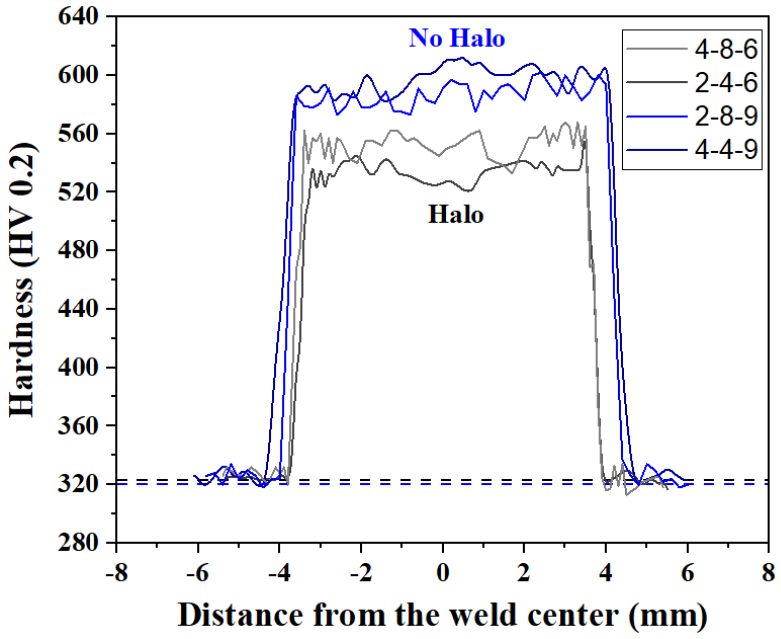


**Figure 5.19: Microhardness comparison for samples with and without the halo.**

Figure 5.20 shows the plot of the lowest hardness value measured in the fusion zone of the weld versus normalized CTS for the samples, where it can be seen that there is a strong correlation between increasing

FZ hardness and increasing CTS values. It is possible that increased fusion zone hardness affects the strength of the weld by introducing increased bending moments during testing, leading to higher energy absorption and, consequently, higher strength values. Overall, the works presented here and in Chapter 4 indicate that the weld nugget properties are closely related to the failure mode and energy absorption capability of Q&P980 welds. Further work is required to confirm this correlation and to investigate other possible mechanisms affecting the weld strength and failure mode of Q&P joints.

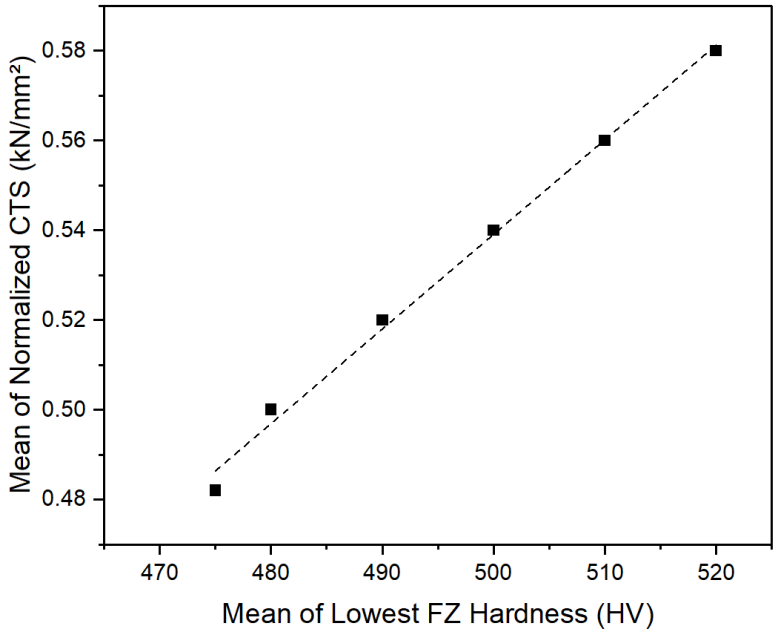


**Figure 5.20: Lowest fusion zone hardness versus normalized CTS for multi-pulse weld schedules.**

## 5.5 Weld Optimization

This work's optimization approach considered all of the multi-pulse weld parameters previously described, namely the cooling time between pulses, second pulse length, and second pulse current. The interactions between these parameters were analyzed to maximize both normalized CTS and normalized TSS values to achieve a weld schedule that offers the optimal weldability in terms of weld strength while decoupling it from the effects of weld nugget diameters.

Through the analysis of the main effects plot shown in Figure 5.10, it is possible to determine that the maximum TSS value occurs when the lowest cooling time between pulses is used and the highest second pulse time and second pulse current. A similar analysis of Figure 5.11 shows that the maximum CTS value

occurs with the highest second pulse time and second pulse current, with the cooling time between pulses not being significant. It follows that optimal weldability is found when using schedule 2-8-9, which corresponds to a heat input of 3.6 kJ. Minitab was used to confirm this analysis through its response optimization tool, also finding that optimal control factors to obtain maximum peak loads and failure energy are A1 (cooling time of 2 cycles), B2 (second pulse time of 8 cycles), and C2 (second pulse current of 9 kA). The results from this analysis can be found in Appendix A. At the optimal condition, the peak CTS value is 4.41 kN, and peak TSS is 21.1 kN. No halo is present in these welds, and the fusion zone hardness is around 600 HV.

## 5.6 Summary and Further Work

This study explored the use of multi-pulse weld schedules to improve the resistance spot weldability of Q&P steels and control the occurrence of a softened zone around the fusion boundary in the joints. The influence of various process parameters such as cooling time between pulses, second pulse current, and second pulse time on weld diameter, hardness, and failure load was established.

The microstructure, hardness profiles, tensile shear strength, cross tension strength, and failure behavior of the multi-pulse welds were analyzed. Multi-pulsing was successfully used to improve weldability by increasing both CTS and TSS values. It was found that these improvements in weld strength occur even after normalization of the values, showing that this result is not merely related to an increase in weld diameter with the second pulse. The use of a second pulse with a high current was strongly correlated to the halo's elimination, which was related to increased cross-tension strength for the samples that showed no softening. However, it is not clear how using a second pulse with a high current could avoid the halo formation, and further study is required to understand this relationship.

This work also discussed how the failure behavior of multi-pulse welds appears to have no established correlation to halo occurrence, and the presence of this softened region may not be the sole factor affecting the energy absorption of the joints. It was proposed that the fracture behavior might be correlated to the hardness ratio of the fusion zone and base material. The possible influence of fusion zone hardness on the mechanical performance of the welds was described. Further study is required to confirm this correlation and achieve a better understanding of this mechanism.

Finally, this chapter also investigated the weld schedule that led to optimized weldability by maximizing weld strength. Through the analysis of various weld parameters, it was found that optimal weldability is achieved by using a weld schedule with the lowest cooling time between pulses (2 cycles), largest length

of the second pulse (8 cycles), and highest second pulse current (9 kA). At the optimal condition, the peak CTS value is 4.41 kN, peak TSS is 21.1 kN, and the ductility ratio is 0.21. No halo was observed in these welds, and the fusion zone hardness is around 600 HV.

# Chapter 6
# Analysis of the Correlation between Thermal Cycles and Weld Strength

Chapter 5 investigated the effect of multi-pulse weld schedules in the resistance spot welding behavior of Q&P980 steels, finding that multi-pulse samples where a high secondary current was used showed no evidence of the halo and also exhibited higher CTS values than samples with a low secondary pulse current and prominent softening around the fusion boundary. However, the mechanism responsible for eliminating the halo when a high secondary current was used was not clear.

This chapter investigates the underlying causes for these effects using computational simulation, where the weld schedules used in the previous chapter were simulated with the finite element code Sysweld®. The results of this study are discussed in the following sections.

## 6.1 Simulation Design and Analysis

As resistance spot welding is governed by a complex interaction between thermal, mechanical, electrical, and metallurgical phenomena, modeling the process often requires specialized software [102]. This work used the finite element method (FEM) software package Sysweld® to simulate the RSW process of two Q&P980 sheets under the weld conditions described in Chapter 5 to investigate the various parameters' effect on the weld. Strong coupling, where every thermal simulation step is followed by mechanical simulation step and geometry actualization, was used to provide better accuracy of the simulation, and four phases were used to simulate the phase transformations throughout the process. Sysweld® processed the input data using the parameters assigned in the process set-up, including the electrode geometry and custom weld mesh, Q&P980's thermophysical and mechanical properties, and spot weld parameters such as frequency, squeezing force, squeezing time, and the length and intensity of each electrical load. The simulation results' initial analysis returned plots showing the weld's overall characteristics under the established process parameters, including the molten nugget's shape and the molten zone's evolution.

Figure 6.1 shows the final shape of the molten zone as predicted by the simulation and a comparison between the simulation results and a micrograph of a sample welded under the same schedule. The simulation results showed good agreement with experimental observations, where the nugget diameters obtained from the simulation were, on average, 13.5% smaller than the ones measured through microscopy. The minimum weld size for the material was achieved at 7.5 kA in the simulation and at 7.3 kA

experimentally at the time of testing, with a divergence of approximately 2.7%, also showing good agreement between the model and experimental results. It should also be noted that the model was developed and previously tested by Mr. C. DiGiovanni in their own resistance spot welding work, where the simulation predictions were within the range of the experimental results [115].

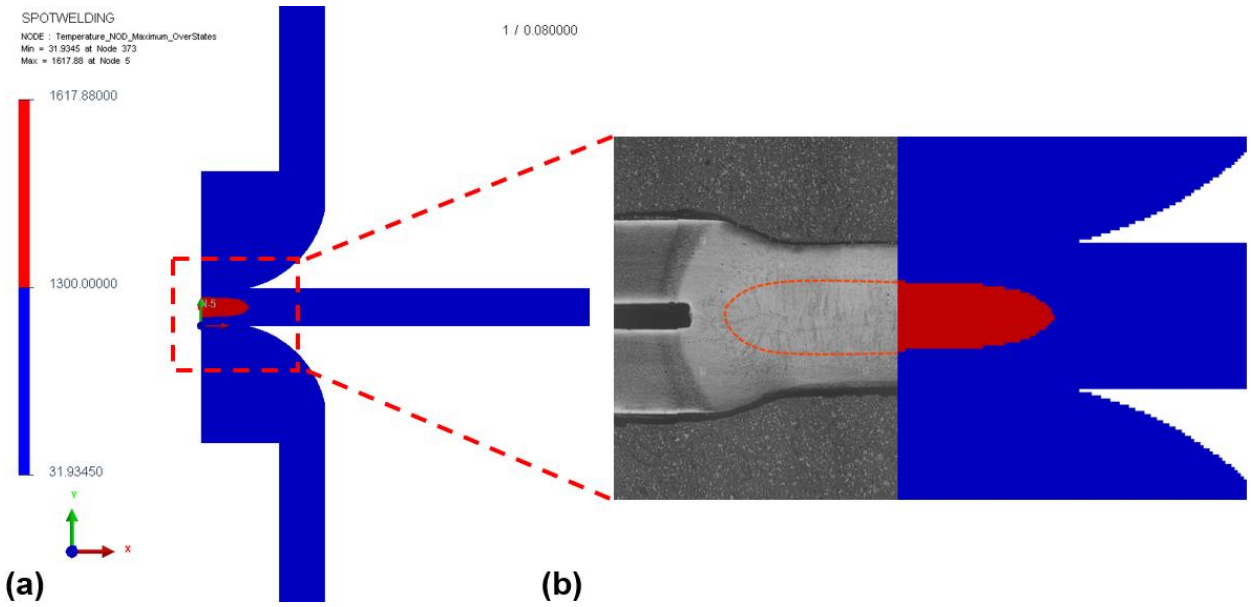


**Figure 6.1: (a) Sysweld® plot showing the final shape of the molten zone after welding and (b) Comparison between simulation results and micrograph of the sample under the same schedule.**

Figure 6.2 shows the molten zone's evolution for a sample where a low secondary current was used and for a sample where a high current was used. The plots in Figure 6.2 represent the evolution of the molten zone in $mm^3$ over time, where it is possible to see the intervals where nugget formation and growth took place. While all samples with a low secondary current showed a single peak in this plot, representing the nugget formation during the first pulse, all samples where a high secondary current was used showed another peak after the first one, formed during the second pulse. These initial results indicate that a second pulse with a high current consistently led to the re-growth of the weld nugget after the first pulse, while a second pulse with a lower current did not.

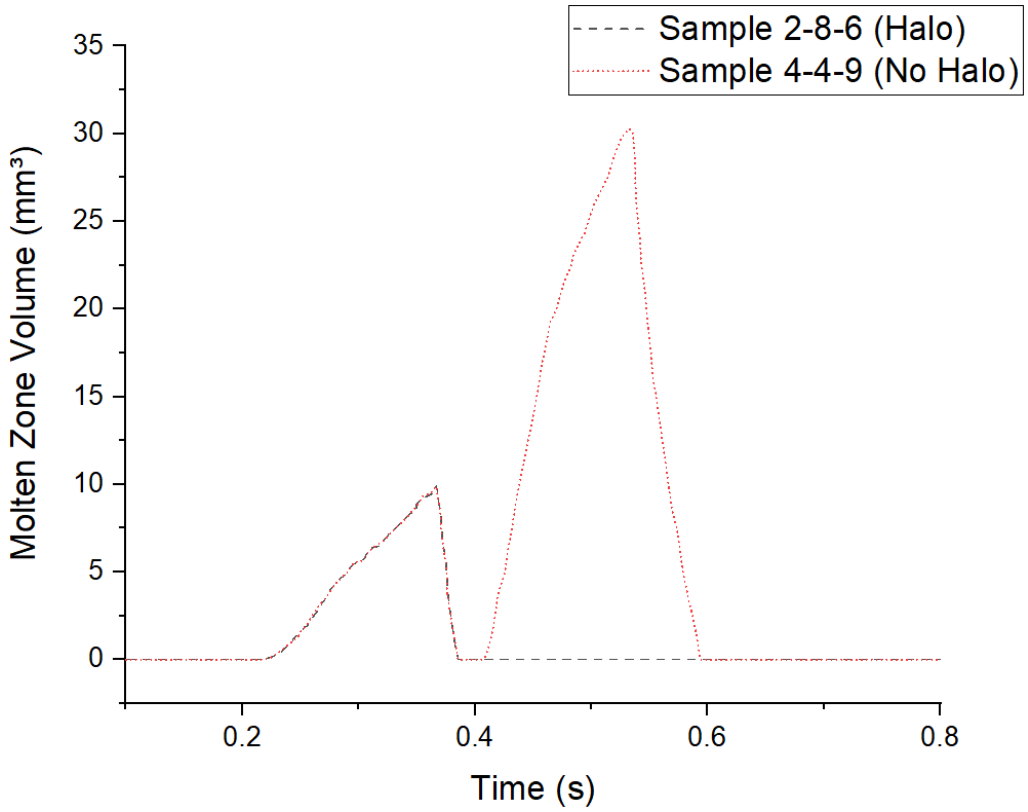


**Figure 6.2: Evolution of the molten zone in $mm^3$ for a sample with low secondary current, 2-8-6, and sample with high secondary current, 4-4-9.**

## 6.2 Effect of Thermal Cycles on Failure Mode

Post-processing of the simulation results was performed to obtain the welding process's thermal profile for each of the simulated weld schedules. For this study's purposes, the focus of the simulation work was on the thermal results generated by the software, which included the temperature at nodes and the phase proportions at the elements.

Figure 6.3 presents a contour plot generated with Sysweld® showing the thermal profile of a weld after the formation of the molten nugget, captured at the time point of 0.36 s after the start of the welding cycle. The melting temperature of Q&P980 was used as the temperature boundary for the plot such that the area in grey can visually identify the molten metal.

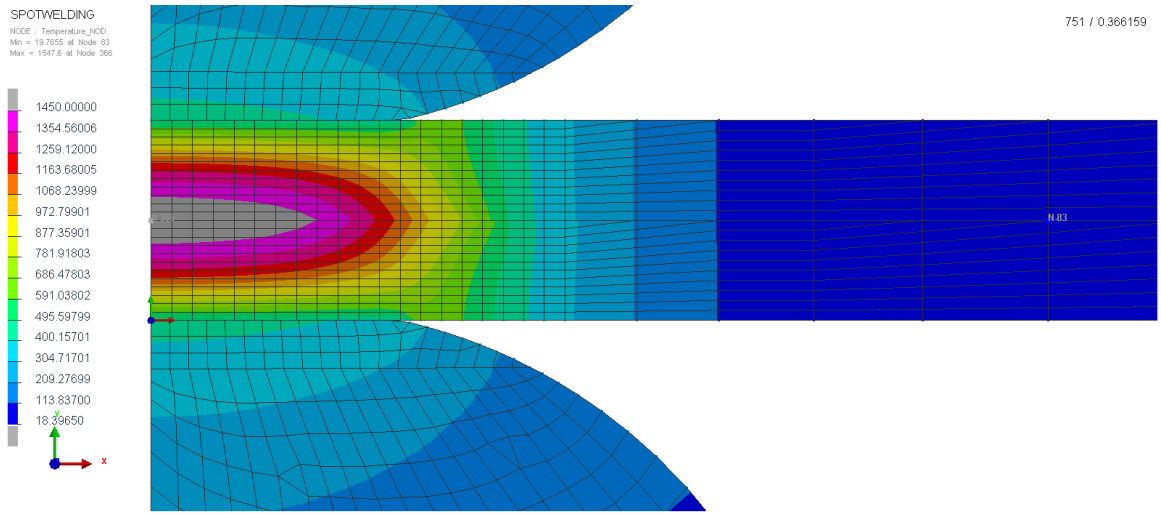


**Figure 6.3: Sysweld® contour plot showing the weld's thermal profile after the formation of the molten nugget.**

Contour plots were generated for each simulated weld schedule's thermal profile to visualize the molten nugget's evolution over time and identify the nodes that intersected with the final position of the fusion boundary. This was done to trace the variation of the temperature at the fusion boundary over time, shown in Figure 6.4.

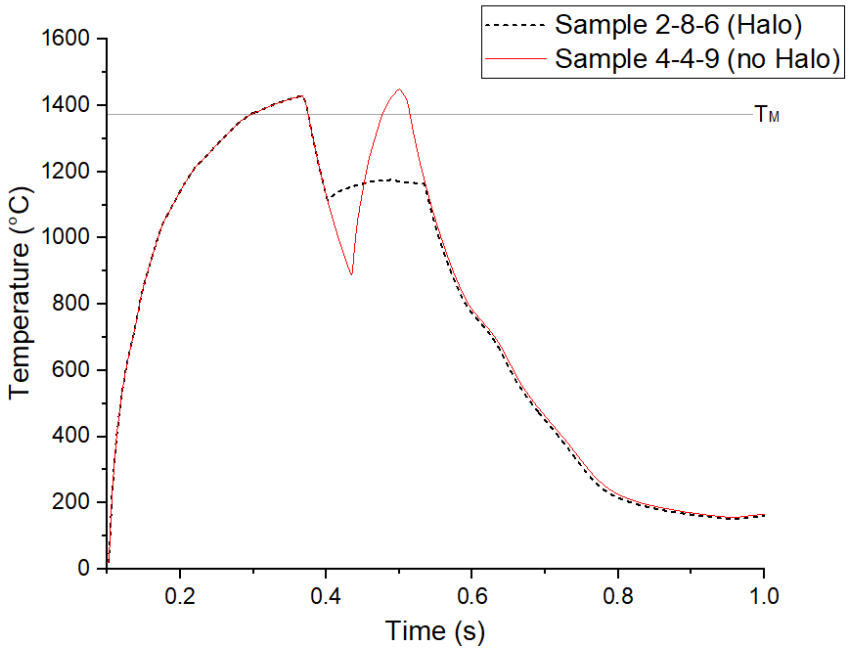


**Figure 6.4: Temperature at the fusion boundary after different multi-pulse weld schedules.**

All weld schedules showed two distinct peaks in temperature during the welding process, one corresponding to the first pulse and another to the second pulse. While all samples with a low secondary current presented a smaller secondary peak, almost flat in shape, samples with a high secondary current presented a secondary peak that reached and even exceeded the first one's temperature. Although Figure 6.4 only illustrates the temperature profile for samples 2-8-6 and 4-4-9 for ease of representation, this trend was consistently seen among all samples with and without the halo, where the samples that showed evidence of the halo were the ones where the secondary current resulted in a lower temperature at the second pulse. Samples with no halo showed a high temperature at the second pulse.

When considering the melting temperature of Q&P980, it is clear that a second pulse with a high current elevated the temperature of the weld above that of the melting point of the steel, remelting the material and leading to regrowth of the weld nugget. However, a secondary pulse with a low current does not cause remelting and regrowth of the weld nugget. This is in agreement with the results shown in Figure 6.2, where it was seen that samples with a low secondary current only showed nugget growth during the first pulse.

This observation is also in agreement with what was seen in Figure 5.4, which showed the cross-section of samples where a high secondary current was used. As previously described in the literature, two distinct nuggets can be seen with a multi-pulse weld schedule where the second pulse has a higher current than the first pulse. Weld schedules where the secondary pulse does not have enough intensity to remelt the nugget effectively slow down the solidification rate but exhibit only the primary nugget formed during the first pulse. To further investigate nugget regrowth and position of the fusion boundary, Figures 6.5 and 6.6 were plotted to illustrate the radius of the fusion boundary over time for samples with low secondary current and high secondary current. As expected, the nugget's regrowth is related to an increase in weld diameter for the samples with a high secondary current. However, the results discussed in Chapter 5 show that the increase in cross-tension strength related to these samples is independent from an increase in diameter. Even after normalizing the CTS values, samples with a high secondary current showed significantly higher load-bearing than samples with a low secondary current. The work presented in Chapter 5 also described the correlation between halo elimination and an improvement in CTS, where the relationship between a low secondary current and the halo occurrence was also made clear.

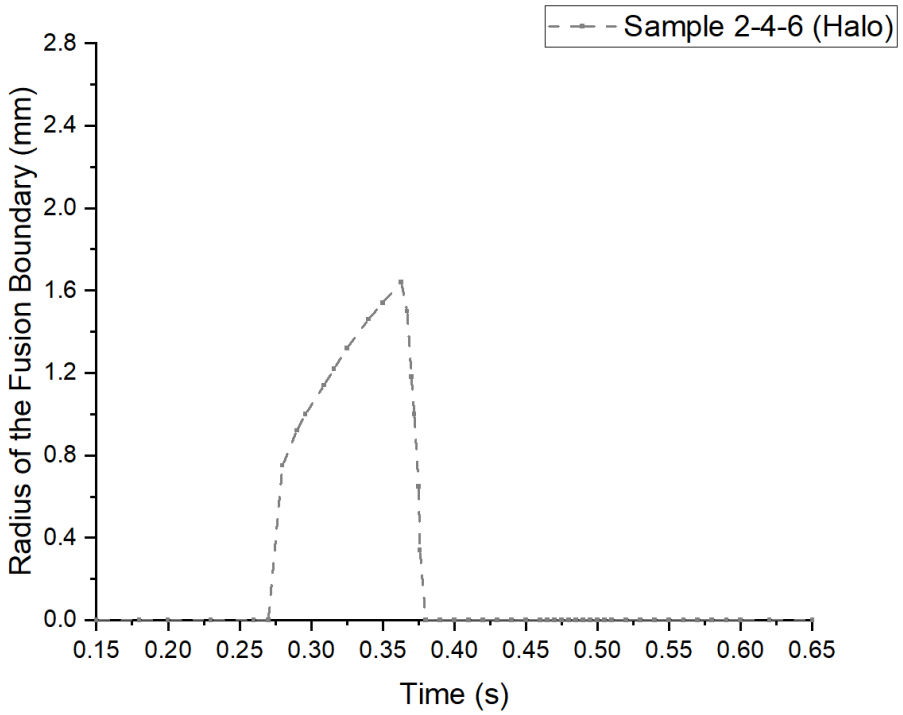


**Figure 6.5: Radius of the fusion boundary over time for samples with a low secondary current.**

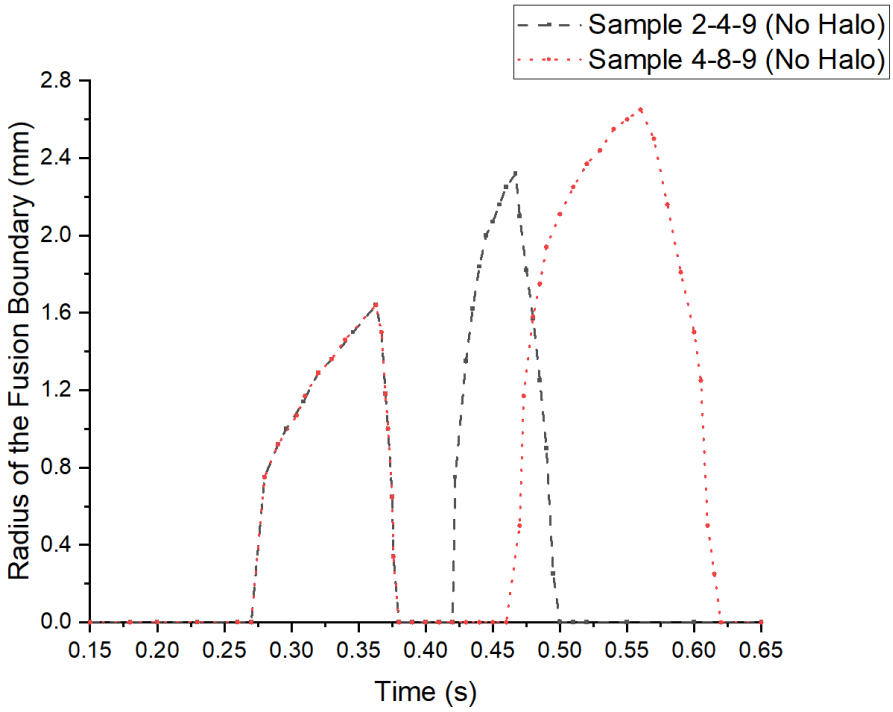


**Figure 6.6: Radius of the fusion boundary over time for samples with a high secondary current.**

As described in Chapter 2, halo formation has been explained in the literature due to the carbon redistribution at the fusion boundary when the molten nugget boundary remains static towards the end of the welding cycle [93, 96]. None of the samples with a high secondary current showed evidence of the halo, and all of them showed consistent remelting of the nugget based on the simulation results. It can be concluded from the current results that samples with a high secondary current not only cause nugget regrowth but also lead the last position fusion boundary to remain "less stationary" towards the end of the cycle than in samples with a low secondary current, effectively avoiding the occurrence of the halo.

However, as was also discussed in Chapter 5, it is possible that the halo is not the only factor driving the failure mode of the welds and consequently affecting the CTS values of the joints. It was proposed that another possible mechanism behind energy absorption of the welds could be the hardness ratio of the fusion zone and base material, where samples with a high secondary current had significantly higher hardness ratios leading to higher energy absorption and consequently higher strength values.

It can be seen from Figure 6.4 that samples with a high secondary current also had slightly higher cooling rates than samples with a low secondary current. The cooling rate for sample 2-8-6, welded with a low secondary current, was calculated to be approximately 2970 °C/s, while for sample 4-4-9, it was found to be approximately 3450 °C/s. High cooling rates are related to increased volume fractions of martensite and increased hardness [116–118]. As such, the simulation results described in this section can also elucidate how the thermal profile of the welds correlates to the alternate weld strength mechanism proposed in this work.

## 6.3 Summary

The work reported in this chapter described how the second pulse current is possibly related to the formation of a softened zone at the fusion boundary of resistance spot welds. A computational simulation was used to identify mechanisms behind how a high secondary current correlates to an increase in weld strength, describing how it consistently led to remelting and re-growth of the weld nugget after the first pulse, and also how a variation in the cooling rate affects martensite volume fraction and consequently fusion zone hardness.

# Chapter 7
# Conclusion and Recommendations

Quenched and partitioned steels offer a combination of high strength and high ductility that has seen increased attention from the automotive industry. Still, the general effects of the resistance spot welding process on the mechanical properties of Q&P joints are not yet fully understood. The present work sought to correlate the microstructure development to the mechanical behavior of resistance spot welded Q&P steels under various weld schedules, to optimize these steels' weldability, and to understand the correlation between the weld's thermal cycles and the failure mode of the joints.

This study described the occurrence of a softened region at the fusion boundary of the welds, known as the halo, which was reported for the first time for Q&P steels. The possible influence of this softened region on the mechanical performance of the welds was described. A method to control the halo's occurrence was proposed, and a theory was suggested regarding how this softened region correlates to the joints' failure mode. However, the present work could not fully establish a clear correlation between the halo's presence and the welds' energy absorption capability. This study also found that optimal weldability is achieved using a multi-pulse weld schedule with a low cooling time between the first and second pulse, a long second pulse, and a high second pulse current.

The microstructures within different Q&P steel's weld zones were investigated, where no heat-affected zone softening was observed in the welds. This work also studied the fracture mechanisms in RSW of Q&P980, with failure consistently initiating at the weld's notch and, in most cases, propagating around the fusion zone of the weld. Q&P's weldability was optimized by maximizing the joints' load-bearing capacity through the use of multi-pulse weld schedules. Possible mechanisms behind the improvement in these steels' weld strength were discussed, including the elimination of the halo and an increase in the hardness ratio of the fusion zone and base material. The sections below further detail the specific findings presented in the various chapters of this dissertation.

## 7.1 Failure Behavior and Mechanical Properties in the Resistance Spot Welding of Quenched and Partitioned Steels

This study presented the results obtained from the resistance spot welding of quenched and partitioned steels and dual-phase steels. The results show that all welds failed in a partial or full button pull-out mode, and all cross-tension strength and tensile shear strength samples met the minimum requirements commonly

used in the automotive industry, and in fact, exceed them by as much as 70%. On further analysis, evidence was found pointing towards the presence of a transient softening at the fusion boundary, leading to further studies to characterize that phenomenon and correlate it to the welding conditions of Q&P steels. The specific conclusions that may be drawn from this study are as follows:

1. Although Q&P980 offers a satisfactory welding range, it presents lower weldability than DP980. Q&P steels require higher currents to achieve acceptable weld nuggets and show expulsion at lower currents. Given the chemical composition of Q&P980, its narrower window can be explained by its higher electrical resistivity, which leads to higher susceptibility to expulsion.

2. Q&P980 welds achieved fusion zone hardness values as high as 580 HV, with no evident heat-affected zone softening as the hardness throughout the weld joint was consistently above that of the base material. DP980 achieves a maximum hardness of around 440 HV in the fusion zone and significant softening in the HAZ.

3. Q&P980 showed evidence of hardening in the HAZ, which was related to a secondary hardening effect where the tempered martensite transformed into ferrite with fine carbides.

4. The measured weld strength for the joints in this study was similar to what was reported in the literature, with an increase in weld diameter leading to increased CTS and TSS values. Values as high as 15.6 kN were found for the TSS test of Q&P980, and CTS showed results as high as 3.2 kN. DP980 welds showed TSS results as high as 17.5 kN and CTS of 6.9 kN.

5. Although there was a slight decrease in peak TSS and CTS for Q&P980 compared to previous studies, all TSS and CTS values met and exceeded the minimum requirements given by automotive guidelines.

6. Fractography of Q&P980's interrupted CTS samples showed crack propagation along the fusion boundary. Evidence was seen of a transient softened region (Halo), which possibly leads to a decrease in the welds' energy absorption capability.

## 7.2 Optimization of Weld Performance by Varying Weld Schedules

Weldability of Q&P980 welds was analyzed through multi-pulse welding schedules and the study of their effects on the joints' microstructural development and their mechanical properties. It was found that multi-pulsing effectively increased both CTS and TSS values of the welds compared to the results seen under a single pulse weld schedule. Results showed that using a second pulse with a high current effectively avoided

the formation of a softened zone and increased CTS values. However, no discernible pattern was found linking this observation to the welds' failure mode, where regardless of the presence of the halo, there was no clear failure path route in the joints. It was alternatively proposed that the halo ring's presence might not be the sole factor affecting the welds' preferred failure path. Weldability optimization was applied by analyzing the weld parameters to maximize both CTS and TSS. The main conclusions from this work were:

1. Secondary pulse time had the strongest effect on nugget diameter, where a long second pulse led to a larger nugget, and although not as significant, so did a higher second pulse current. As both current and time are the main factors indicating the heat generated during the RSW process, these effects were expected. The cooling time between pulses had little effect on the nugget diameter.

2. There is no significant TSS difference between samples with halo (15.95 ± 2.05 kN) and samples with no halo (18.2 ± 3.87 kN). Although there seems to be no impact of the halo in the TSS values of Q&P980, multi-pulsing effectively increased TSS results and improved the joints' weldability.

3. Samples with no halo have statistically significantly higher CTS values (4.07 ± 0.61 kN) than samples with halo (3.38 ± 0.29 kN).

4. A second pulse with a high current was strongly correlated to the elimination of the halo. However, the failure behavior of multi-pulse welds appears to have no established correlation to the halo’s occurrence. Samples with and without evidence of the halo exhibited failure progressing through the HAZ, around the FZ in partial pullout mode, and interfacially through the FZ.

5. Samples with no halo have significantly higher hardness ratios than those with halo, which can affect the weld's strength by introducing increased bending moments during testing, which leads to higher energy absorption and, consequently, higher strength values.

6. Optimal weldability is achieved when using a weld schedule with a cooling time between pulses of 2 cycles, a second pulse length of 8 cycles, and a second pulse current of 9 kA. At the optimal condition, the peak CTS value is 4.41 kN, peak TSS is 21.1 kN, and the ductility ratio is 0.21. No halo is present in these welds, and the fusion zone hardness is around 600 HV.

## 7.3 Analysis of the Correlation between Thermal Cycles and Weld Strength

A computational simulation was applied to investigate the mechanism behind how different multi-pulse weld schedules affect the formation of the halo and how they correlate to the increase in weld strength seen in the previous work. It was found through the study of the thermal cycles in the weld that a second pulse

with a higher current effectively leads to remelting and re-growth of the nugget, also showing an increase in the cooling rate towards the end of the weld cycle. The key conclusions of this work are as follows:

1. While all samples with a low secondary current showed a single interval where nugget growth occurred, related to the formation of the weld nugget during the first pulse, all samples where a high secondary current was used showed the presence of another peak after the first one, formed during the second pulse. This indicates that a second pulse with a high current led to the weld nugget's re-growth after the first pulse.

2. A secondary pulse with a high current consistently elevated the weld's temperature above that of the steel's melting point, remelting the material and leading to the weld nugget regrowth. However, a secondary pulse with a low current does not cause remelting and regrowth of the molten zone.

3. A high secondary current causes nugget regrowth and leads the fusion boundary to remain less static towards the end of the weld cycle, which is possibly related to eliminating the halo.

## 7.4 Recommendations for Future Work

While this work showed that a multi-pulsing welding schedule is an effective method to improve resistance spot weldability of Q&P steels, additional work is needed to fully understand the microstructural and mechanical changes leading to this observed effect. The possibility of further improving the multi-pulsing welding schedules to achieve better optimization should also be fully explored, perhaps by expanding the use of computational simulation as an investigational tool to determine an ideal pulsing technique before experimental work.

The relationship between the formation of the softened region at the fusion boundary, known as halo, and the failure mode of the welds should be further investigated to achieve a complete understanding of the halo ring's impact on resistance spot welds. The current study could not establish a relationship between the occurrence of the halo and the fracture path in tensile shear-strength or cross-tension strength, so it is of particular interest to determine if there is a correlation between those effects.

Finally, while this work presented a comprehensive study of the welding behavior of Q&P980, it is essential to expand the investigation to quenched and partitioned steels with different tensile strength levels, such as Q&P1180.

# Bibliography


1. Wang L, Speer JG (2013) Quenching and Partitioning Steel Heat Treatment. Metallogr Microstruct Anal 2:268–281. https://doi.org/10.1007/s13632-013-0082-8

2. DiGiovanni C, Biro E, Zhou NY (2019) Impact of liquid metal embrittlement cracks on resistance spot weld static strength. Sci Technol Weld Join 24:218–224. https://doi.org/10.1080/13621718.2018.1518363

3. Wintjes E, Digiovanni C, He L, et al. (2019) Quantifying the link between crack distribution and resistance spot weld strength reduction in liquid metal embrittlement susceptible steels. Weld World 63. https://doi.org/10.1007/s40194-019-00712-5

4. He L, DiGiovanni C, Han X, et al. (2019) Suppression of liquid metal embrittlement in resistance spot welding of TRIP steel. Sci Technol Weld Join 24:579–586. https://doi.org/10.1080/13621718.2019.1573011

5. Matlock DK, Speer JG (2009) Third Generation of AHSS: Microstructure Design Concepts. In: Haldar A, Suwas S, Bhattacharjee D (eds) Microstructure and Texture in Steels. Springer London, London, pp 185–205

6. Speer J, De Moor E, Findley K, et al. (2011) Analysis of Microstructure Evolution in Quenching and Partitioning Automotive Sheet Steel. Metall Mater Trans Phys Metall Mater Sci 42:3591–3601. https://doi.org/10.1007/s11661-011-0869-7

7. Speer J, Matlock DK, De Cooman BC, Schroth JG (2003) Carbon partitioning into austenite after martensite transformation. Acta Mater 51:2611–2622. https://doi.org/10.1016/S1359-6454(03)00059-4

8. Edmonds DV, He K, Rizzo FC, et al. (2006) Quenching and partitioning martensite—A novel steel heat treatment. Mater Sci Eng A 438–440:25–34. https://doi.org/10.1016/j.msea.2006.02.133

9. (2012) AWS D8.9M. Test methods for evaluating the resistance spot welding behavior of automotive sheet steel materials, Third ed. American Welding Society (AWS), Miami, Fl, USA

10. (2013) AWS D8.1M. Specification for Automotive Weld Quality-Resistance Spot Welding of Steel., Second ed. American Welding Society (AWS), Miami, Fl, USA

11. Fonstein N (2015) Advanced High Strength Sheet Steels. Springer International Publishing

12. Geck PE (2014) Automotive Lightweighting Using Advanced High-Strength Steels. SAE International, Warrendale, PA

13. Bleck W, Brühl F, Ma Y, Sasse C (2019) Materials and Processes for the Third-generation Advanced High-strength Steels. BHM Berg- Hüttenmänn Monatshefte 164:466–474. https://doi.org/10.1007/s00501-019-00904-y

14. Demeri MY (2013) Advanced High-Strength Steels - Science, Technology, and Applications. ASM International

15. Tolouei R, Titheridge H (2009) Vehicle mass as a determinant of fuel consumption and secondary safety performance. Transp Res Part Transp Environ 14:385–399. https://doi.org/10.1016/j.trd.2009.01.005

16. Shome M, Tumuluru M (2015) Welding and Joining of Advanced High Strength Steels (AHSS). Elsevier

17. Mallick PK (2010) Materials, Design and Manufacturing for Lightweight Vehicles. Woodhead Publishing

18. Billur E, Altan T (2013) Three generations of advanced high-strength steels for automotive applications, Part I. Stamp J

19. Billur E, Altan T (2014) Three generations of advanced high-strength steels for automotive applications, Part II. Stamp J

20. Billur E, Altan T (2014) Three generations of advanced high-strength steels for automotive applications, Part III. Stamp J

21. Matlock DK, Speer JG (2009) Third generation of AHSS: microstructure design concepts

22. Lesch C, Kwiaton N, Klose FB (2017) Advanced High Strength Steels (AHSS) for Automotive Applications − Tailored Properties by Smart Microstructural Adjustments. Steel Res Int 88:1700210. https://doi.org/10.1002/srin.201700210

23. Hardwick AP, Outteridge T (2016) Vehicle lightweighting through the use of molybdenum-bearing advanced high-strength steels (AHSS). Int J Life Cycle Assess 21:1616–1623. https://doi.org/10.1007/s11367-015-0967-7

24. 2019 Chevy Silverado reduces weight and increases strength with AHSS. https://automotive.arcelormittal.com/news_and_stories/cases/2018ChevroletSilverado. Accessed 3 Jan 2021

25. Tasan CC, Diehl M, Yan D, et al. (2015) An Overview of Dual-Phase Steels: Advances in Microstructure-Oriented Processing and Micromechanically Guided Design. Annu Rev Mater Res 45:391–431. https://doi.org/10.1146/annurev-matsci-070214-021103

26. Saha DC, Nayak SS, Biro E, et al. (2014) Mechanism of Secondary Hardening in Rapid Tempering of Dual-Phase Steel. Metall Mater Trans A 45:6153–6162. https://doi.org/10.1007/s11661-014-2591-8

27. Dual Phase steels. https://automotive.arcelormittal.com/products/flat/first_gen_AHSS/DP. Accessed 5 Jan 2021

28. de Diego-Calderón I, De Knijf D, Monclús MA, et al. (2015) Global and local deformation behavior and mechanical properties of individual phases in a quenched and partitioned steel. Mater Sci Eng A 630:27–35. https://doi.org/10.1016/j.msea.2015.01.077

29. Stewart RA, Speer JG, Thomas BG, et al. (2019) Quenching and Partitioning of Plate Steels: Partitioning Design Methodology. Metall Mater Trans A 50:4701–4713. https://doi.org/10.1007/s11661-019-05337-3

30. Frint P, Kaiser T, Mehner T, et al. (2019) Strain-rate sensitive ductility in a low-alloy carbon steel after quenching and partitioning treatment. Sci Rep 9:17023. https://doi.org/10.1038/s41598-019-53303-1

31. Seo EJ, Cho L, Estrin Y, De Cooman BC (2016) Microstructure-mechanical properties relationships for quenching and partitioning (Q&P) processed steel. Acta Mater 113:124–139. https://doi.org/10.1016/j.actamat.2016.04.048

32. De Moor E, Lacroix S, Clarke AJ, et al. (2008) Effect of Retained Austenite Stabilized via Quench and Partitioning on the Strain Hardening of Martensitic Steels. Metall Mater Trans A 39:2586–2595. https://doi.org/10.1007/s11661-008-9609-z

33. Marder AR (2000) The metallurgy of zinc-coated steel. Prog Mater Sci 45:191–271. https://doi.org/10.1016/S0079-6425(98)00006-1

34. Amirudin A, Thierry D (1996) Corrosion mechanisms of phosphated zinc layers on steel as substrates for automotive coatings. Prog Org Coat 28:59–75. https://doi.org/10.1016/0300-9440(95)00554-4

35. DiGiovanni C, Ghatei Kalashami A, Goodwin F, et al. (2021) Occurrence of sub-critical heat affected zone liquid metal embrittlement in joining of advanced high strength steel. J Mater Process Technol 288:116917. https://doi.org/10.1016/j.jmatprotec.2020.116917

36. DiGiovanni C, Bag S, Mehling C, et al. (2019) Reduction in liquid metal embrittlement cracking using weld current ramping. Weld World 63:1583–1591. https://doi.org/10.1007/s40194-019-00790-5

37. Hamlaoui Y, Tifouti L, Pedraza F (2010) On the corrosion resistance of porous electroplated zinc coatings in different corrosive media. Corros Sci 52:1883–1888. https://doi.org/10.1016/j.corsci.2010.02.024

38. Junqueira DM (2018) Analysis of spot weld distribution in a weldment—numerical simulation and topology optimization. Int J Adv Manuf Technol 9

39. Lee Y, Jeong H, Park K, et al. (2017) Development of numerical analysis model for resistance spot welding of automotive steel. J Mech Sci Technol 31:3455–3464. https://doi.org/10.1007/s12206-017-0634-y

40. Pouranvari M, Marashi SPH (2013) Critical review of automotive steels spot welding: process, structure and properties. Sci Technol Weld Join 18:361–403. https://doi.org/10.1179/1362171813Y.0000000120

41. Williams NT, Parker JD (2004) Review of resistance spot welding of steel sheets Part 1 Modelling and control of weld nugget formation. Int Mater Rev 49:45–75. https://doi.org/10.1179/095066004225010523

42. Zhang H, Senkara J (2011) Resistance Welding. CRC Press/Taylor & Francis Group, Boca Raton, FL

43. Kimchi M, Phillips DH (2017) Resistance Spot Welding: Fundamentals and Applications for the Automotive Industry. Synth Lect Mech Eng 1:i–115. https://doi.org/10.2200/S00792ED1V01Y201707MEC005

44. Enami M, Farahani M, Sohrabian M (2016) Evaluation of mechanical properties of Resistance Spot Welding and Friction Stir Spot Welding on Aluminium Alloys. 12

45. Dickinson DW Characterization of Spot Welding Behavior by Dynamic Electrical Parameter Monitoring. 7

46. Kim T, Park H, Rhee * S (2005) Optimization of welding parameters for resistance spot welding of TRIP steel with response surface methodology. Int J Prod Res 43:4643–4657. https://doi.org/10.1080/00207540500137365

47. Bohnenkamp U, Sandström R, Grimvall G (2002) Electrical resistivity of steels and face-centered-cubic iron. J Appl Phys 92:4402–4407. https://doi.org/10.1063/1.1502182

48. Koley S, Ray T, Mohanty I, et al. (2019) Prediction of electrical resistivity of steel using artificial neural network. Ironmak Steelmak 46:383–391. https://doi.org/10.1080/03019233.2017.1403109

49. Lee H-T, Chang Y-C (2020) Effect of Double Pulse Resistance Spot Welding Process on 15B22 Hot Stamped Boron Steel. Metals 10:1279. https://doi.org/10.3390/met10101279

50. Eftekharimilani P, van der Aa EM, Hermans MJM, Richardson IM (2017) Microstructural characterization of double pulse resistance spot welded advanced high strength steel. Sci Technol Weld Join 22:545–554. https://doi.org/10.1080/13621718.2016.1274848

51. Kim JW, Murugan SP, Yoo J-H, et al. (2020) Enhancing nugget size and weldable current range of ultra-high-strength steel using multi-pulse resistance spot welding. Sci Technol Weld Join 25:235–242. https://doi.org/10.1080/13621718.2019.1680483

52. Sawanishi C, Ogura T, Taniguchi K, et al. (2014) Mechanical properties and microstructures of resistance spot welded DP980 steel joints using pulsed current pattern. Sci Technol Weld Join 19:52–59. https://doi.org/10.1179/1362171813Y.0000000165

53. Jahandideh A, Hamedi M, Mansourzadeh SA, Rahi A (2011) An experimental study on effects of post-heating parameters on resistance spot welding of SAPH440 steel. Sci Technol Weld Join 16:669–675. https://doi.org/10.1179/1362171811Y.0000000053

54. Koichi T, Yasuaki O, Rinsei I (2015) Development of Next Generation Resistance Spot Welding Technologies Improving the Weld Properties of Advanced High Strength Steel Sheets. 7

55. David SA, DebRoy T (1992) Current issues and problems in welding science. Science 257:497+

56. Roy S (2020) Austenite decomposition in the coarse grain heat affected zone of X80 line pipe steel. The University of British Columbia

57. Stadler M, Gruber M, Schnitzer R, Hofer C (2020) Microstructural characterization of a double pulse resistance spot welded 1200 MPa TBF steel. Weld World 64:335–343. https://doi.org/10.1007/s40194-019-00835-9

58. Baltazar Hernandez VH, Panda SK, Okita Y, Zhou NY (2010) A study on heat affected zone softening in resistance spot welded dual phase steel by nanoindentation. J Mater Sci 45:1638–1647. https://doi.org/10.1007/s10853-009-4141-0

59. Pouranvari M, Sobhani S, Goodarzi F (2018) Resistance spot welding of MS1200 martensitic advanced high strength steel: Microstructure-properties relationship. J Manuf Process 31:867–874. https://doi.org/10.1016/j.jmapro.2018.01.009

60. Dancette S, Fabrègue D, Massardier V, et al. (2011) Experimental and modeling investigation of the failure resistance of Advanced High Strength Steels spot welds. Eng Fract Mech 78:2259–2272. https://doi.org/10.1016/j.engfracmech.2011.04.013

61. Zhao HS, Li W, Zhu X, et al. (2016) Analysis of the relationship between retained austenite locations and the deformation behavior of quenching and partitioning treated steels. Mater Sci Eng A 649:18–26. https://doi.org/10.1016/j.msea.2015.09.088

62. Radakovic DJ, Tumuluru M (2012) An Evaluation of the Cross-Tension Test of Resistance Spot Welds in High-Strength Dual-Phase Steels. Weld J 91:8

63. Wang X, Zhang Y, Ju J, et al. (2016) Characteristics of Welding Crack Defects and Failure Mode in Resistance Spot Welding of DP780 Steel. J Iron Steel Res Int 23:1104–1110. https://doi.org/10.1016/S1006-706X(16)30163-7

64. Pouranvari M, Marashi SPH (2009) Similar and dissimilar RSW of low carbon and austenitic stainless steels: effect of weld microstructure and hardness profile on failure mode: MST. Mater Sci Technol 25:1411–1416

65. Sun X, Stephens EV, Khaleel MA (2008) Effects of fusion zone size and failure mode on peak load and energy absorption of advanced high strength steel spot welds under lap shear loading conditions. Eng Fail Anal 15:356–367. https://doi.org/10.1016/j.engfailanal.2007.01.018

66. Pouranvari M, Marashi SPH, Safanama DS (2011) Failure mode transition in AHSS resistance spot welds. Part II: Experimental investigation and model validation. Mater Sci Eng A 528:8344–8352. https://doi.org/10.1016/j.msea.2011.08.016

67. Daneshpour S, Riekehr S, Koçak M, Gerritsen CHJ (2009) Mechanical and fatigue behaviour of laser and resistance spot welds in advanced high strength steels. Sci Technol Weld Join 14:20–25. https://doi.org/10.1179/136217108X336298

68. Tamizi M, Pouranvari M, Movahedi M (2017) Welding metallurgy of martensitic advanced high strength steels during resistance spot welding. Sci Technol Weld Join 22:327–335. https://doi.org/10.1080/13621718.2016.1240979

69. Pouranvari M, Marashi SPH (2010) Key factors influencing mechanical performance of dual phase steel resistance spot welds. Sci Technol Weld Join 15:149–155. https://doi.org/10.1179/136217109X12590746472535

70. Khan MI, Kuntz ML, Su P, et al. (2007) Resistance and friction stir spot welding of DP600: a comparative study. Sci Technol Weld Join 12:175–182. https://doi.org/10.1179/174329307X159801

71. Zhao D, Wang Y, Liang D, Zhang P (2017) An investigation into weld defects of spot-welded dual-phase steel. Int J Adv Manuf Technol 92:3043–3050. https://doi.org/10.1007/s00170-017-0398-7

72. Wang B, Hua L, Wang X, Li J (2016) Effects of multi-pulse tempering on resistance spot welding of DP590 steel. Int J Adv Manuf Technol 86:2927–2935. https://doi.org/10.1007/s00170-016-8361-6

73. Kishore K, Kumar P, Mukhopadhyay G (2019) Resistance spot weldability of galvannealed and bare DP600 steel. J Mater Process Technol 271:237–248. https://doi.org/10.1016/j.jmatprotec.2019.04.005

74. Chabok A, van der Aa E, De Hosson JTM, Pei YT (2017) Mechanical behavior and failure mechanism of resistance spot welded DP1000 dual phase steel. Mater Des 124:171–182. https://doi.org/10.1016/j.matdes.2017.03.070

75. Biro E, McDermid JR, Embury JD, Zhou Y (2010) Softening Kinetics in the Subcritical Heat-Affected Zone of Dual-Phase Steel Welds. Metall Mater Trans A 41:2348–2356. https://doi.org/10.1007/s11661-010-0323-2

76. Baltazar Hernandez VH, Nayak SS, Zhou Y (2011) Tempering of Martensite in Dual-Phase Steels and Its Effects on Softening Behavior. Metall Mater Trans A 42:3115–3129. https://doi.org/10.1007/s11661-011-0739-3

77. Guo W, Wan Z, Peng P, et al. (2018) Microstructure and mechanical properties of fiber laser welded QP980 steel. J Mater Process Technol 256:229–238. https://doi.org/10.1016/j.jmatprotec.2018.02.015

78. Li W, Ma L, Peng P, et al. (2018) Microstructural evolution and deformation behavior of fiber laser welded QP980 steel joint. Mater Sci Eng A 717:124–133. https://doi.org/10.1016/j.msea.2018.01.050

79. Lin H, Jiang H, Wang Y, Tian S (2019) Microstructure gradient characteristics and mechanical properties of friction stir welded high strength QP980 steel. Mater Res Express 6:126584. https://doi.org/10.1088/2053-1591/ab5a92

80. Wang B, Duan QQ, Yao G, et al. (2014) Investigation on fatigue fracture behaviors of spot welded Q&P980 steel. Int J Fatigue 66:20–28. https://doi.org/10.1016/j.ijfatigue.2014.03.004

81. Lei M, Pan H (2012) Comparative study of resistance spot welding performance between cold-rolled dp980 and q&p980 steels. Baosteel Tech Res 6. https://doi.org/10.3969/j.issn.1674-3458.2012.01.008

82. Liu XD, Xu YB, Misra RDK, et al. (2019) Mechanical properties in double pulse resistance spot welding of Q&P 980 steel. J Mater Process Technol 263:186–197. https://doi.org/10.1016/j.jmatprotec.2018.08.018

83. Luo C, Zhang Y (2019) Constitutive relationship of fusion zone in the spot welds of advance high strength steels. J Manuf Process 45:624–633. https://doi.org/10.1016/j.jmapro.2019.08.007

84. Chen T, Ling Z, Wang M, Kong L (2020) Effect of a slightly concave electrode on resistance spot welding of Q&P1180 steel. J Mater Process Technol 285:116797. https://doi.org/10.1016/j.jmatprotec.2020.116797

85. Fan C-L, Ma B-H, Chen D-N, et al. (2016) Spall Strength of Resistance Spot Weld for QP Steel. Chin Phys Lett 33:036201. https://doi.org/10.1088/0256-307X/33/3/036201

86. Fan C, Ma B, Chen D, et al. (2019) Uniaxial compression properties of fusion zone martensite in resistance spot-weld for QP980 steel. Weld World 63:161–166. https://doi.org/10.1007/s40194-018-0646-y

87. Ling Z, Chen T, Kong L, et al. (2019) Liquid Metal Embrittlement Cracking During Resistance Spot Welding of Galvanized Q&P980 Steel. Metall Mater Trans A 50:5128–5142. https://doi.org/10.1007/s11661-019-05388-6

88. Spena PR, De Maddis M, Lombardi F (2015) Mechanical Strength and Fracture of Resistance Spot Welded Advanced High Strength Steels. Procedia Eng 109:450–456. https://doi.org/10.1016/j.proeng.2015.06.262

89. Russo Spena P, Rossi S, Wurzer R (2017) Effects of Welding Parameters on Strength and Corrosion Behavior of Dissimilar Galvanized Q&P and TRIP Spot Welds. Metals 7:534. https://doi.org/10.3390/met7120534

90. Russo Spena P, De Maddis M, Lombardi F, Rossini M (2016) Dissimilar Resistance Spot Welding of Q&P and TWIP Steel Sheets. Mater Manuf Process 31:291–299. https://doi.org/10.1080/10426914.2015.1048476

91. Russo Spena P, De Maddis M, D'Antonio G, Lombardi F (2016) Weldability and Monitoring of Resistance Spot Welding of Q&P and TRIP Steels. Metals 6:270. https://doi.org/10.3390/met6110270

92. Ozturk Yilmaz I, Bilici AY, Aydin H (2019) Microstructure and mechanical properties of dissimilar resistance spot welded DP1000–QP1180 steel sheets. J Cent South Univ 26:25–42. https://doi.org/10.1007/s11771-019-3980-3

93. Sherepenko O, Kazemi O, Rosemann P, et al. (2019) Transient Softening at the Fusion Boundary of Resistance Spot Welds: A Phase Field Simulation and Experimental Investigations for Al–Si-coated 22MnB5. Metals 10:10. https://doi.org/10.3390/met10010010

94. Sherepenko O, Jüttner S (2019) Transient softening at the fusion boundary in resistance spot welded ultra-high strengths steel 22MnB5 and its impact on fracture processes. Weld World 63:151–159. https://doi.org/10.1007/s40194-018-0633-3

95. Li YB, Li DL, David SA, et al. (2016) Microstructures of magnetically assisted dual-phase steel resistance spot welds. Sci Technol Weld Join 21:555–563. https://doi.org/10.1080/13621718.2016.1141493

96. Mohamadizadeh A, Biro E, Worswick M (2020) Shear band formation at the fusion boundary and failure behaviour of resistance spot welds in ultra-high-strength hot-stamped steel. Sci Technol Weld Join 1–8. https://doi.org/10.1080/13621718.2020.1773057

97. Yurioka N, Suzuki H, Ohshita S, Saito S (1983) Determination of Necessary Preheating Temperature in Steel Welding. Weld Res Suppl 7

98. Resistance Welding Manufacturing Alliance (RWMA) (2003) Resistance Welding Manual (Revised 4th Edition). American Welding Society (AWS)

99. (2019) AWS C1.1M. Recommended Practices for Resistance Welding., Sixth edition. American Welding Society (AWS)

100. Ramos HME, Tavares SMO, de Castro PMST (2018) Numerical modelling of welded T-joint configurations using SYSWELD. Sci Technol Mater 30:6–15. https://doi.org/10.1016/j.stmat.2018.08.002

101. Nguyen NT, Kim DY, Song JH, et al. (2012) Numerical prediction of various failure modes in spotwelded metals. Int J Automot Technol 13:459–467. https://doi.org/10.1007/s12239-012-0043-2

102. Eshraghi M, Tschopp MA, Zaeem MA, Felicelli SD (2016) A Parametric Study of Resistance Spot Welding of a Dual-Phase Steel Using Finite Element Analysis. In: Marquis F (ed) Proceedings of the 8th Pacific Rim International Congress on Advanced Materials and Processing. Springer International Publishing, Cham, pp 3073–3080

103. Pakkanen J, Vallant R, Kičin M (2016) Experimental investigation and numerical simulation of resistance spot welding for residual stress evaluation of DP1000 steel. Weld World 60:393–402. https://doi.org/10.1007/s40194-016-0301-4

104. Farrance I, Frenkel R Uncertainty of Measurement: A Review of the Rules for Calculating Uncertainty Components through Functional Relationships. 27

105. Ludwigson DC, Schwerer FC (1971) The effect of composition on the resistivity of carbon steel sheet. Metall Mater Trans B 2:3500–3501. https://doi.org/10.1007/BF02811640

106. Kaiser JG, Dunn GJ, Eagar TW (1982) The Effect of Electrical Resistance on Nugget Formation During Spot Welding. Weld Res Suppl 8

107. Easterling K (1992) Introduction to the Physical Metallurgy of Welding. Elsevier

108. Ashiri R, Marashi SPH, Park, Y-D (2018) Weld Processing and Mechanical Responses of 1-GPa TRIP Steel Resistance Spot Welds. Weld J 97:157–169. https://doi.org/10.29391/2018.97.014

109. E04 Committee (2017) Standard Test Method for Microindentation Hardness of Materials. ASTM International, West Conshohocken, PA

110. Sangwal K, Surowska B, Błaziak P (2003) Analysis of the indentation size effect in the microhardness measurement of some cobalt-based alloys. Mater Chem Phys 77:511–520. https://doi.org/10.1016/S0254-0584(02)00086-X

111. Farges G, Degout D (1989) Interpretation of the indentation size effect in Vickers microhardness measurements-absolute hardness of materials. Thin Solid Films 181:365–374. https://doi.org/10.1016/0040-6090(89)90505-1

112. Russo Spena P, Cortese L, De Maddis M, Lombardi F (2016) Effects of Process Parameters on Spot Welding of TRIP and Quenching and Partitioning Steels. Steel Res Int 87:1592–1600. https://doi.org/10.1002/srin.201600007

113. Pouranvari M, Marashi SPH (2011) Failure mode transition in AHSS resistance spot welds. Part I. Controlling factors. Mater Sci Eng A 528:8337–8343. https://doi.org/10.1016/j.msea.2011.08.017

114. Zhang S, DiGiovanni C, He L, Zhou NY (2021) Weld hardness ratio and liquid metal embrittlement crack's detrimental effect on resistant spot weld strength. Sci Technol Weld Join 26:58–67. https://doi.org/10.1080/13621718.2020.1833517

115. DiGiovanni C, He L, Pistek U, et al. (2020) Role of spot weld electrode geometry on liquid metal embrittlement crack development. J Manuf Process 49:1–9. https://doi.org/10.1016/j.jmapro.2019.11.015

116. Yi Y, Li Q, Xing J, et al. (2019) Effects of cooling rate on microstructure, mechanical properties, and residual stress of Fe-2.1B (wt%) alloy. Mater Sci Eng A 754:129–139. https://doi.org/10.1016/j.msea.2019.03.061

117. Dumovic M, Dunne D, Norrish J, et al. (2018) Effect of cooling rate on microstructural evolution and hardness of self-shielded arc weld deposits containing 1 wt% aluminium. Weld World 62:685–697. https://doi.org/10.1007/s40194-018-0568-8

118. Wang Y, Hua J, Kong M, et al. (2016) Quantitative analysis of martensite and bainite microstructures using electron backscatter diffraction: MARTENSITE AND BAINITE MICROSTRUCTURES. Microsc Res Tech 79:814–819. https://doi.org/10.1002/jemt.22703

# Appendix A

### Supplementary Data for Chapter 5

## Factorial Regression: Diameter versus Cooling Time, 2nd Pulse Time, 2nd Pulse Current

### Coded Coefficients

| Term | Effect | Coef | SE Coef | T-Value | P-Value |
|---|---|---|---|---|---|
| Constant | | 6.13182 | 0.00643 | 953.89 | 0.000 |
| Cooling Time | 0.05000 | 0.02500 | 0.00754 | 3.32 | 0.045 |
| 2nd Pulse Time | 0.35000 | 0.17500 | 0.00754 | 23.22 | 0.000 |
| 2nd Pulse Current | 0.25000 | 0.12500 | 0.00754 | 16.58 | 0.000 |
| Cooling Time*2nd Pulse Time | 0.15000 | 0.07500 | 0.00754 | 9.95 | 0.002 |
| Cooling Time*2nd Pulse Current | -0.15000 | -0.07500 | 0.00754 | -9.95 | 0.002 |
| 2nd Pulse Time*2nd Pulse Current | 0.15000 | 0.07500 | 0.00754 | 9.95 | 0.002 |
| Cooling Time*2nd Pulse Time*2nd Pulse Current | -0.05000 | -0.02500 | 0.00754 | -3.32 | 0.045 |

| Term | VIF |
|---|---|
| Constant | |
| Cooling Time | 1.00 |
| 2nd Pulse Time | 1.00 |
| 2nd Pulse Current | 1.00 |
| Cooling Time*2nd Pulse Time | 1.00 |
| Cooling Time*2nd Pulse Current | 1.00 |
| 2nd Pulse Time*2nd Pulse Current | 1.00 |
| Cooling Time*2nd Pulse Time*2nd Pulse Current | 1.00 |

### Model Summary

| S | R-sq | R-sq(adj) | R-sq(pred) |
|---|---|---|---|
| 0.0213201 | 99.74% | 99.12% | 37.80% |

### Analysis of Variance

| Source | DF | Adj SS | Adj MS | F-Value | P-Value |
|---|---|---|---|---|---|
| Model | 7 | 0.515000 | 0.073571 | 161.86 | 0.001 |
| Linear | 3 | 0.375000 | 0.125000 | 275.00 | 0.000 |
| Cooling Time | 1 | 0.005000 | 0.005000 | 11.00 | 0.045 |
| 2nd Pulse Time | 1 | 0.245000 | 0.245000 | 539.00 | 0.000 |
| 2nd Pulse Current | 1 | 0.125000 | 0.125000 | 275.00 | 0.000 |

| | | | | | |
|---|---|---|---|---|---|
| 2-Way Interactions | 3 | 0.135000 | 0.045000 | 99.00 | 0.002 |
| Cooling Time*2nd Pulse Time | 1 | 0.045000 | 0.045000 | 99.00 | 0.002 |
| Cooling Time*2nd Pulse Current | 1 | 0.045000 | 0.045000 | 99.00 | 0.002 |
| 2nd Pulse Time*2nd Pulse Current | 1 | 0.045000 | 0.045000 | 99.00 | 0.002 |
| 3-Way Interactions | 1 | 0.005000 | 0.005000 | 11.00 | 0.045 |
| Cooling Time*2nd Pulse Time*2nd Pulse Current | 1 | 0.005000 | 0.005000 | 11.00 | 0.045 |
| Error | 3 | 0.001364 | 0.000455 | | |
| Curvature | 1 | 0.001364 | 0.001364 | * | * |
| Pure Error | 2 | 0.000000 | 0.000000 | | |
| Total | 10 | 0.516364 | | | |

## Regression Equation in Uncoded Units

Diameter = 6.707 - 0.200 Cooling Time - 0.4000 2nd Pulse Time
- 0.0667 2nd Pulse Current
+ 0.1000 Cooling Time*2nd Pulse Time
+ 0.0000 Cooling Time*2nd Pulse Current
+ 0.05000 2nd Pulse Time*2nd Pulse Current
- 0.00833 Cooling Time*2nd Pulse Time*2nd Pulse Current

## Alias Structure

| Factor | Name |
|---|---|
| A | Cooling Time |
| B | 2nd Pulse Time |
| C | 2nd Pulse Current |

| Aliases |
|---|
| I |
| A |
| B |
| C |
| AB |
| AC |
| BC |
| ABC |


Normal Plot of the Standardized Effects
(response is Diameter, α = 0.05)
Percent
99
95
90
80
70
60
50
40
30
20
10
5
1
-10
-5
0
5
10
15
20
25
Standardized Effect
B
C
BC
AB
A
ABC
AC
Effect Type
Significant
Factor Name
A Cooling Time
B 2nd Pulse Time
C 2nd Pulse Current

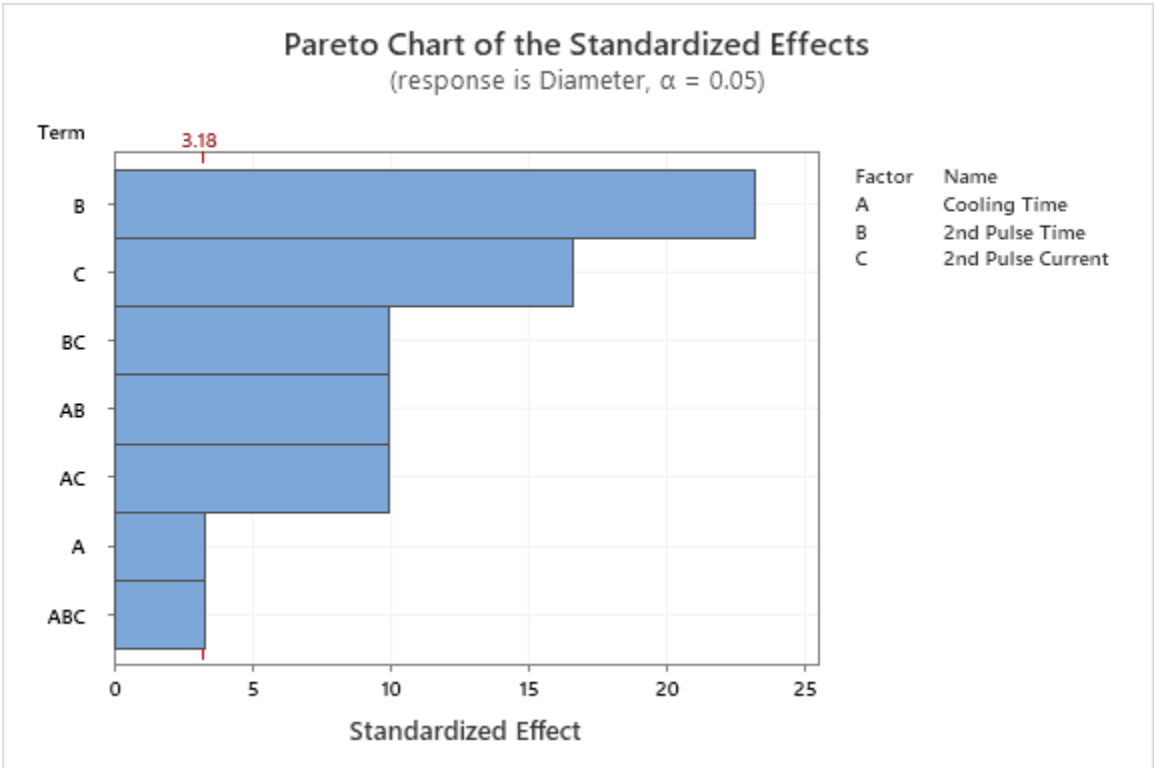
Pareto Chart of the Standardized Effects
(response is Diameter, α = 0.05)
Term
3.18
B
C
BC
AB
AC
A
ABC
0
5
10
15
20
25
Standardized Effect
Factor Name
A Cooling Time
B 2nd Pulse Time
C 2nd Pulse Current

# Factorial Regression: Low_FZ versus Cooling Time, 2nd Pulse Time, 2nd Pulse Current

## Coded Coefficients

| Term | Effect | Coef | SE Coef | T-Value | P-Value |
|---|---|---|---|---|---|
| Constant | | 497.55 | 2.31 | 215.00 | 0.000 |
| Cooling Time | 2.00 | 1.00 | 2.71 | 0.37 | 0.737 |
| 2nd Pulse Time | -16.50 | -8.25 | 2.71 | -3.04 | 0.056 |
| 2nd Pulse Current | 44.50 | 22.25 | 2.71 | 8.20 | 0.004 |
| Cooling Time*2nd Pulse Time | 12.50 | 6.25 | 2.71 | 2.30 | 0.105 |
| Cooling Time*2nd Pulse Current | -0.50 | -0.25 | 2.71 | -0.09 | 0.932 |
| 2nd Pulse Time*2nd Pulse Current | -6.00 | -3.00 | 2.71 | -1.11 | 0.350 |
| Cooling Time*2nd Pulse Time*2nd Pulse Current | -2.00 | -1.00 | 2.71 | -0.37 | 0.737 |

| Term | VIF |
|---|---|
| Constant | |
| Cooling Time | 1.00 |
| 2nd Pulse Time | 1.00 |
| 2nd Pulse Current | 1.00 |
| Cooling Time*2nd Pulse Time | 1.00 |
| Cooling Time*2nd Pulse Current | 1.00 |
| 2nd Pulse Time*2nd Pulse Current | 1.00 |
| Cooling Time*2nd Pulse Time*2nd Pulse Current | 1.00 |

## Model Summary

| S | R-sq | R-sq(adj) | R-sq(pred) |
|---|---|---|---|
| 7.67523 | 96.52% | 88.41% | 0.00% |

## Analysis of Variance

| Source | DF | Adj SS | Adj MS | F-Value | P-Value |
|---|---|---|---|---|---|
| Model | 7 | 4906.00 | 700.86 | 11.90 | 0.033 |
| Linear | 3 | 4513.00 | 1504.33 | 25.54 | 0.012 |
| Cooling Time | 1 | 8.00 | 8.00 | 0.14 | 0.737 |
| 2nd Pulse Time | 1 | 544.50 | 544.50 | 9.24 | 0.056 |
| 2nd Pulse Current | 1 | 3960.50 | 3960.50 | 67.23 | 0.004 |
| 2-Way Interactions | 3 | 385.00 | 128.33 | 2.18 | 0.269 |
| Cooling Time*2nd Pulse Time | 1 | 312.50 | 312.50 | 5.30 | 0.105 |
| Cooling Time*2nd Pulse Current | 1 | 0.50 | 0.50 | 0.01 | 0.932 |
| 2nd Pulse Time*2nd Pulse Current | 1 | 72.00 | 72.00 | 1.22 | 0.350 |
| 3-Way Interactions | 1 | 8.00 | 8.00 | 0.14 | 0.737 |

| | | | | | |
|---|---|---|---|---|---|
| Cooling Time*2nd Pulse Time*2nd Pulse Current | 1 | 8.00 | 8.00 | 0.14 | 0.737 |
| Error | 3 | 176.73 | 58.91 | | |
| Curvature | 1 | 176.73 | 176.73 | * | * |
| Pure Error | 2 | 0.00 | 0.00 | | |
| Total | 10 | 5082.73 | | | |

## Regression Equation in Uncoded Units

Low_FZ = 461 - 31.5 Cooling Time - 13.5 2nd Pulse Time + 15.3 2nd Pulse Current
+ 5.62 Cooling Time*2nd Pulse Time
+ 1.83 Cooling Time*2nd Pulse Current
- 0.00 2nd Pulse Time*2nd Pulse Current
- 0.333 Cooling Time*2nd Pulse Time*2nd Pulse Current

## Alias Structure

| Factor | Name |
|---|---|
| A | Cooling Time |
| B | 2nd Pulse Time |
| C | 2nd Pulse Current |

| Aliases |
|---|
| I |
| A |
| B |
| C |
| AB |
| AC |
| BC |
| ABC |


Normal Plot of the Standardized Effects
(response is Low_FZ, α = 0.05)
Percent
99
95
90
80
70
60
50
40
30
20
10
5
1
-4
-2
0
2
4
6
8
Standardized Effect
C
Effect Type
Not Significant
Significant
Factor Name
A Cooling Time
B 2nd Pulse Time
C 2nd Pulse Current

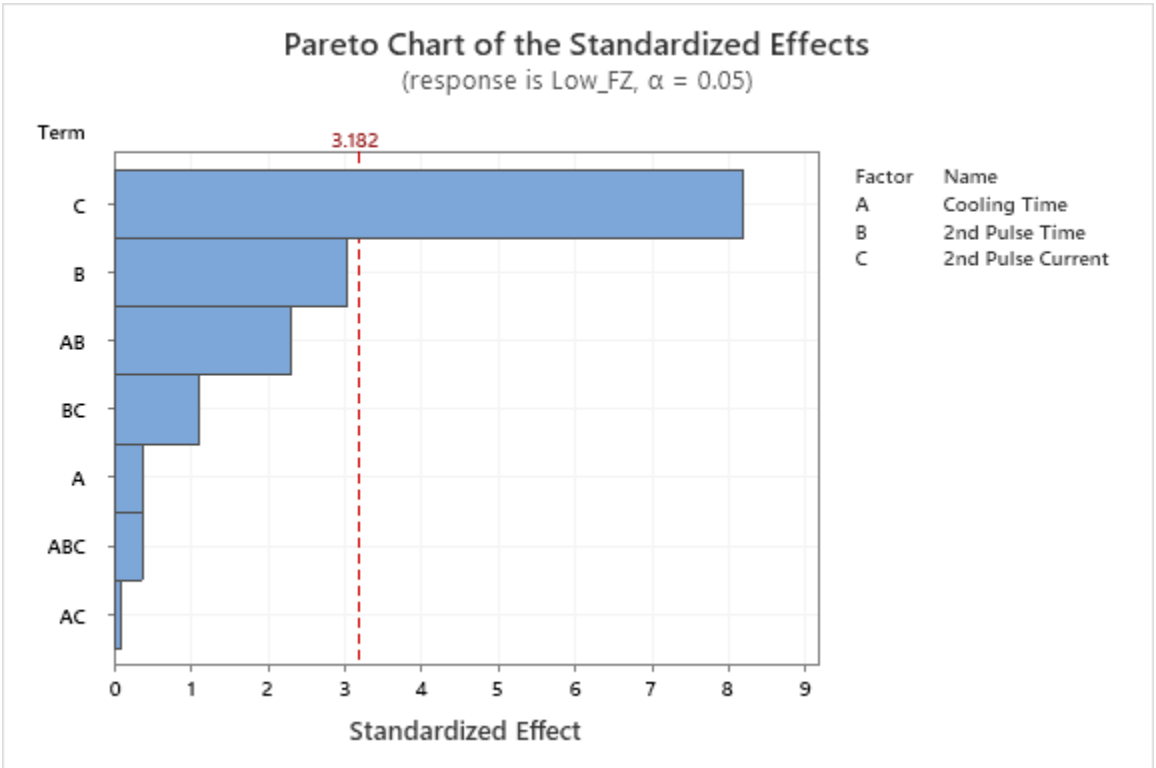
Pareto Chart of the Standardized Effects
(response is Low_FZ, α = 0.05)
Term
3.182
C
B
AB
BC
A
ABC
AC
0
1
2
3
4
5
6
7
8
9
Standardized Effect
Factor Name
A Cooling Time
B 2nd Pulse Time
C 2nd Pulse Current

# Factorial Regression: Normalized_TSS versus Cooling Time, 2nd Pulse Time, 2nd Pulse Current

## Coded Coefficients

| Term | Effect | Coef | SE Coef | T-Value | P-Value |
|---|---|---|---|---|---|
| Constant | | 2.3410 | 0.0251 | 93.42 | 0.000 |
| Cooling Time | -0.1858 | -0.0929 | 0.0294 | -3.16 | 0.051 |
| 2nd Pulse Time | 0.3194 | 0.1597 | 0.0294 | 5.44 | 0.012 |
| 2nd Pulse Current | 0.1825 | 0.0912 | 0.0294 | 3.10 | 0.053 |
| Cooling Time*2nd Pulse Time | -0.1659 | -0.0829 | 0.0294 | -2.82 | 0.067 |
| Cooling Time*2nd Pulse Current | -0.0278 | -0.0139 | 0.0294 | -0.47 | 0.669 |
| 2nd Pulse Time*2nd Pulse Current | 0.3179 | 0.1589 | 0.0294 | 5.41 | 0.012 |
| Cooling Time*2nd Pulse Time*2nd Pulse Current | 0.3410 | 0.1705 | 0.0294 | 5.80 | 0.010 |

| Term | VIF |
|---|---|
| Constant | |
| Cooling Time | 1.00 |
| 2nd Pulse Time | 1.00 |
| 2nd Pulse Current | 1.00 |
| Cooling Time*2nd Pulse Time | 1.00 |
| Cooling Time*2nd Pulse Current | 1.00 |
| 2nd Pulse Time*2nd Pulse Current | 1.00 |
| Cooling Time*2nd Pulse Time*2nd Pulse Current | 1.00 |

## Model Summary

| S | R-sq | R-sq(adj) | R-sq(pred) |
|---|---|---|---|
| 0.0831112 | 97.57% | 91.89% | 0.00% |

## Analysis of Variance

| Source | DF | Adj SS | Adj MS | F-Value | P-Value |
|---|---|---|---|---|---|
| Model | 7 | 0.831017 | 0.118717 | 17.19 | 0.020 |
| Linear | 3 | 0.339733 | 0.113244 | 16.39 | 0.023 |
| Cooling Time | 1 | 0.069066 | 0.069066 | 10.00 | 0.051 |
| 2nd Pulse Time | 1 | 0.204083 | 0.204083 | 29.55 | 0.012 |
| 2nd Pulse Current | 1 | 0.066585 | 0.066585 | 9.64 | 0.053 |
| 2-Way Interactions | 3 | 0.258675 | 0.086225 | 12.48 | 0.034 |
| Cooling Time*2nd Pulse Time | 1 | 0.055034 | 0.055034 | 7.97 | 0.067 |
| Cooling Time*2nd Pulse Current | 1 | 0.001544 | 0.001544 | 0.22 | 0.669 |
| 2nd Pulse Time*2nd Pulse Current | 1 | 0.202097 | 0.202097 | 29.26 | 0.012 |
| 3-Way Interactions | 1 | 0.232609 | 0.232609 | 33.67 | 0.010 |

| | | | | | |
|---|---|---|---|---|---|
| Cooling Time*2nd Pulse Time*2nd Pulse Current | 1 | 0.232609 | 0.232609 | 33.67 | 0.010 |
| Error | 3 | 0.020722 | 0.006907 | | |
| Curvature | 1 | 0.020722 | 0.020722 | * | * |
| Pure Error | 2 | 0.000000 | 0.000000 | | |
| Total | 10 | 0.851739 | | | |

## Regression Equation in Uncoded Units

Normalized_TSS = -4.56 + 2.783 Cooling Time + 1.086 2nd Pulse Time
+ 0.794 2nd Pulse Current
- 0.4678 Cooling Time*2nd Pulse Time
- 0.3503 Cooling Time*2nd Pulse Current
- 0.1175 2nd Pulse Time*2nd Pulse Current
+ 0.05684 Cooling Time*2nd Pulse Time*2nd Pulse Current

## Alias Structure

| Factor | Name |
|---|---|
| A | Cooling Time |
| B | 2nd Pulse Time |
| C | 2nd Pulse Current |

| Aliases |
|---|
| I |
| A |
| B |
| C |
| AB |
| AC |
| BC |
| ABC |

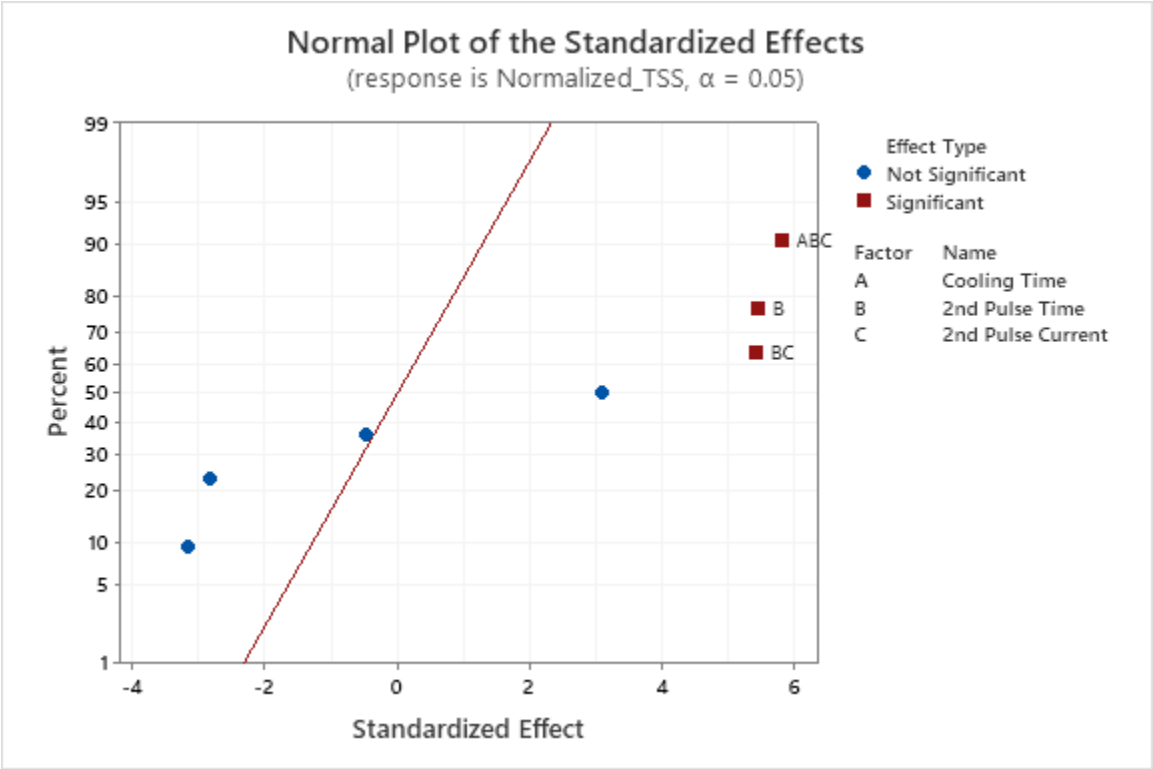
Normal Plot of the Standardized Effects
(response is Normalized_TSS, α = 0.05)
Percent
99
95
90
80
70
60
50
40
30
20
10
5
1
-4
-2
0
2
4
6
Standardized Effect
ABC
B
BC
Effect Type
Not Significant
Significant
Factor Name
A Cooling Time
B 2nd Pulse Time
C 2nd Pulse Current

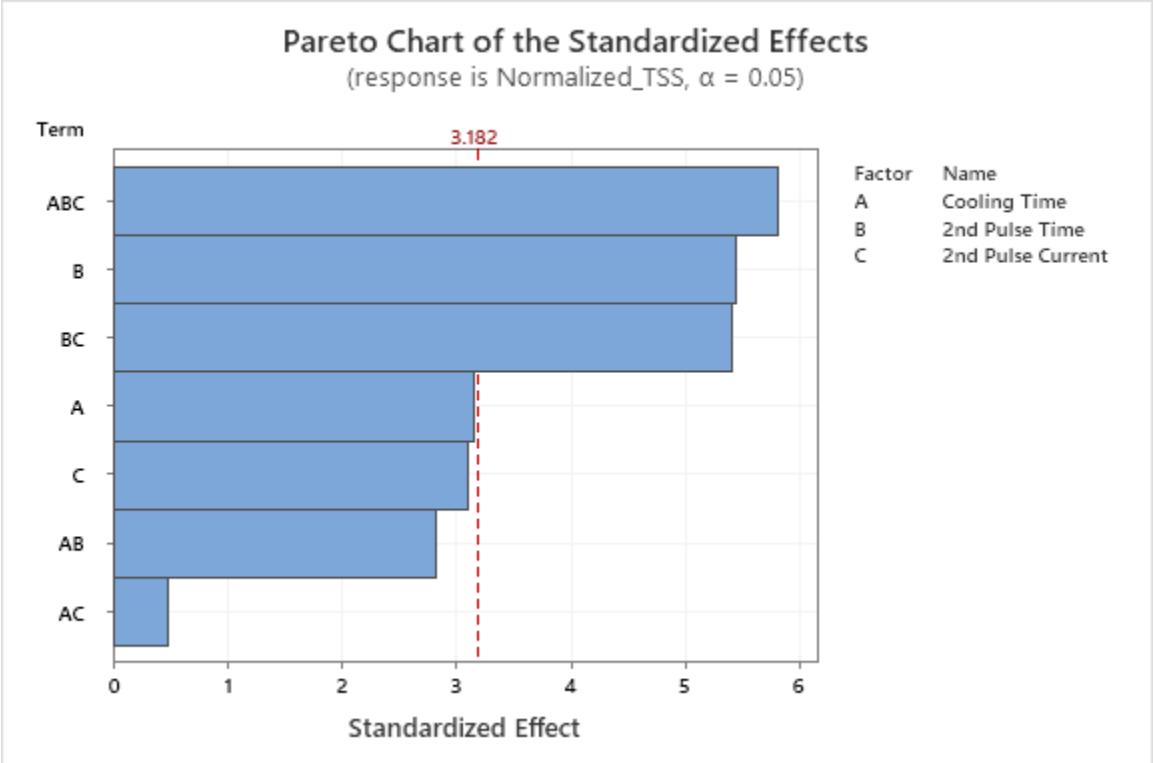
Pareto Chart of the Standardized Effects
(response is Normalized_TSS, α = 0.05)
Term
3.182
ABC
B
BC
A
C
AB
AC
0
1
2
3
4
5
6
Standardized Effect
Factor Name
A Cooling Time
B 2nd Pulse Time
C 2nd Pulse Current

# Factorial Regression: Normalized_CTS versus Cooling Time, 2nd Pulse Time, 2nd Pulse Current

## Coded Coefficients

| Term | Effect | Coef | SE Coef | T-Value |
|---|---|---|---|---|
| Constant | | 0.529098 | 0.000731 | 723.78 |
| Cooling Time | -0.000499 | -0.000249 | 0.000857 | -0.29 |
| 2nd Pulse Time | 0.008182 | 0.004091 | 0.000857 | 4.77 |
| 2nd Pulse Current | 0.093491 | 0.046746 | 0.000857 | 54.53 |
| Cooling Time*2nd Pulse Time | -0.035370 | -0.017685 | 0.000857 | -20.63 |
| Cooling Time*2nd Pulse Current | 0.027873 | 0.013936 | 0.000857 | 16.26 |
| 2nd Pulse Time*2nd Pulse Current | -0.046779 | -0.023390 | 0.000857 | -27.29 |
| Cooling Time*2nd Pulse Time*2nd Pulse Current | -0.011235 | -0.005618 | 0.000857 | -6.55 |

| Term | P-Value | VIF |
|---|---|---|
| Constant | 0.000 | |
| Cooling Time | 0.790 | 1.00 |
| 2nd Pulse Time | 0.017 | 1.00 |
| 2nd Pulse Current | 0.000 | 1.00 |
| Cooling Time*2nd Pulse Time | 0.000 | 1.00 |
| Cooling Time*2nd Pulse Current | 0.001 | 1.00 |
| 2nd Pulse Time*2nd Pulse Current | 0.000 | 1.00 |
| Cooling Time*2nd Pulse Time*2nd Pulse Current | 0.007 | 1.00 |

## Model Summary

| S | R-sq | R-sq(adj) | R-sq(pred) |
|---|---|---|---|
| 0.0024245 | 99.93% | 99.78% | 84.22% |

## Analysis of Variance

| Source | DF | Adj SS | Adj MS | F-Value | P-Value |
|---|---|---|---|---|---|
| Model | 7 | 0.026300 | 0.003757 | 639.17 | 0.000 |
| Linear | 3 | 0.017616 | 0.005872 | 998.91 | 0.000 |
| Cooling Time | 1 | 0.000000 | 0.000000 | 0.08 | 0.790 |
| 2nd Pulse Time | 1 | 0.000134 | 0.000134 | 22.78 | 0.017 |
| 2nd Pulse Current | 1 | 0.017481 | 0.017481 | 2973.85 | 0.000 |
| 2-Way Interactions | 3 | 0.008432 | 0.002811 | 478.17 | 0.000 |
| Cooling Time*2nd Pulse Time | 1 | 0.002502 | 0.002502 | 425.64 | 0.000 |
| Cooling Time*2nd Pulse Current | 1 | 0.001554 | 0.001554 | 264.33 | 0.001 |
| 2nd Pulse Time*2nd Pulse Current | 1 | 0.004377 | 0.004377 | 744.54 | 0.000 |

| | | | | | |
|---|---|---|---|---|---|
| 3-Way Interactions | 1 | 0.000252 | 0.000252 | 42.95 | 0.007 |
| Cooling Time*2nd Pulse Time*2nd Pulse Current | 1 | 0.000252 | 0.000252 | 42.95 | 0.007 |
| Error | 3 | 0.000018 | 0.000006 | | |
| Curvature | 1 | 0.000018 | 0.000018 | * | * |
| Pure Error | 2 | 0.000000 | 0.000000 | | |
| Total | 10 | 0.026318 | | | |

## Regression Equation in Uncoded Units

Normalized_CTS = 0.2357 - 0.1011 Cooling Time + 0.04492 2nd Pulse Time
+ 0.01636 2nd Pulse Current
+ 0.00520 Cooling Time*2nd Pulse Time
+ 0.02053 Cooling Time*2nd Pulse Current
- 0.002179 2nd Pulse Time*2nd Pulse Current
- 0.001873 Cooling Time*2nd Pulse Time*2nd Pulse Current

## Alias Structure

| Factor | Name |
|---|---|
| A | Cooling Time |
| B | 2nd Pulse Time |
| C | 2nd Pulse Current |

**Aliases**

I
A
B
C
AB
AC
BC
ABC

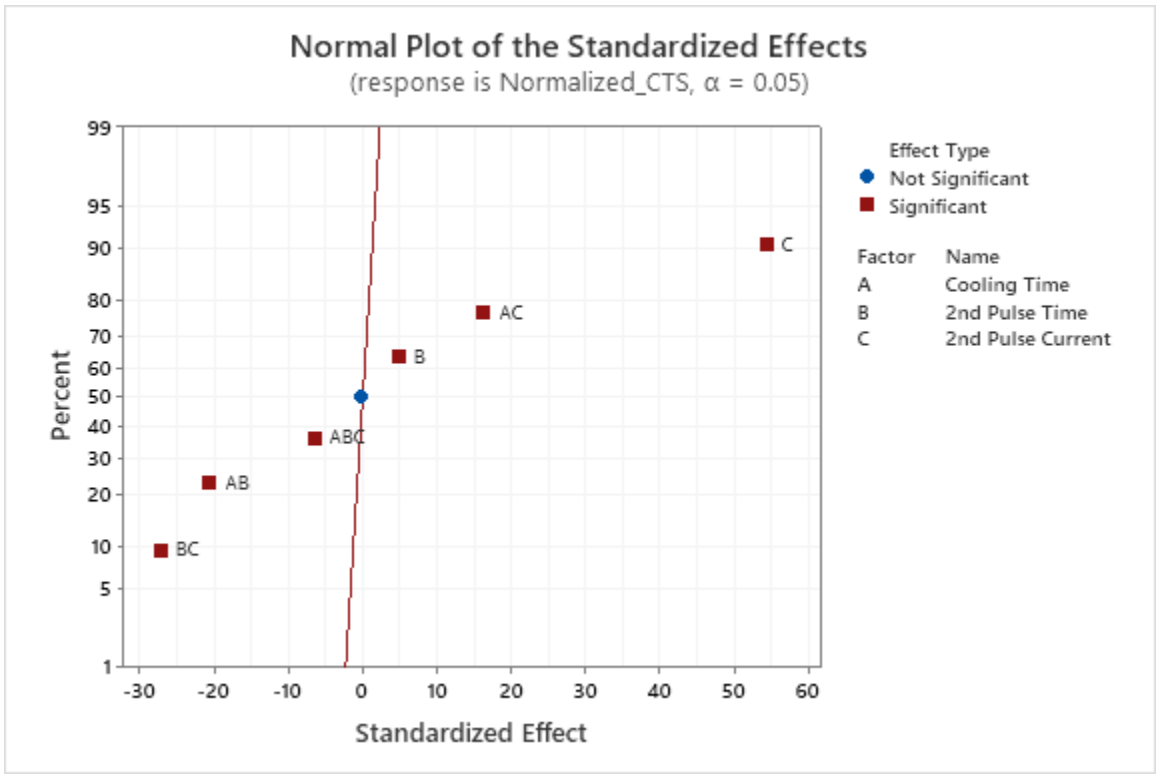
Normal Plot of the Standardized Effects
(response is Normalized_CTS, α = 0.05)
Percent
99
95
90
80
70
60
50
40
30
20
10
5
1
C
AC
B
ABC
AB
BC
-30
-20
-10
0
10
20
30
40
50
60
Standardized Effect
Effect Type
Not Significant
Significant
Factor Name
A Cooling Time
B 2nd Pulse Time
C 2nd Pulse Current

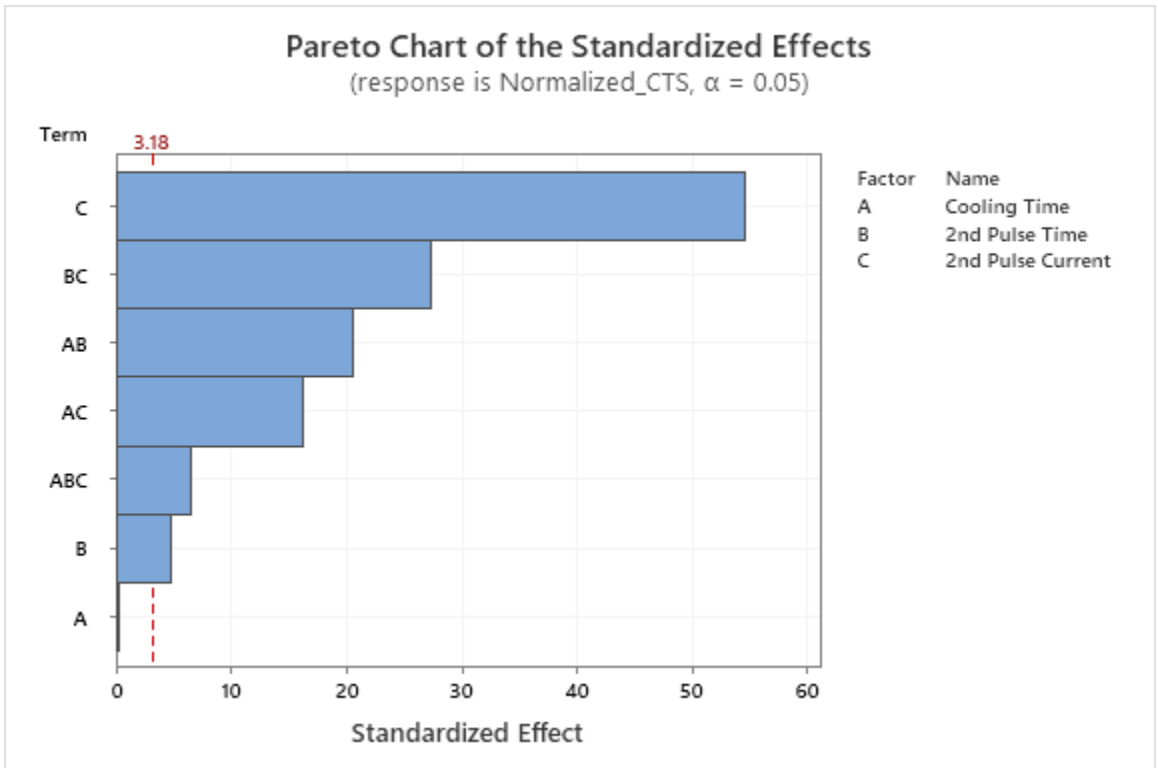
Pareto Chart of the Standardized Effects
(response is Normalized_CTS, α = 0.05)
Term
3.18
C
BC
AB
AC
ABC
B
A
0
10
20
30
40
50
60
Standardized Effect
Factor Name
A Cooling Time
B 2nd Pulse Time
C 2nd Pulse Current

# Two-Sample T-Test and CI: Halo TSS, No Halo TSS

## Method

$\mu_1$: population mean of Halo TSS
$\mu_2$: population mean of No Halo TSS
Difference: $\mu_1 - \mu_2$

*Equal variances are not assumed for this analysis.*

## Descriptive Statistics

| Sample | N | Mean | StDev | SE Mean |
|---|---|---|---|---|
| Halo TSS | 12 | 15.96 | 2.05 | 0.59 |
| No Halo TSS | 12 | 18.20 | 3.87 | 1.1 |

## Estimation for Difference

| Difference | 95% CI for Difference |
|---|---|
| -2.24 | (-4.92, 0.44) |

## Test

Null hypothesis $H_0: \mu_1 - \mu_2 = 0$
Alternative hypothesis $H_1: \mu_1 - \mu_2 \neq 0$

| T-Value | DF | P-Value |
|---|---|---|
| -1.77 | 16 | 0.095 |

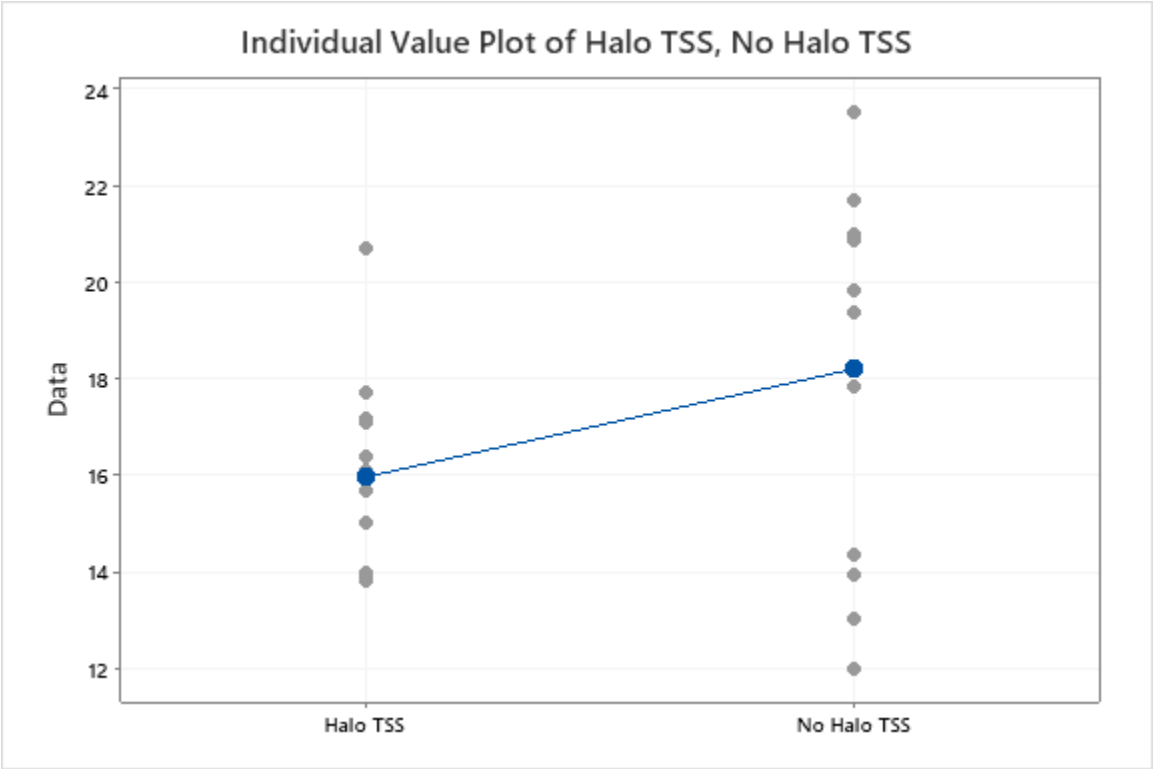
Individual Value Plot of Halo TSS, No Halo TSS
Data
24
22
20
18
16
14
12
Halo TSS
No Halo TSS

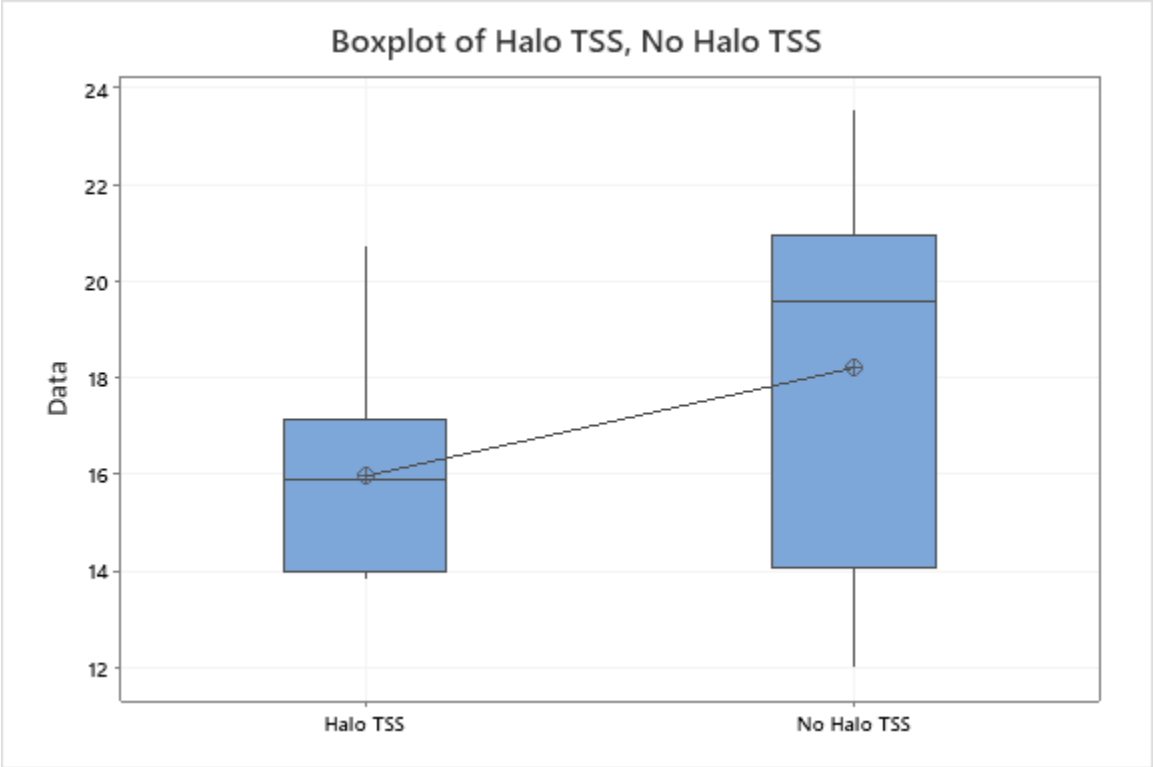
Boxplot of Halo TSS, No Halo TSS
Data
24
22
20
18
16
14
12
Halo TSS
No Halo TSS

# Two-Sample T-Test and CI: Halo CTS, No Halo CTS

## Method

$\mu_1$: population mean of Halo CTS
$\mu_2$: population mean of No Halo CTS
Difference: $\mu_1 - \mu_2$

*Equal variances are not assumed for this analysis.*

## Descriptive Statistics

| Sample | N | Mean | StDev | SE Mean |
|---|---|---|---|---|
| Halo CTS | 12 | 3.377 | 0.287 | 0.083 |
| No Halo CTS | 12 | 4.067 | 0.605 | 0.17 |

## Estimation for Difference

| Difference | 95% CI for Difference |
|---|---|
| -0.690 | (-1.102, -0.278) |

## Test

| | |
|---|---|
| Null hypothesis | $H_0: \mu_1 - \mu_2 = 0$ |
| Alternative hypothesis | $H_1: \mu_1 - \mu_2 \neq 0$ |

| T-Value | DF | P-Value |
|---|---|---|
| -3.57 | 15 | 0.003 |

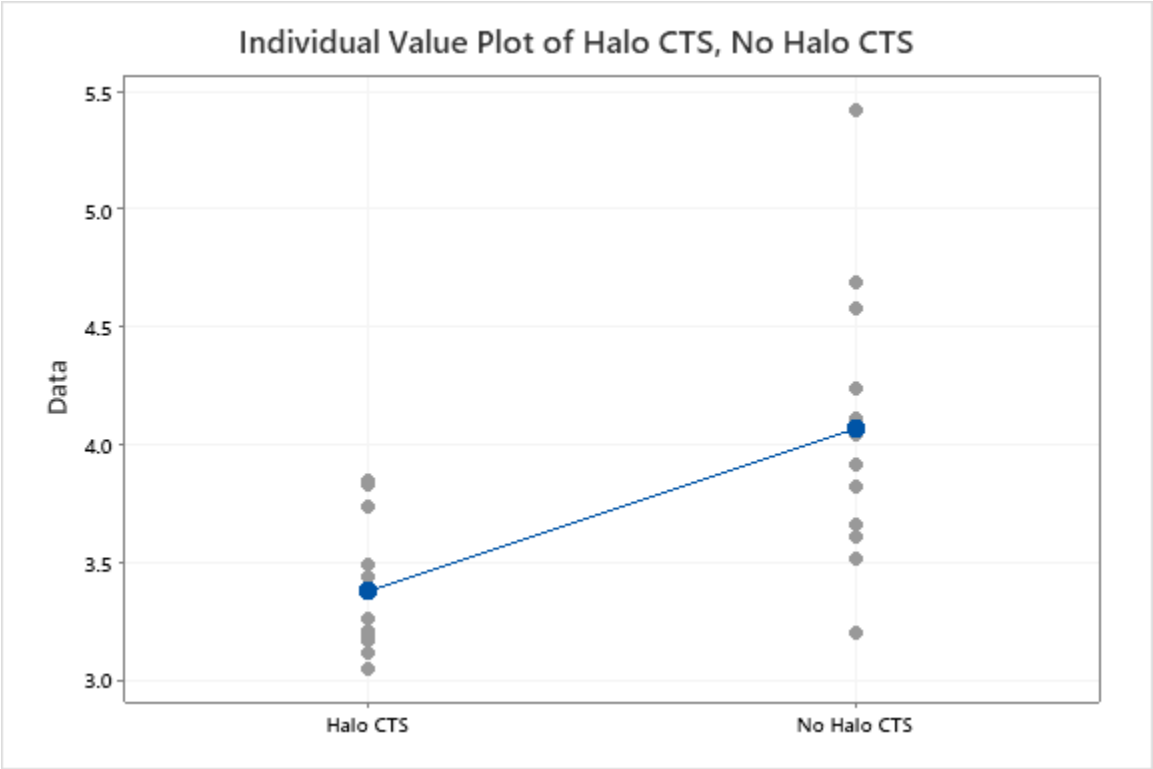
Individual Value Plot of Halo CTS, No Halo CTS
Data
5.5
5.0
4.5
4.0
3.5
3.0
Halo CTS
No Halo CTS

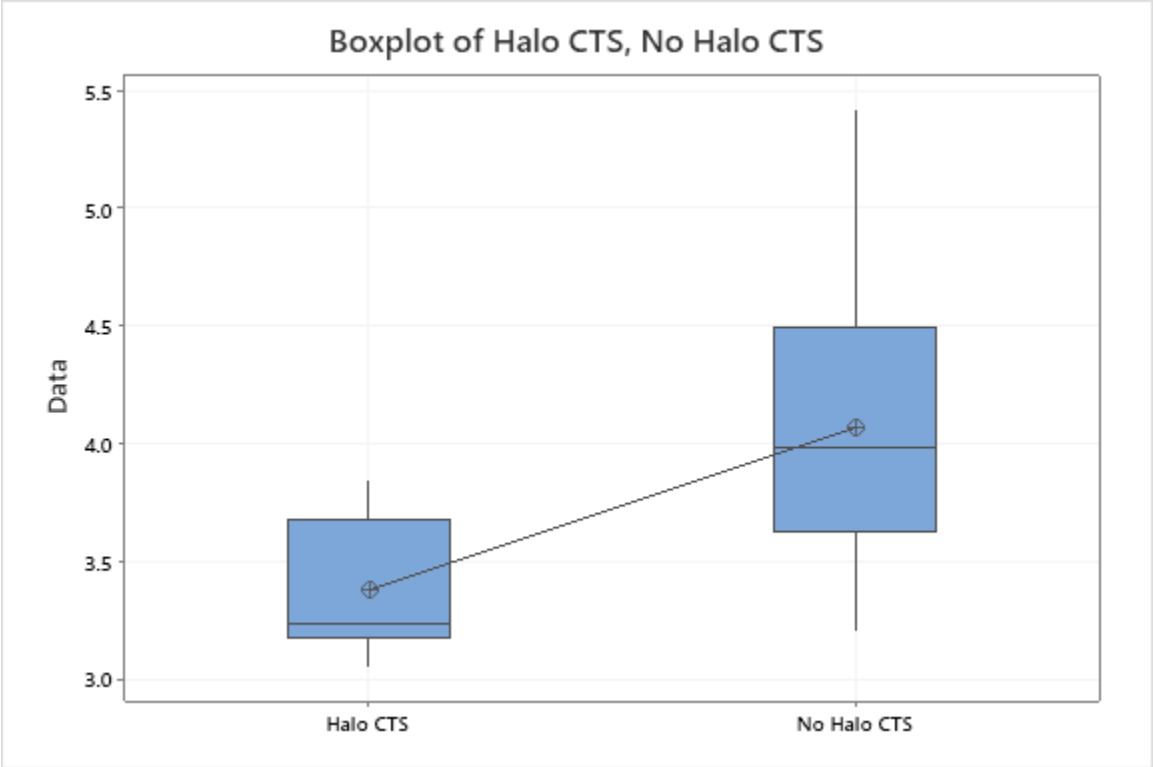
Boxplot of Halo CTS, No Halo CTS
Data
5.5
5.0
4.5
4.0
3.5
3.0
Halo CTS
No Halo CTS

# Response Optimization: Normalized_TSS, Normalized_CTS

## Parameters

| Response | Goal | Lower | Target | Upper | Weight | Importance |
|---|---|---|---|---|---|---|
| Normalized_TSS | Maximum | 1.89153 | 2.74359 | | 1 | 1 |
| Normalized_CTS | Maximum | 0.45198 | 0.63136 | | 1 | 1 |

## Solution

| Solution | Cooling Time | 2nd Pulse Time | 2nd Pulse Current | Normalized_TSS Fit | Normalized_CTS Fit | Composite Desirability |
|---|---|---|---|---|---|---|
| 1 | 2 | 8 | 9 | 2.77017 | 0.566160 | 0.797838 |

## Multiple Response Prediction

| Variable | Setting |
|---|---|
| Cooling Time | 2 |
| 2nd Pulse Time | 8 |
| 2nd Pulse Current | 9 |

| Response | Fit | SE Fit | 95% CI | 95% PI |
|---|---|---|---|---|
| Normalized_TSS | 2.7702 | 0.0817 | (2.5102, 3.0301) | (2.3993, 3.1410) |
| Normalized_CTS | 0.56616 | 0.00238 | (0.55858, 0.57374) | (0.55534, 0.57698) |

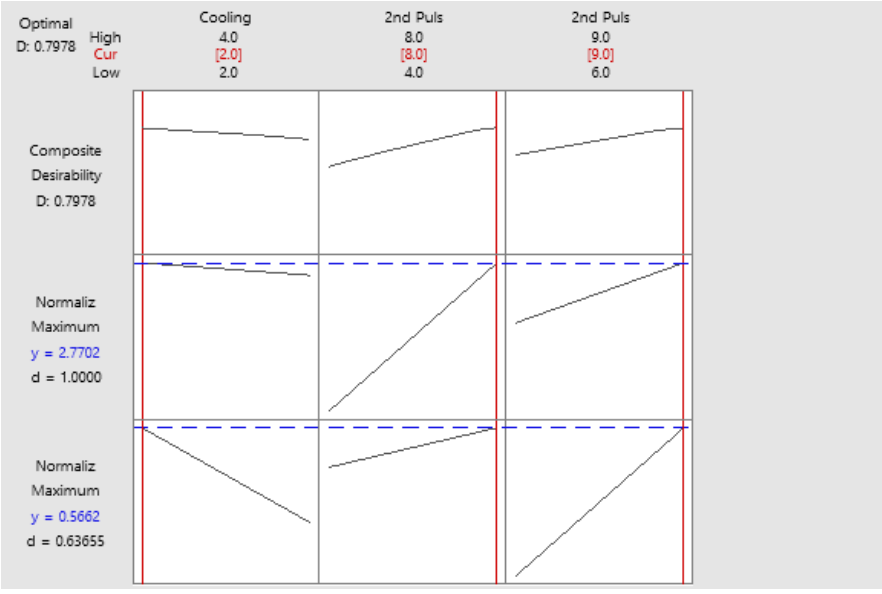

# Appendix B

## Supplementary Data for Chapter 6

### JMatPro® Results for Q&P980's Material Data

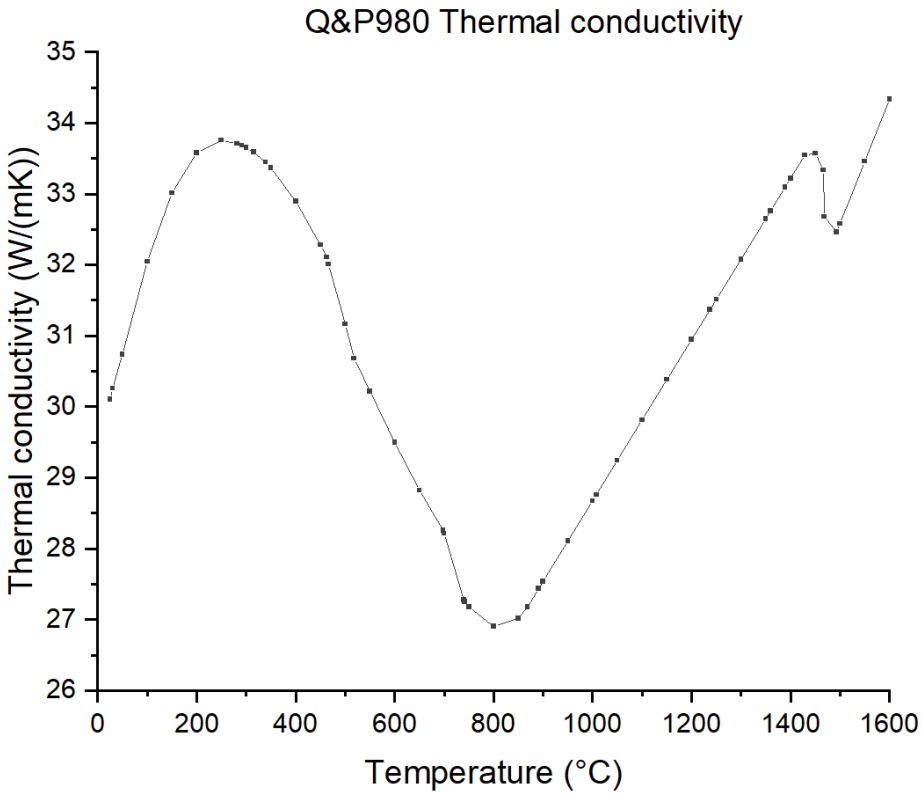

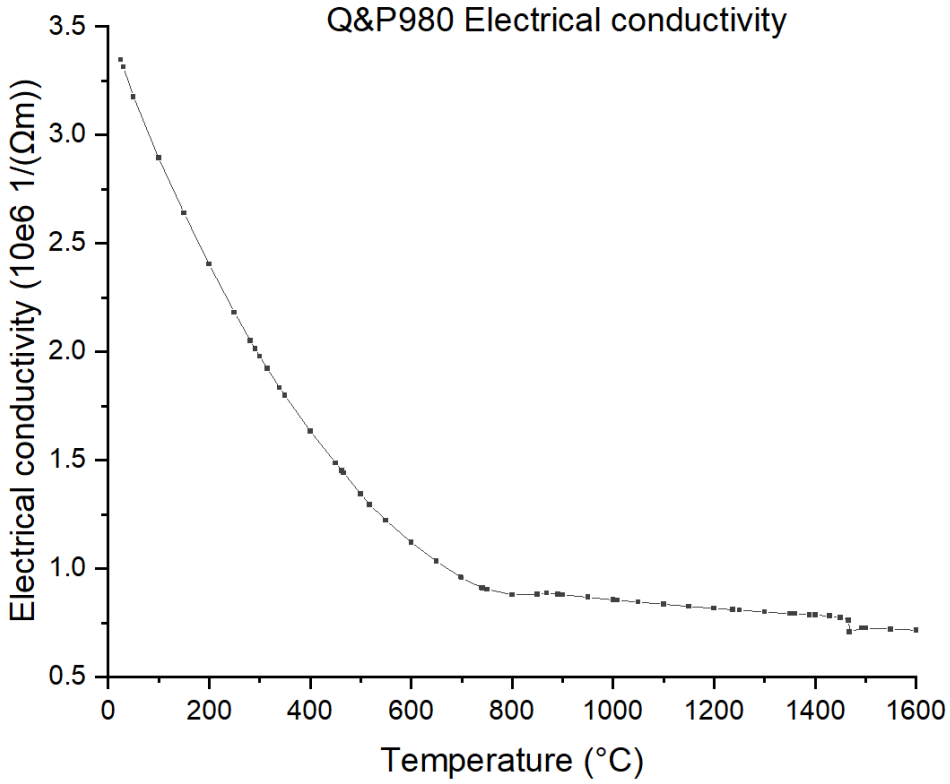
Q&P980 Electrical conductivity
Electrical conductivity (10e6 1/(Ωm))
3.5
3.0
2.5
2.0
1.5
1.0
0.5
0
200
400
600
800
1000
1200
1400
1600
Temperature (°C)

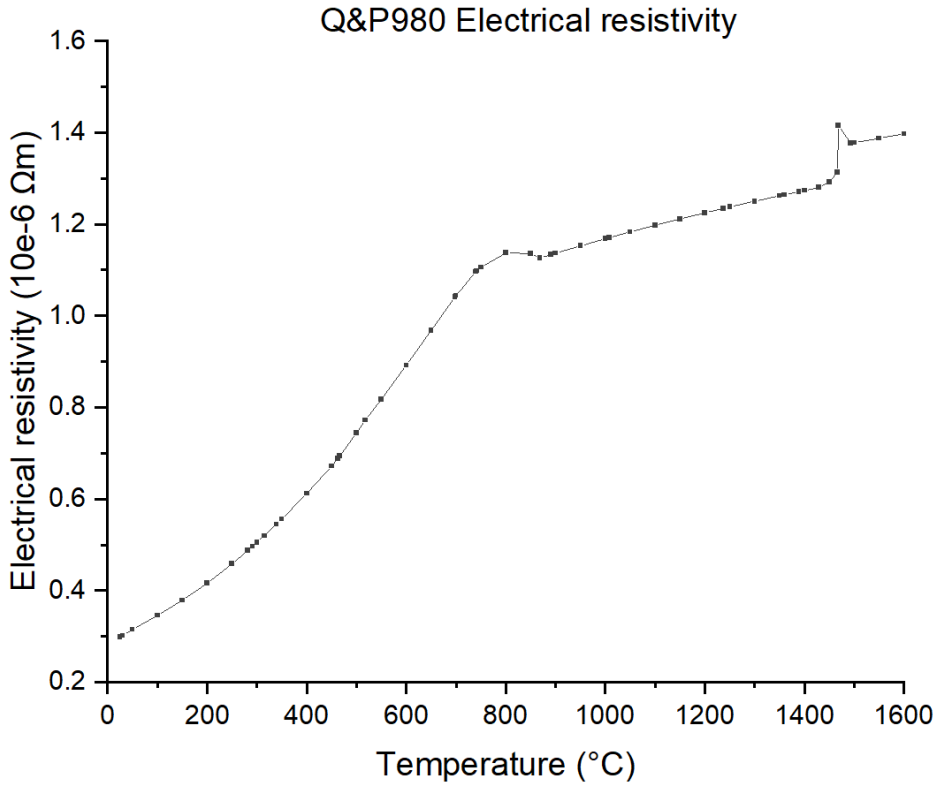
Q&P980 Electrical resistivity
Electrical resistivity (10e-6 Ωm)
1.6
1.4
1.2
1.0
0.8
0.6
0.4
0.2
0
200
400
600
800
1000
1200
1400
1600
Temperature (°C)

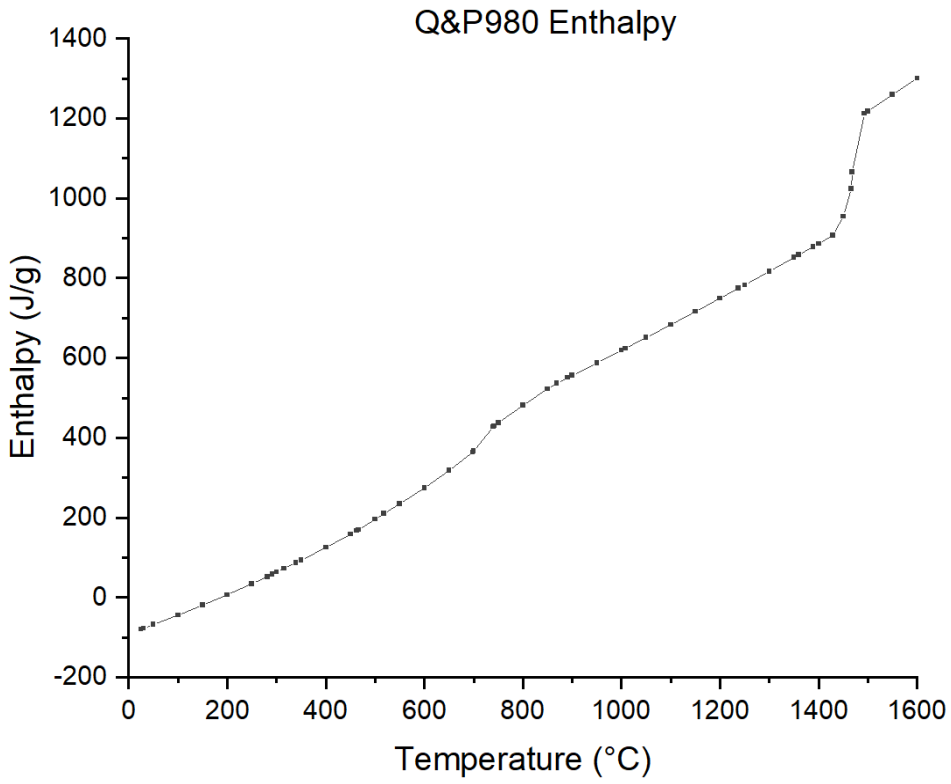
Q&P980 Enthalpy
Enthalpy (J/g)
Temperature (°C)
1400
1200
1000
800
600
400
200
0
-200
0
200
400
600
800
1000
1200
1400
1600

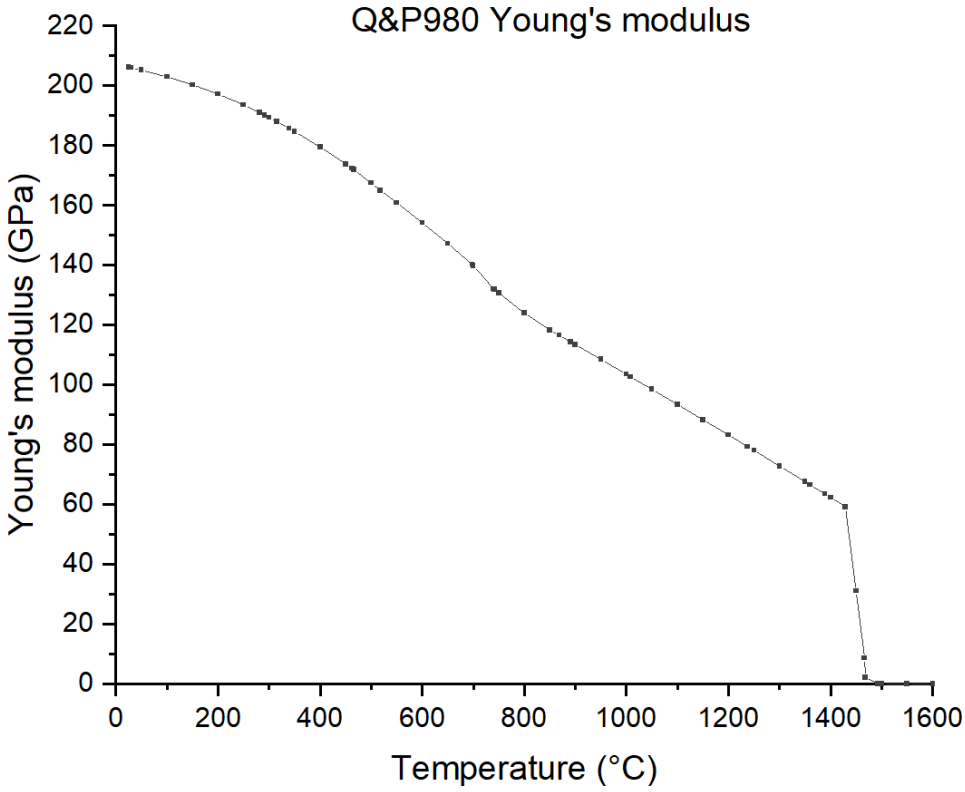
Q&P980 Young's modulus
Young's modulus (GPa)
Temperature (°C)
220
200
180
160
140
120
100
80
60
40
20
0
0
200
400
600
800
1000
1200
1400
1600

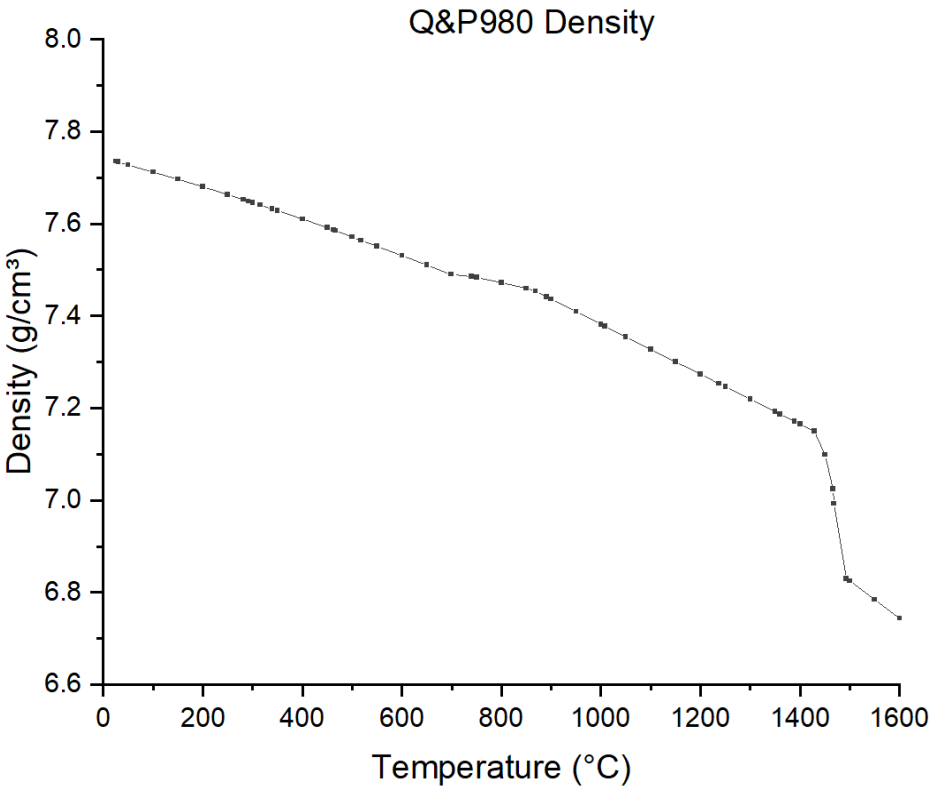
Q&P980 Density
Density (g/cm³)
8.0
7.8
7.6
7.4
7.2
7.0
6.8
6.6
0
200
400
600
800
1000
1200
1400
1600
Temperature (°C)

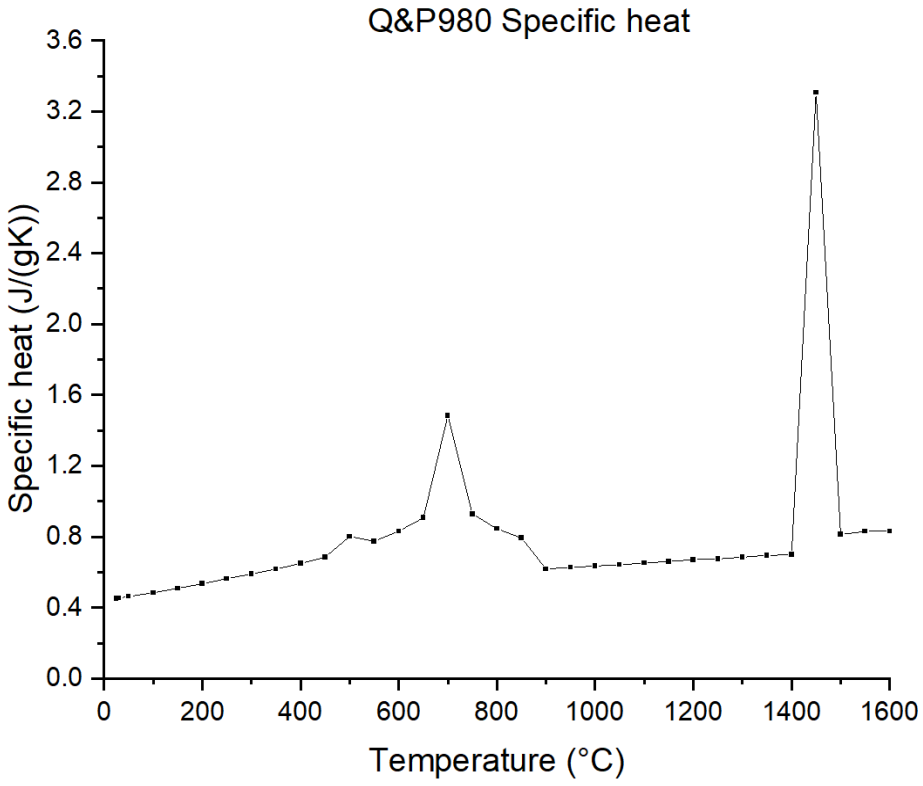
Q&P980 Specific heat
Specific heat (J/(gK))
3.6
3.2
2.8
2.4
2.0
1.6
1.2
0.8
0.4
0.0
0
200
400
600
800
1000
1200
1400
1600
Temperature (°C)